Spin correlations in frustrated magnets with orbital ordering

Thesis submitted in accordance with the requirements of
Royal Holloway, University of London for the degree of Doctor in Philosophy by

Andrea Joanne Magee

Department of Physics, Royal Holloway, University of London
Egham
Surrey
TW20 0EX

September 2010

Declaration of Authorship

I, Andrea Joanne Magee, hereby declare that this thesis and the work presented in it is entirely my own. Where I have consulted the work of others, this is always clearly stated.

Signed: ....

Date: ....

Abstract

The magnetism of two model systems that undergo orbital ordering transitions, MnV_2O_4 and $GdVO_3$, has been studied using neutron scattering and synchrotron x-rays.

MnV_2O_4 comprises a network of corner-sharing tetrahedra with the vanadium ions forming a pyrochlore lattice. This structure is typical of systems that are geometrically frustrated in three dimensions. In the case of MnV_2O_4, the V^{3+} 3d electrons occupy two out of three t_{2g} orbitals and, therefore, the orbital degrees of freedom come into play. The presence of the magnetic Mn^{2+} ions leads to ferrimagnetic structures, allowing the possibility to control the orbital ordering.

The low temperature MnV_2O_4 magnetic structure and phase diagram were determined using single-crystal neutron diffraction. The magnetic excitations in the low temperature phases were studied using inelastic neutron scattering. The rotation method was employed on MAPS to obtain four-dimensional volumes of reciprocal space. Unidirectional polarization analysis was employed on IN20 to focus on details of the magnetic dispersion with great sensitivity. The previously published magnetic exchange model was unable to account for our data and a new model is proposed. This magnetic exchange model distinguishes between the two candidate orbital ordering models.

The perovskite orthovanadates, RVO_3 (R = rare earth or Y), display a variety of *commensurate* magnetic structures. Until now the magnetic structure of $GdVO_3$ had not been determined by neutron diffraction due to strong absorption at thermal wavelengths. Magnetisation measurements for $GdVO_3$ reveal an unusual magnetic memory effect and a series of magnetic-field-induced phase transitions at low temperature.

We have studied the complex magnetic ordering in $GdVO_3$ using hot neutrons on D9 at ILL and resonant x-ray scattering on ID20 at ESRF. We have determined new magnetic structures in the rich magnetic phase diagram of $GdVO_3$ at low temperature, which we find to be comprised of *incommensurate* orderings of gadolinium moments.

Dedicated to Anna, Michael and Suzanna.

Acknowledgements

My greatest thanks go to Jon Goff for his wisdom, support and endless patience. You really were the best supervisor that I could have hoped for. Thank you!

Mrs Probert, my school physics teacher and sixth form tutor, deserves a thank you for her encouragement and help during my GCSEs and A-levels, without her I would never have embarked on a degree in Physics at all.

Thank you to Des McMorrow for setting up my stagiaire placement at the ESRF, the first step which put me on the road to a PhD. Many thanks to Pascale Deen for being my stagiaire supervisor. Your help with experiments, the pep-talks over coffee and of course all the sophisticated nights in Grenoble's classiest haunts were very much appreciated!

Many hours were spent on experiments and data analysis at ILL by Garry McIntyre, I am very grateful for your help! Thanks also to Mechthild Enderle for all her hard work on experiments and for her expertise on IN20 - I apologise for the 2am call outs! Thanks to Bachir Ouladdiaf for always being happy to help

with sample alignment. Thanks also to Paul Freeman and Ross Springell.

It was always a pleasure working at the ESRF and my thanks go to Luigi Paolasini, Laurence Bouchenoire and Claudio Mazzoli for their experimental expertise as well as welcome chats over coffee in the sun. Thanks also to Peter Normile, Paul Thomson and Simon Brown.

Many thanks to Chris Frost for all his help at ISIS and to Russell Ewings for helping me get to grips with the MAPS computer program, Horace.

Useful discussions were had with John Chalker and Peter Conlan whose efforts in producing a Matlab magnetic model calculation was instrumental in the analysis of the MnV_2O_4 data. An excellent continuation of the data modelling using McPhase was done by Duc Le from HZB with assistance from Martin Rotter. Thank you for all the time you spent on this Duc and for your patience in explaining the intricacies to me!

The work couldn't have been done without the samples so thanks to Tung for his crystals and for teaching me how he made them. Thank you to the boys in the Living Room for keeping me entertained and in trouble in year one! Special thanks to Simon Lee and Markos Skoulatos for their words of wisdom and help with experiments and analysis, your help was invaluable.

Thanks to Moreton Moore at RHUL for his assistance characterising samples on the x-ray set and to the RHUL crowd for keeping me company in the Cabin.

Lastly I would like to thank all my friends and family for checking on my

progress and being interested!

Most especially my heartfelt thanks to Mam, Dad and Suzy for always being there for me, supporting and encouraging me the whole way. I couldn't have done it without you, thank you so much!

Contents

List of Figures

List of Tables

1 Introduction

The Greeks were aware of magnetism in 800 B.C. when they discovered that the mineral magnetite Fe_3O_4, also known as lodestone, attracted iron. The property of magnetism is claimed to have been utilised in the form of the compass by the Chinese as far back as the 13^{th} century B.C., although the invention of the compass is generally considered to be of Arabic or Indian origin [1]. The magnetic ions in magnetite are arranged on a three-dimensional pyrochlore lattice made of corner sharing tetrahedra. The pyrochlore crystal structure is based upon the mineral Pyrochlore $(Na,Ca)_2Nb_2O_6(OH,F)$, which is named from the Greek words 'pyro' ($\pi\tilde{u}\rho$) meaning fire and 'chloros' ($\chi\lambda\omega\rho\acute{o}\varsigma$) meaning green, because the mineral turns green upon ignition [2]. The pyrochlore crystal structure describes materials of the type $A_2B_2O_7$ where A and B are generally rare-earth or transition metal species. These systems are particularly susceptible to geometrical frustration and novel magnetic effects [2]. The physical properties of materials with the pyrochlore structure are very varied and range from superconducting materials, electronic insulators, ionic conductors, metallic conductors, mixed ionic and electric conductors, spin ice systems and spin glass systems [3, 4].

Transition metal (TM) oxides in particular have been the topic of much research since the discovery of high temperature superconductors in 1986 [5]. The TM oxides often have a perovskite ($CaTiO_3$) structure where the TM ion is at the centre, surrounded by six oxygen ions. The high symmetry undistorted cubic structure is often lowered to orthorhombic, tetragonal or trigonal structures in many perovskites to minimise their energy. Perovskite materials also exhibit many interesting properties including colossal magnetoresistance, ferroelectricity, superconductivity, charge ordering, spin dependent transport, high thermopower and the interplay of structural, magnetic and transport properties. These properties enable them to be used in many practical applications such as catalyst electrodes and sensors in fuel cells and memory and spintronics devices [6]. The reason for such varied properties is that the charge, spin and orbitals of these materials have several degrees of freedom which interact.

1.1 Basic theory of magnetism

Magnetism is concerned with the formation and behaviour of magnetic moments in solids. It is a collective phenomenon; the magnetic properties of atoms and molecules individually are often very different to those of the macroscopic systems of which they are a part. A magnetic moment $\boldsymbol{\mu}$ and the current I around a loop of area $\mathbf{ds}$ can be related using classical electromagnetism [7,8]:

$$\mathbf{d}\boldsymbol{\mu} = I\mathbf{ds} \tag{1.1}$$

where the magnetic moment points perpendicular to the plane of the current loop. This magnetic moment is associated with orbital angular momentum $\mathbf{L}$ because the current loop is formed from the movement of particles with mass (electrons). γ is the gyromagnetic ratio:

$$\boldsymbol{\mu} \ = \gamma\mathbf{L} \tag{1.2}$$

In a magnetic solid, the vector sum of the magnetic moments per unit volume is known as the magnetisation $\mathbf{M}$. In free space, $\mathbf{M}$ is zero and the magnetic field can be described by the magnetic flux density $\mathbf{B}$ and magnetic field strength $\mathbf{H}$.

$$\mathbf{B} = \mu_0\mathbf{H} \tag{1.3}$$

where μ_0 is the permeability of free space. When a magnetised sample is introduced the relationship becomes:

$$\mathbf{B} = \mu_0(\mathbf{H} + \mathbf{M}) \tag{1.4}$$

In a linear material where **M** is linearly related to **H**, **M**= χ**H** where χ is the magnetic susceptibility. There is still a linear relationship between **B** and **H**:

$$\mathbf{B} = \mu_0(1 + \chi)\mathbf{H} = \mu_0\mu_r\mathbf{H} \tag{1.5}$$

μ_r is the relative permeability of the material and is equal to 1+χ [7,8] .

1.1.1 Hund's Rules

The resultant angular momentum of an atom is dependant only on electrons in unfilled shells (the net angular momentum of a filled shell is zero). There are two factors to consider when determining the appropriate way to add the momentum of the individual electrons to obtain the overall angular momentum of the atom:

- Electrostatic Coulomb interaction between the atomic electrons leads to an effective coupling between the spin angular momenta.
- Spin-orbit interaction, a relativistic effect which becomes more significant for heavier atoms [8].

L-S or Russell-Saunders coupling

For low to intermediate weight elements the electrons' static interactions dominate and the spin-orbit interaction can be treated as a perturbation. The combination of angular momentum quantum numbers which minimize the ground state energy is found by applying Hund's rules.

> "When an atom has orbitals of equal energy, the order in
> which they are filled by electrons is such that a maximum
> number of electrons have unpaired spins." [1]

1. Maximise the total spin angular momentum S.

   Keeping the spins parallel minimises the coulomb repulsion between electrons.

2. Maximise the total orbital angular momentum L.

   Electron orbits rotating in the same direction minimises the coulomb repulsion between electrons.

3. J = L - S if shell is less than half filled.

   J = L + S if shell is more than half filled.

The rules assume that the repulsion between the outer electrons is very much greater than the spin-orbit interaction which is in turn stronger than any other remaining interactions. The last rule arises from the spin-orbit interaction. It works well for rare earth ions but for some systems such as TM ions, the spin-orbit energies are not as significant as the crystal field for example and so Hund's third rule is disobeyed. [7,8]

1.1.2 Crystal fields

The electric field experienced by an ion in a solid due to the charge on neighbouring ions is known as the crystal field. Consider the d orbitals (Figure 1.1). They can be divided into two classes depending on whether the lobes of the wavefunctions (i.e. the charge distribution of the ion) points between the x, y and z axes (t_{2g}) or along them (e_g) [7,8].

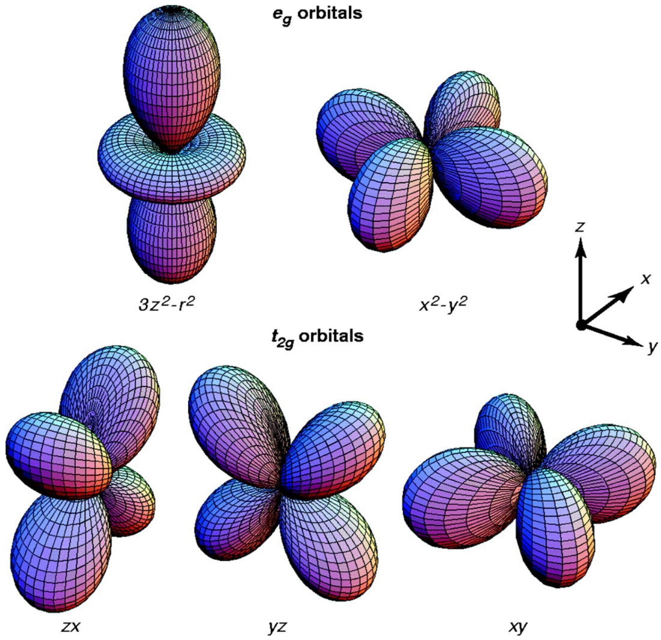

Figure 1.1: The angular distribution of d orbitals after Y. Tokura *et al.* [9]. The 5 fold degenerate d level is split into the 2 fold degenerate level (e_g), which contains $d_{3z^2-r^2}$ and $d_{x^2-y^2}$ levels, and the 3 fold degenerate level (t_{2g}) which contains d_{zx}, d_{yz} and d_{xy} levels.

Crystal field effects are stronger for d electrons than f electrons because the d electron wavefunctions extend a larger distance away from the nucleus whereas f electron wavefunctions are smaller. The f electrons are also partly shielded from Coulomb interactions with the surroundings by the s and p electrons in filled levels [10]. The ground state of the ion depends on the local environment and its symmetry. As an example see Figure 1.2. The d$_{xy}$ orbital (Figure 1.2(a)) has a lower overlap than the d$_{x^2-y^2}$ orbital (Figure 1.2(b)) and hence has a lower electrostatic energy. In an octahedral environment t$_{2g}$ states will have lower energy than the e$_g$ states [7].

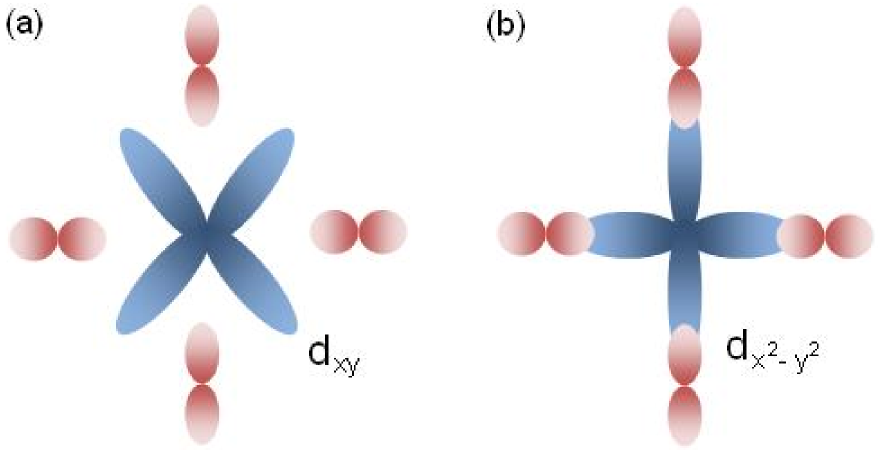

Figure 1.2: (a) The d$_{xy}$ orbital is lowered in energy compared to (b) the d$_{x^2-y^2}$ orbital in an octahedral environment. After Blundell [7].

Sometimes the magnetic properties can influence the symmetry of the local environment e.g. an octahedron can spontaneously distort because the cost in elastic energy is balanced by electronic energy saving due to change in crystal-field splitting. This is known as the Jahn-Teller effect [11] and is discussed in Section 6.1.2.

1.1.3 Exchange interactions

Exchange interactions arise as a result of the Exclusion Principle and the resulting change to the spatial distribution of the wavefunctions leads to strong electrostatic interactions. When the electrons on neighbouring magnetic atoms interact via an exchange interaction it is known as 'direct' exchange as there is no need to involve an intermediary ion in the process [7]. In 1934 Hendrik Kramers noted that Mn atoms in MnO could interact with one another despite having the non-magnetic oxygen atoms between them. To explain this he proposed the concept of 'superexchange', an indirect exchange interaction [12]. In superexchange, the coupling between two next-nearest neighbour cations through a non-magnetic anion is usually antiferromagnetic as this has a kinetic energy advantage [7, 8]. Figure 1.3 illustrates this.

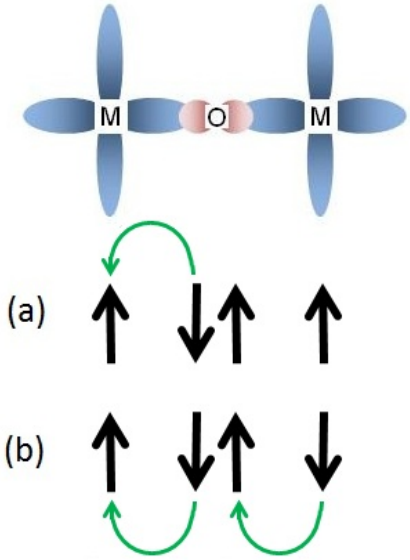

Figure 1.3: Superexchange in the magnetic oxide, MnO. Indirect exchange interaction occurs via the non-magnetic oxygen ion. The AF arrangement in (b) allows electrons to become delocalised over the MOM unit, whereas some of the excited configurations are prevented by the Exclusion Principle for the FM arrangement in (a). After [7].

An oxygen ion separates the 3d ions. Assume the chemistry is such that the oxygen has its electrons in the p shell and that there is one electron in each 3d shell. There are two distinct ways of putting the electrons in their orbits. Either with ferromagnetic (Figure 1.3(a)) or antiferromagnetic alignment (Figure 1.3(b)). To decide on which configuration has the lower energy, the kinetic energy needs to be considered. In the antiferromagnetic arrangement the total energy is lowered if an electron can hop between the ions. The interaction can be ferromagnetic if the two next-nearest neighbour positive ions are connected at 90 degrees to the bridging non-magnetic anion [7, 8].

1.1.4 Spin waves

Disturbances which propagate in magnetic materials and disrupt the order of the material are called spin waves. These excitations occur in lattices with continuous symmetry and are also known as ‘magnons’. Provided its wavelength is long enough, only a very small amount of energy is required to produce a spin wave [7]. In keeping with typical Curie points at room temperature and below, the energies of spin waves are typically only 10^{-3} - 10^{-2}eV and so can be effectively measured using inelastic neutron scattering [7]. Neutrons can gain energy by annihilating a spin wave excitation in the sample; the probability for this process to occur is directly proportional to the number of spin waves. The neutrons can also lose energy to create a spin wave in the system [13].

The excitation of spin waves as temperature is increased causes a ferromagnet’s magnetisation to be reduced. The spin waves are thermally excited and this gradually destroys the ordered state. The number of spin waves at each energy and temperature can be determined; this is directly related to the intensity of the spin waves [13]. Spin waves have been detected in ferromagnets, ferrimagnets, and antiferromagnets. See Figure 1.4 for the low energy excitations from a ferromagnetic spin chain.

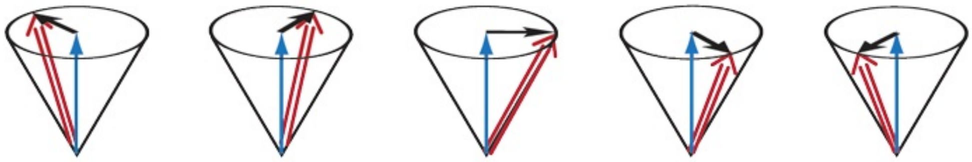

Figure 1.4: The classical picture of a spin wave in a ferromagnet: the spin (red arrow) precesses about a fixed axis (blue). The deviation is measured by the black arrows. Image by Alan Stonebraker [14]

In order to calculate a spin wave dispersion a model describing the magnetic energy of the system is needed. Generally it will include the following; crystallographic coordinates, spin orientations, exchange constants and anisotropy constants [13]. The simplest description of a spin Hamiltonian (the operator corresponding to the total energy of the system) is the isotropic Heisenberg model:

$$\hat{\mathcal{H}} = -\sum_{\langle ij \rangle} J_{ij} \hat{\boldsymbol{S}}_i . \hat{\boldsymbol{S}}_j \tag{1.6}$$

where $\hat{\boldsymbol{S}}_i$ is the spin operator on the ith site and J_{ij} is the Heisenberg exchange constant (representing the strength of magnetic exchange) between spins on the ith and jth site. If J_{ij} is positive, then a lower energy occurs when the moments are parallel and the ground state at zero temperature will be a ferromagnet, conversely if J_{ij} is negative, then the nearest-neighbour spins will align antiparallel to lower their energies, i.e. an antiferromagnet [13, 15].

The annihilation and creation operators $a_i^\dagger$ and a_i express the fluctuation of a spin away from its classical direction $\bar{z}$. The following expressions are derived from a linear approximation satisfying the spin commutation relation.

$$
\begin{aligned}
S_i^{\bar{x}} &= \sqrt{\frac{S}{2}}(a_i^\dagger + a_i) \\
S_i^{\bar{y}} &= i\sqrt{\frac{S}{2}}(a_i^\dagger - a_i) \\
S_i^{\bar{z}} &= S - a_i^\dagger a_i
\end{aligned}
\tag{1.7}
$$

Transforming the expressions 1.7 to a global coordinate gives:

$$
\begin{pmatrix} S_i^x \\ S_i^y \\ S_i^z \end{pmatrix} = \mathbf{R_i} \begin{pmatrix} S_i^{\bar{x}} \\ S_i^{\bar{y}} \\ S_i^{\bar{z}} \end{pmatrix}
\tag{1.8}
$$

where $\mathbf{R}_i$ is a rotational matrix corresponding to the relative rotation between the global z axis and the local $\bar{z}$ axis [13]. The spin operator of each sublattice is inserted into the Hamiltonian, a Fourier transformation is applied then the zeroth and quadratic operators are considered. The Hamiltonian is then diagonalised by Bogoliubov transformation to obtain the spin wave dispersion relations. When the magnetic lattice is an integer multiple of the crystallographic lattice, the number of modes is equal to the number of magnetic sublattices and the material is said to be commensurate [13].

1.1.5 Frustration

Geometrical Spin frustration

The geometrical properties of a crystal lattice can prevent simultaneous minimization of the interaction energies which can lead to highly degenerate ground states. For example, in 2D triangular and 3D pyrochlore lattices, it is not possible to satisfy all of the interactions in the system due to the symmetry of the magnetic ions in the crystal lattice. This can be seen in Figure 1.5 where the spin on the third site cannot be orientated in such a way as to satisfy the antiferromagnetic interactions with the other two spins. This means that several low energy states are possible and the system is said to be degenerate and frustrated [7, 16].

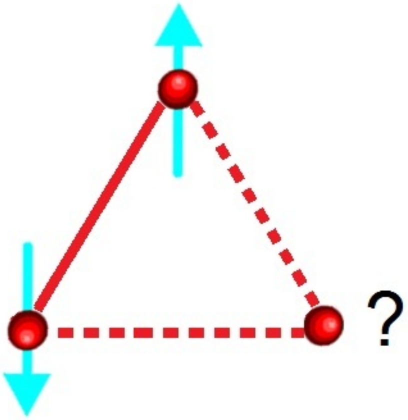

Figure 1.5: Geometrical spin frustration on a 2D triangular lattice. Not all exchange couplings can be simultaneously satisfied [7].

Geometrical frustration governs a range of phenomena in the collective behaviour of atoms. New properties develop when these frustrated materials are cooled well below the energy of moment-moment interactions [17]. Examples of these are spin ice, spin glasses and spin liquids [15, 18–26].

The most common example of geometric frustration is water ice. As predicted by Pauling in the 1930's [27], the hydrogen positions are disordered despite the well-ordered oxygen lattice. This prediction was based upon 'missing' entropy in specific heat measurements [17]. Spin ices are pyrochlore magnets with magnetic moments analogous to water ice. Like the hydrogen positions in water ice, there is disorder in the magnetic moment directions, despite the ordered lattice [17]. Spin ice can be studied over a range of energies as its lattice is formed at a higher temperature than that at which the moments interact [17].

The understanding of colossal magnetocapacitive coupling, multiferroic behaviour and mechanisms of high-transition-temperature superconductivity have required mechanisms related to geometric frustration [22, 24]. Geometrically frustrated systems have many potential uses. When the crystallisation energy of the material is significantly higher than the energy of the moment interactions, it is the structure which, through frustration, dictates the behaviour at low energies. However, unexpected patterns can emerge if the material itself can respond to the frustration. One such example is the blue phase of cholesteric liquid crystals [26] and self-assembled nanotubes (see Figure 1.6) [28] for drug delivery [29]. Nanotubes are lipid electrolyte bi-layers which curl up in the form of a tube when the polyelectrolytes and lipid membranes have different charge densities [17]. The properties of these nanotubes are such that they are useful in textile, cosmetics and drug industries. It is in principle possible to target specific sites in the body to deliver precise quantities of drugs. Understanding of the geometrical frustration of these compounds could allow the size and shape of the nanotubes to be altered for specific uses [17].

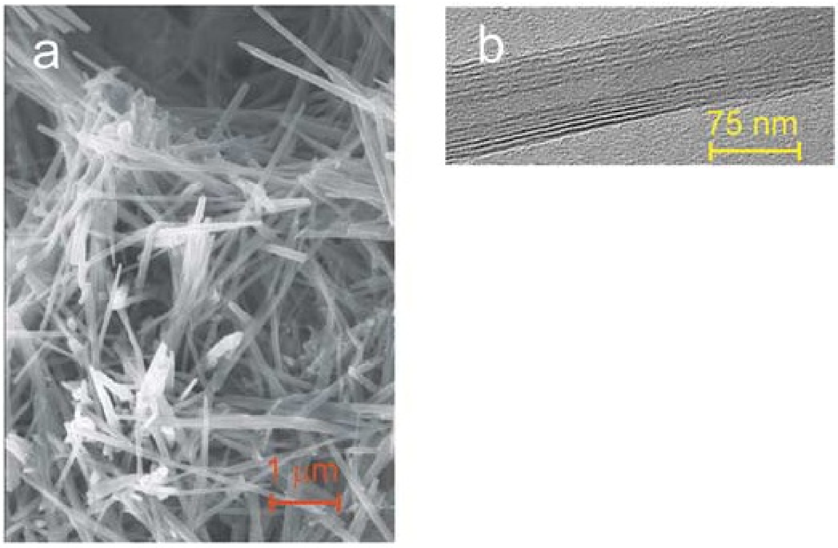

Figure 1.6: Self-assembled vanadium oxide nanotubes (a) Scanning electron microscopy (SEM) images show that the tubes can be several micrometres long, with diameters that vary from 60 to 100 nm. (b) A transmission electron microscopy (TEM) image shows the tubes to be multiwalled. Images taken from Nature paper by Krusin-Elbaum *et al.* [28]

There are several other examples of the uses of geometrically frustrated materials. The frustrated compound (Ba,Sr)TiO_3 (BST) could be used in dielectrics and storage capacitors for dynamic random access memories [16]. Geometric frustration has also led to the discovery of magnetic monopoles [21, 30, 31].

Orbital frustration

Orbital frustration does not require reduced dimensionality or a certain crystal geometry as the orbital interaction depends on the bond direction. The possible orbital states compete because each bond interaction requires the population of different orbital states. This dependence on the direction of the bonds leads to large degeneracy and quantum effects. The electrons in TM oxides which take part in superexchange are in the 3d state. For the vanadates, the t_{2g} orbitals are occupied but only two out of the three possible orbitals are relevant for superexchange in each direction and orbital fluctuations arise between them as shown in Figure 1.7.

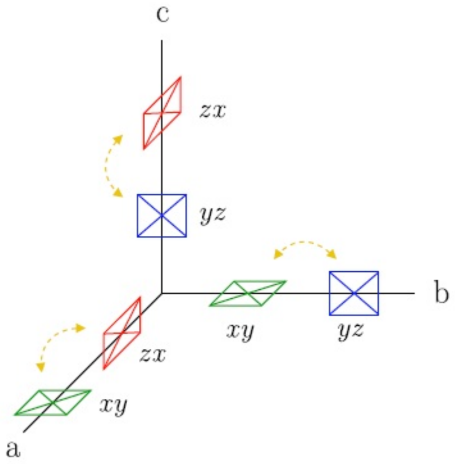

Figure 1.7: Two out of three t_{2g} orbitals are equally involved in the superexchange on every bond of a cubic crystal. A particular component of angular momentum is selected by these two orbitals. After Khaliullin *et al.* [32].

Tsunetsugu *et al.* [33] proposed the following orbital order in AV_2O_4 shown in Figure 1.8 (a) and (b). There are three orbitals; d_{xy} (blue), d_{yz} (red) and d_{zx} (yellow). The four different sizes of orbitals represent four different ab planes with different z coordinates. S. H. Lee *et al.* [34] showed how the occupation of orbitals could control the magnetic exchange interaction in this system, see Figure 1.8. At low temperatures in the orbitally ordered phase, spin chains are formed in [110] directions. At high temperature where the occupation of orbitals is random, three-dimensionally tangled chains are obtained.

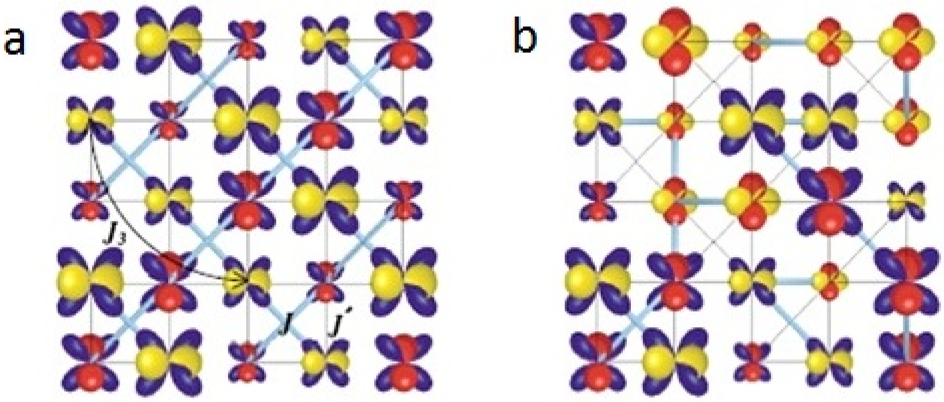

Figure 1.8: (a) and (b): After S.H. Lee *et al.* [34], viewed down the [001] direction. (a) At low T, antiferro-orbital ordering occurs, blue rods show significant intrachain J and J3, but negligible interchain J' as d_{yz} and d_{zx} orbitals do not overlap. (b) At high T the three orbitals, d_{xy}, d_{yz} and d_{zx}, are randomly occupied. The blue rods indicate possible dynamic magnetic interactions due to overlap of orbitals. Hence, there are fluctuating three-dimensionally tangled chains.

This thesis explores the interplay between magnetism and orbital order in the perovskite orthovanadate $GdVO_3$ and the pyrochlore MnV_2O_4.

1.2 Aims of the Project

The aims of the thesis were to characterize $GdVO_3$ and MnV_2O_4 single crystal samples fully using X-ray diffraction, SQUID magnetometry and heat capacity and to study their orbital and magnetic ordering and excitations at the ILL, ESRF and ISIS.

$GdVO_3$

Little neutron work had been carried out on $GdVO_3$ due to its strongly absorbing nature. Bulk thermodynamic measurements suggest a rich magnetic phase diagram at low temperatures [35]. We wanted to map the phase diagram at low temperatures and determine the orbital ordering and magnetic structure of $GdVO_3$ in zero field and in a field respectively.

MnV_2O_4

The studies already carried out on MnV_2O_4 had several inconsistencies which required clarification [33, 36–42]. Results from our initial data showed that the magnetic structure we had assumed for MnV_2O_4, in accordance with previous studies, was incorrect. We intended to confirm the crystal structure, magnetic structure and the orbital ordering of MnV_2O_4. There was also some disagreement as to whether the structural transition temperature was at $T_{\mathrm{M}} = 53$K or at $T_{\mathrm{N}} = 57$K [37, 38, 42–45] so we sought to resolve this issue. We wanted to understand the excitations in the ordered phase in a magnetic field and to map out the phase diagram using neutron diffraction. We aimed to investigate the frustrated magnetism of MnV_2O_4 and the role of the orbital degree of freedom in order to determine an entirely new way of thinking about charge transport in metals, and with it the first theoretical clues to the solution to a long standing theoretical problem: how to stabilise fractional spin or charge excitations in three dimensions.

2 Neutron and X-ray scattering

2.1 Scattering theory

X-rays and neutrons are useful in determining crystallographic and magnetic structures because their wavelengths are comparable to the distance between atoms and so they can be used to perform diffraction measurements [8]. In both the X-ray and neutron diffraction experiments carried out for this thesis, a beam was scattered from a single crystal sample. In a general diffraction experiment the X-rays or neutrons are incident on the sample with a wavevector of $\boldsymbol{k}_i$ and exit the sample with a scattering angle 2θ and a final wavevector $\boldsymbol{k}_f$ [46], see Figure 2.1.

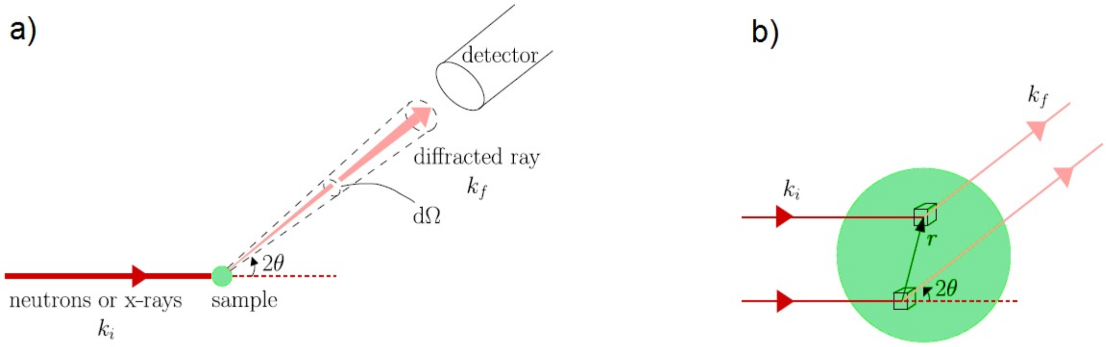

Figure 2.1: (a) A beam of neutrons or X-ray photons incident on a sample with incident wavevector $\boldsymbol{k}_i$. A diffracted ray $\boldsymbol{k}_f$ emerges within the solid angle dΩ, at the scattering angle 2θ. (b) A close up of the sample scattering volume showing two rays of the beam scattered by elemental volumes dV separated by a displacement vector **r**. After P. Normile [47]

For particle beams the energy is $Ei = \hbar^2|\mathbf{k}_i|^2/2m$ (particle mass = m). Constructive interference resulting in Bragg reflections is produced in elastic scattering when the scattering vector **Q** obeys the Laue condition and is equal to the reciprocal lattice vector **G**, see Equation 2.1.

$$\mathbf{Q} = \mathbf{k}_i - \mathbf{k}_f = \mathbf{G} \tag{2.1}$$

G can be described as follows with basis vectors $\mathbf{a}^*$, $\mathbf{b}^*$ and $\mathbf{c}^*$ and Miller indices h, k, and l:

$$\mathbf{G} = h\mathbf{a}^* + k\mathbf{b}^* + l\mathbf{c}^* \tag{2.2}$$

Elastic scattering occurs when there is zero energy transfer, $|\mathbf{k}_i| = |\mathbf{k}_f| = $ k.

The value of Q in this case is:

$$Q = 2ksin\theta = \frac{4\pi}{\lambda}sin\theta \tag{2.3}$$

In an elastic neutron or X-ray diffraction experiment the intensity of particles entering the detector per unit incident flux and solid angle dΩ is measured. This is called the differential cross-section and is defined as follows:

$$\frac{d\sigma}{d\Omega}(\mathbf{Q}) = N\frac{(2\pi)^2}{\upsilon}\sum_{\mathbf{G}}|F(\mathbf{Q})|^2\delta(\mathbf{Q}-\mathbf{G}) \tag{2.4}$$

N is the number of crystal unit cells in the sample scattering volume and υ is the volume of each cell. The δ function is associated with a summation over the lattice points of the whole crystal as opposed to the unit cell structure factor F($\mathbf{Q}$) which is only summed over the unit cell:

$$F(\mathbf{Q}) = \sum_{j} f_j(\mathbf{Q})e^{i\mathbf{Q}.r} \tag{2.5}$$

f$_j$($\mathbf{Q}$) is the scattering amplitude of the atom in the crystallographic unit cell at position vector $\mathbf{r}_j$.

2.2 Neutrons

Neutrons interact with matter in two different ways, either with short range strong nuclear forces or through the magnetic moment of the neutron. The neutron is a spin $\frac{1}{2}$ particle and as such has a non zero magnetic moment [8, 48, 49]. The neutron 'senses' the magnetic fields due to the unpaired electrons in the solid and, being uncharged, it can penetrate deep into the material and come close to the nuclei before being scattered by the nuclear forces [8, 48, 49]. Neutrons are created in large quantities by spallation or nuclear fission and the beam of neutrons produced has a spectrum of energies which are determined by the properties of the moderator; this therefore means that the neutrons also have a range of velocities. Thermal neutrons have a De Broglie wavelength which is similar to atomic spacings and so they are perfect for determining the structure of materials via diffraction experiments [8, 48, 49]. A thorough explanation of the theory of neutron scattering can be found in [48]. The most relevant aspects will briefly be covered here.

2.2.1 Coherent and incoherent nuclear scattering

A measure of the neutron-nucleus interaction or the ‘strength’ of scattering is b, the neutron scattering length. Each atom has a constant value which is independent of $\mathbf{Q}$ in thermal neutron scattering. The scattering cross section for a single nucleus is $4\pi\mathrm{b}^2$. The differential cross section is the fundamental quantity determined in a scattering experiment but it is the partial differential cross section, shown in Equation 2.6, which is used when the energy of the scattered beam is analysed:

$$\frac{d^2\sigma}{d\Omega dE_f} = \frac{\mathbf{k}_f}{\mathbf{k}_i}\frac{1}{2\pi\hbar}\int_{-\infty}^{\infty}\langle\sum_{j,j'} b_j b_{j'} e^{-i\mathbf{Q}.\mathbf{R}_{j'}(0)} e^{i\mathbf{Q}.\mathbf{R}_j(t)}\rangle e^{-i\omega t}dt \tag{2.6}$$

$\mathbf{R}_j(\mathrm{t})$ is the Heisenberg operator of the nuclear positions, $\langle ... \rangle$ is an ensemble average of the operator and the summation is over all pairs of nuclei. The nuclear spins and isotopes, in a single element at a temperature of a few mK, are randomly distributed and so the scattering length b varies between nuclei. In this case, the nuclear parameters can be decoupled:

$$\frac{d^2\sigma}{d\Omega dE_f} = \frac{\mathbf{k}_f}{\mathbf{k}_i}\frac{1}{2\pi\hbar}\sum_{j,j'}\langle b_j b_{j'}\rangle\int_{-\infty}^{\infty}\langle e^{-i\mathbf{Q}.\mathbf{R}_{j'}(0)} e^{-i\mathbf{Q}.\mathbf{R}_j(t)}\rangle e^{-i\omega t}dt \tag{2.7}$$

This cross section is averaged over all the nuclei with different scattering lengths

($\langle b_j, b_{j'} \rangle$ term). Assuming no correlation between the b values of the different nuclei gives the following relationships:

$$\begin{aligned} \langle b_j, b_{j'} \rangle &= \langle b \rangle^2, \qquad j^{'} \neq j \\ \langle b_j, b_{j'} \rangle &= \langle b^2 \rangle, \qquad j^{'} = j \end{aligned} \tag{2.8}$$

Equation 2.7 can now be written as:

$$\frac{d^2\sigma}{d\Omega dE_f} = \langle b \rangle^2 \sum_{j,j'} \langle j', j \rangle + (\langle b^2 \rangle - \langle b \rangle^2) \sum_{j} \langle j', j \rangle \tag{2.9}$$

The first term is the coherent scattering cross section $\sigma_{coh} = 4\pi\langle b \rangle^2$ and the second term is the incoherent scattering cross section $\sigma_{incoh} = 4\pi(\langle b^2 \rangle - \langle b \rangle^2)$. The coherent scattering term gives the intensity which would be produced if the scattering lengths of all the nuclei were equal to $\langle b \rangle$. The incoherent scattering term is the result of the random distribution of the deviations of the scattering lengths from their mean value and this must be used in order to obtain the intensity which is produced by the actual system [48].

2.2.2 Magnetic scattering

The neutron is an excellent probe to investigate the magnetic properties of materials as it has a magnetic dipole moment $\boldsymbol{\mu_n}$ and so can interact with any unpaired electrons in a magnetic atom. Elastic scattering of this kind allows the arrangement of the electron spins and their density distribution to be deduced. In addition, inelastic scattering gives information on the energies of the magnetic excitations [48]. Unlike X-rays, neutrons have equal sensitivity to nuclear and magnetic structures because the cross-sections for the two processes are roughly the same [8]. In a magnetic solid a magnetic field $\mathbf{B}$ arises due to the unpaired electrons. The neutron experiences this interaction potential $\boldsymbol{\mu_n}.\mathbf{B}$ when it enters the material and is therefore scattered. Only the magnetic moment component perpendicular to the scattering vector $\mathbf{Q}$ is able to scatter the neutrons and so contribute to the scattering amplitude. This means that neutrons are sensitive to the magnetisation direction as well as the spatial distribution [8, 48].

2.2.3 Inelastic scattering

Whereas elastic scattering gives information on the time-averaged structure, inelastic scattering gives information on the dynamical behaviour of a sample. Many excitations in condensed matter have energies similar to the energy of thermal neutrons and hence inelastic scattering of neutrons allows the energy of the excitations inside the sample to be deduced and this in turn gives information on the interatomic forces [48]. Inelastic scattering occurs when the neutrons impart or take energy to/from the sample on passing through it:

$$\hbar\omega = E_i - E_f \tag{2.10}$$

E_i and E_f are the incident and final energies respectively. If $\hbar\omega$ is greater than zero, energy is transferred from neutron to sample and an excitation of $\hbar\omega$ is created. If, on the other hand, $\hbar\omega$ is less than zero, the neutron gains energy from the sample and an excitation is annihilated [48].

Inelastic scattering from magnetic materials has two components. One is magneto-vibrational scattering due to the thermal displacement of the magnetic atoms from their equilibrium positions (resulting in the Debye-Waller factor and a reduction in the magnetic reflection intensity). The second is spin waves which, as discussed in Chapter 1 Section 1.1.4, are produced by fluctuations of the orientation of individual magnetic moments due to thermal energy and quantum zero-point fluctuations. The spins are coupled together via exchange interactions and so these fluctuations are collective excitations. Neutrons interacting in a magnetic crystal undergo inelastic scattering and either produce or annihilate excitations [7].

The cross section for inelastic scattering is:

$$
\begin{aligned}
\frac{d^2\sigma}{d\Omega dE_f} \propto \sum_{\mathbf{G}} \{ & S^2 \delta(\mathbf{Q}_z - \mathbf{G})\delta(\hbar\omega) + (\delta S)^2 (1 + \hat{\mathbf{Q}}_z^2) \times \\
& [\delta(\mathbf{Q}_z - \mathbf{k} - \mathbf{G})\delta(\omega - \Omega) + \delta(\mathbf{Q}_z + \mathbf{k} - \mathbf{G})\delta(\omega + \Omega)]\}
\end{aligned}
\tag{2.11}
$$

2.2.4 Diffuse scattering

A diffraction pattern for a completely ordered crystal would consist only of a discrete set of Bragg reflections. However deviations, such as thermal fluctuations and atomic defects, create disorder in a crystal which reduces the intensity of the Bragg reflections and produces diffuse scattering outside of these positions. The features of diffuse scattering depend upon the correlation functions of the deviations from a perfectly ordered crystal [50]. The static structure factor $S(\mathbf{Q})$ can be obtained by integrating over energy transfer. This is often useful as it is related to the static susceptibility $\chi(\mathbf{Q})$ which can be calculated if the Hamiltonian is known [51].

2.2.5 Polarised neutrons

Polarised neutrons are used to separate the magnetic and non-magnetic scattering. Polarisation of the incident beam may be used to see whether scattering is magnetic but complex magnetic structures may require full polarisation analysis of both the incident and scattered beam. One disadvantage in using polarised neutrons is that there is a considerable reduction in intensity [50].

A neutron has an angular momentum of $\pm \frac{1}{2}\hbar$ and spin $\mathbf{S} = \frac{1}{2}$. The spin vector $\boldsymbol{S_n}$ of a neutron defines the polarisation $\mathbf{P}$ of a neutron beam as the average over all neutron spin vectors normalised to their modulus:

$$\mathbf{P} = \langle \boldsymbol{S_n} \rangle / \frac{1}{2} = 2\langle \boldsymbol{S_n} \rangle \tag{2.12}$$

A neutron can be considered as being spin up ↑ or spin down ↓ relative to an applied magnetic field. The polarisation can then be expressed as a scalar as follows:

$$P = \frac{N_+ - N_-}{N_+ + N_-} = \frac{F-1}{F+1} \tag{2.13}$$

where N_+ and N_- is the number of neutrons with spin up and spin down and $F = \frac{N_+}{N_-}$ is the flipping ratio. A completely polarised beam has P = 1 (all ↑) or P = -1 (all ↓) and an unpolarised beam has P = 0.

In order to produce a polarised beam, polarised filters, mirrors (and supermirrors) or crystals can be used. This equipment causes polarisation by preferential absorption, reflection or Bragg reflection respectively. Once the polarised beam has been produced, an external magnetic field is required to prevent depolarisation. Varying the magnetic field or using spin flippers can be used to rotate or flip the polarisation. When using polarised neutrons the magnetic cross sections generally have spin-flip (SF) and non-spin-flip (NSF) components in all the x, y and z axes.

Unidirectional polarisation analysis

The method used in our experiments was unidirectional polarisation analysis, the experimental set up of which is shown in Figure 2.2. The flipper positions required to produce spin-flip (SF) and non-spin-flip (NSF) channels are shown in Table 2.1.

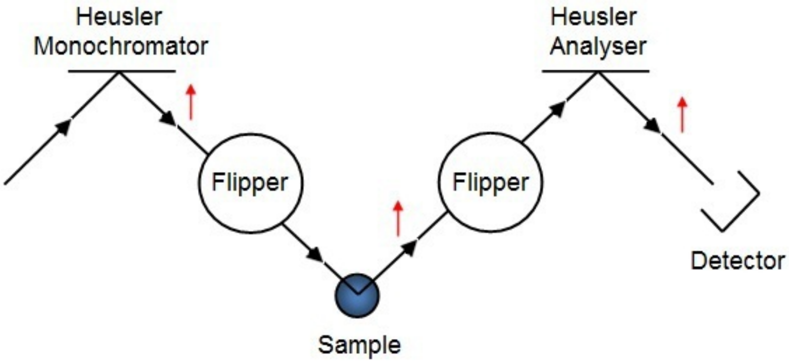

Figure 2.2: Experimental setup for unidirectional polarisation analysis.

$\sigma^{\uparrow\uparrow}$ $\sigma^{\downarrow\downarrow}$	Both flippers off Both flippers on	Non spin flip
$\sigma^{\downarrow\uparrow}$ $\sigma^{\uparrow\downarrow}$	1st flipper on, 2nd off 1st flipper off, 2nd on	Spin flip

Table 2.1: Unidirectional polarisation analysis: experimental set up to produce SF and NSF channels

Structural (nuclear) scattering is seen only in the non-spin-flip (NSF) channels. Magnetic scattering is seen in both the NSF and the spin-flip (SF) channels. The component of the magnetic moment parallel to z is observed in NSF and the component of the magnetic moment perpendicular to z is observed in SF. Spin incoherent signal is present in both channels. The SF channel contains only magnetic scattering and spin incoherent signal. The spin incoherent scattering is uniform in **Q** and centered on zero energy transfer. Therefore if a peak is seen in the SF channel which is peaked in **Q** and not at zero energy transfer it is magnetic.

2.2.6 Laue diffraction

Laue diffraction uses a white incident beam, fixed crystal geometry and an area detector which records the diffraction pattern over a large solid angle. The white beam ensures that Bragg condition is satisfied for many reciprocal lattice points [8]. The Laue diffraction instrument, Orient Express at the ILL, was used with the assistance of Bachir Ouladdiaf, to align our MnV_2O_4 single crystal samples. The Laue pattern is symmetrical when the incoming beam is parallel to a high-symmetry direction of the crystal. In cubic crystals, such as our MnV_2O_4 crystal, an incoming beam parallel to one of the unit cell edges produces Laue patterns with 4-fold symmetry (See Figure 2.3).

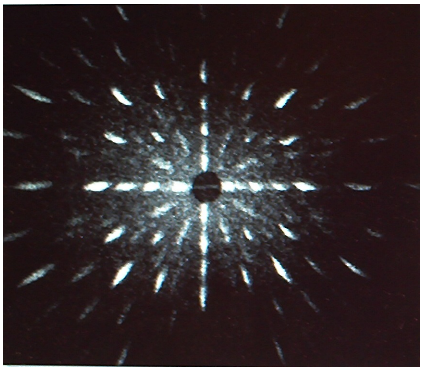

Figure 2.3: Laue diffraction pattern measured on Orient Express (ILL) with the incident beam parallel to a four fold axis of MnV_2O_4.

2.3 Synchrotron X-rays

In the 1930s the first particle accelerators called cyclotrons were built. They used the collision of high energy particles to split the nucleus of an atom, the results of these experiments helped physicists to understand the fundamental physics of the universe. Synchrotron radiation was seen for the first time in 1947. The electrons moved so fast that they produced electromagnetic radiation [46]. This was at first considered undesirable because it meant that the particles lost energy but later on in the 1960s it was found to be electromagnetic radiation with exceptional and useful properties. X-rays have both electric and magnetic components which are normal to each other and oscillate perpendicular to the direction of propagation. Interaction between the electric charge densities and the electric field of the X-ray gives information on the structural properties of the material. Interaction of the material spins and orbital densities with the magnetic field of the X-ray gives information on the magnetism of the material. The interactions are described by amplitudes or 'form factors'. X-rays can be considered quantum mechanically as photons carrying a quantum, $\hbar\omega$, of energy or $\hbar\mathbf{k}$ of momentum [46].

2.3.1 Thomson scattering

This type of elastic scattering occurs far from any absorption edge. When the electric field E of the incident X-ray exerts a force on the charge it causes a new wave with the same wavelength to be radiated. This is a first order interaction since no excitations occur [8,46]. The intensity I of both the incident and scattered beams is as follows:

$$I \propto |E|^2 \times Area\ of\ beam \tag{2.14}$$

$|E|^2$ is proportional to the energy of the beam per unit area which in turn is proportional to the number of photons. Therefore:

$$\frac{I_f}{I_i} = \frac{|E_f|^2}{|E_i|^2} \times \frac{A_D}{A_i} \tag{2.15}$$

A$_D$ is the area of the detector and A$_i$ is the incident beam area. E_f is the final radiated energy and E_i is the incident beam energy. If $\frac{I_i}{A_i} = \Phi_i$, the incident flux, and $A_D = d\Omega R^2$ where R is the target-detector distance then:

$$I_f = \Phi_i \frac{|E_f|^2}{|E_i|^2} \times d\Omega R^2 \tag{2.16}$$

So, the Thomson differential cross section is:

$$\left(\frac{d\sigma}{d\Omega}\right)_{Thomson} = \frac{I_f}{I_i \times d\Omega} \tag{2.17}$$

$$\left(\frac{d\sigma}{d\Omega}\right)_{Thomson} = \frac{|E_f|^2}{|E_i|^2} \times R^2 \tag{2.18}$$

The Thomson scattering length (i.e. the classical electron radius) is r_0, the scattering angle is Ψ and ε_0 is the permittivity of free space:

$$r_0 = \left(\frac{e^2}{4\pi\varepsilon_0 mc^2}\right) = 2.82 \times 10^{-5} \mathring{A} \tag{2.19}$$

$$\left(\frac{d\sigma}{d\Omega}\right)_{Thomson} = {r_0}^2 cos^2\Psi \tag{2.20}$$

In general this can be written as:

$$\left(\frac{d\sigma}{d\Omega}\right)_{Thomson} = {r_0}^2 P \tag{2.21}$$

where P is equal to 1 when the synchrotron radiation is scattered vertically, $P = cos^2\Psi$ when the synchrotron radiation is scattered horizontally and $P = \frac{1}{2}(1 + cos^2\Psi)$ when the source is unpolarised [8].

For Thomson scattering the atomic form factor as described above is defined by:

$$f^o(\mathbf{Q}) = \int \rho(\mathbf{r}) e^{i\mathbf{Q}.\mathbf{r}} d\mathbf{r} \tag{2.22}$$

r is the vector between two volume elements.

The Thomson scattering cross section is calculated by assuming that the electrons are ‘free’ which, for electrons bound in atoms, is obviously not the case. The atomic form factor describes the scattering amplitude associated with a single atom (it is the Fourier transform of the electron density in an atom) [8,46]. When there is no phase difference, $\mathbf{Q} = 0$, the form factor equals Z, the number of electrons in the atom. As $\mathbf{Q}$ increases, the wavelength of the radiation decreases and destructive interference occurs, damping the diffraction pattern [8,46].

2.3.2 Resonant X-ray scattering (RXS)

The RXS method was devised by Templeton and Templeton in the 1970's [52]. RXS can be used to investigate charge and orbital order parameters as well as magnetic properties. An X-ray photon can be absorbed by an electron only if its energy is above the binding energy of the electron. This binding energy is element and shell specific and is known as an absorption edge. When an atom absorbs an X-ray, a core electron is given enough energy to escape the atom and is known as a photoelectron (see Figure 2.4). It is then energetically favourable for an outer shell electron to move down and fill the hole in the core. This causes a fluorescent X-ray to be emitted [8,46].

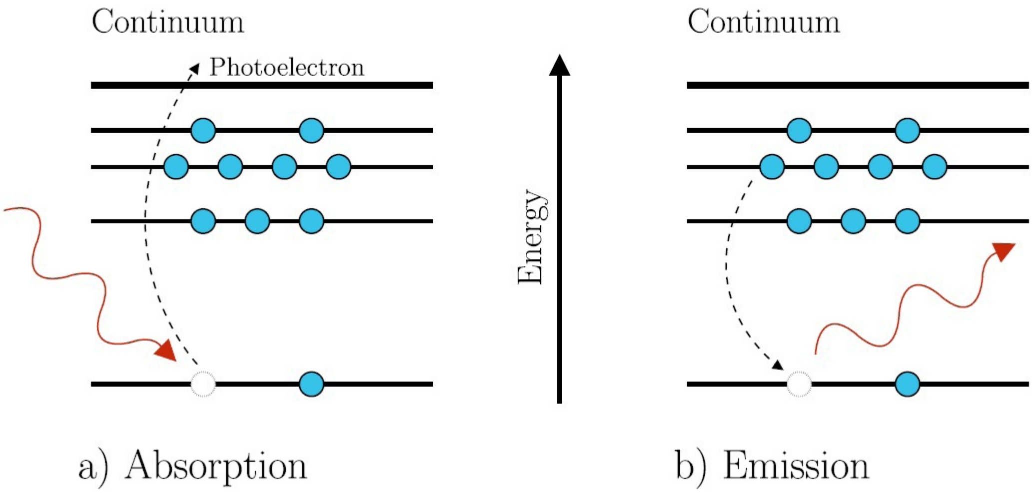

Figure 2.4: (a) An atom absorbs an X-ray with an energy large enough to promote a core electron to the continuum. (b) The vacancy can then be filled by an outer shell electron which results in the emission of a fluorescent X-ray. A large increase is observed in the fluorescence absorption spectrum. Electrons are shown as blue circles. After Skoulatos [53]

When the incident photon energy is close to the atomic absorption edge large resonant enhancements of the scattering cross section are observed [54]. For the rare earths it is the L_{II} and L_{III} edges and in transition metals it is the K edges. The polarisation dependence of the resonant cross section can be used to deduce information on the magnetic moment direction and the symmetry of the ordered state. Resonances sensitive to magnetic and quadrupolar order have been observed [54]. Resonant magnetic X-ray scattering (RMXS) was first seen by Namikawa *et al.* [55] in 1985 when they were studying Nickel. In 1988 Gibbs *et al.* was investigating the magnetic structure of Holmium and observed RMXS when a large resonant enhancement was seen when the X-ray energy was tuned to the L_{II} and L_{III} edges [56].

Because electrons in solids cannot be considered as 'free', the scattering theory given by Thomson scattering must be extended. The scattering length of the atom becomes more complicated and includes both real and imaginary parts:

$$f(\mathbf{Q},\omega) = f^{o}(\mathbf{Q}) + f'(\omega) + if''(\omega) \tag{2.23}$$

f' and *f"* are energy dependent and are known as the dispersion corrections to f^{o}. Classically describing RXS involves thinking of an atom as an assembly of damped forced charge oscillators. To describe RXS in quantum mechanical terms requires time-dependent perturbation theory [46]. The transition rate probability W between initial $|i\rangle$ and final $|f\rangle$ states of the combined system of target electron and X-ray photon is given by:

$$W = \frac{2\pi}{\hbar}\langle f|\mathcal{H}_I|i\rangle + \sum_{n=1}^{\infty}\frac{\langle f|\mathcal{H}_I|n\rangle\langle n|\mathcal{H}_I|i\rangle}{E_i - E_n}^{2}\rho(\varepsilon_f) \tag{2.24}$$

where $\rho(\varepsilon_f)$ is the density of states and the interaction between the photon and the electron is described by the Hamiltonian $\mathcal{H}_I$. Although RXS is a quantum mechanical process, this equation can be used to describe RXS semi-classically; a core electron at an initial state is given energy by the incident photon and makes a virtual transition to an intermediate state $|n\rangle$ before relaxing back to the initial state with the creation of a scattered photon which is experimentally detected. Resonant behaviour arises when the denominator tends to zero which occurs when the incident energy E_i, is equal to the energy of the intermediate state E_n or when it corresponds to an absorption edge [46].

The term $\langle f|\mathcal{H}_I|i\rangle$ from Equation 2.24 is the matrix element M_{if} and is the first-order perturbation term. This gives an interaction Hamiltonian (Equation 2.25) which is responsible for photoelectric absorption (first term) and Thompson scattering (second term):

$$\mathcal{H}_I = \frac{e\mathbf{A}.\mathbf{p}}{m} + \frac{e^2\mathbf{A^2}}{2m} \tag{2.25}$$

A is the vector potential describing electromagnetic fields, e and m are the electron's charge and mass respectively and **p** is the momentum operator of the electron. In summary, RXS is used to investigate intermediate unoccupied atomic states. If the degeneracy of the intermediate state is lifted by magnetic or Jahn-Teller interactions it becomes sensitive to magnetic or orbital ordering.

3 Experimental Techniques

3.1 Neutron instruments

3.1.1 Operating principles of two-axis diffractometers

As discussed in Section 2.1, Bragg reflections are produced by elastically scattered neutrons when the scattering vector is equal to a reciprocal lattice vector. This type of reflection can be studied using two-axis diffractometers [7]. Examples of two-axis diffractometers include powder and single crystal diffractometers, small angle instruments and reflectometers [57].

A schematic diagram of a two-axis diffractometer is shown in Figure 3.1. The first axis of rotation is about the monochromator crystal M. A white beam of neutrons is incident on M, but by rotation of M to the Bragg angle θ_M and the monochromator-sample direction to $2\theta_M$, a single wavelength is selected. The second axis of rotation is about the sample S. Usually the sample has been aligned so that the desired crystallographic plane is in the horizontal scattering plane. It is then possible to rotate the sample to the correct Bragg angle θ_S for elastic scattering of neutrons of the given wavelength, and to rotate the detector to $2\theta_S$. The detector does not discriminate between elastic and inelastic scattering. However, the elastic signal always swamps the inelastic signal so that the configuration is suitable for diffraction measurements.

The collimators C_1, C_2 and C_3 and the mosaic spread of the monochromator η_M and the sample η_S determine the instrument resolution. There is always a trade off between narrow wave-vector transfer resolution and flux [57, 58].

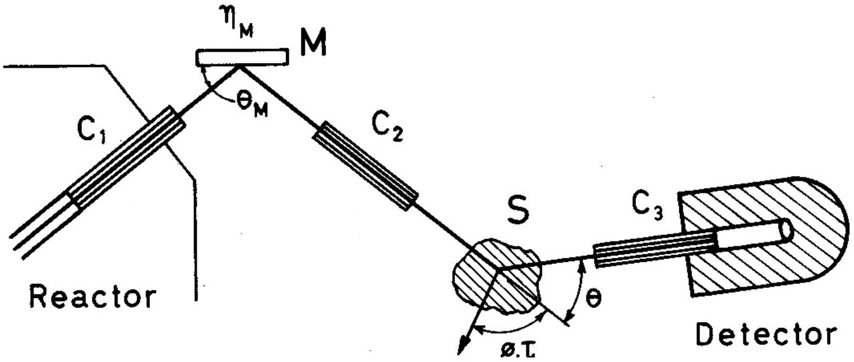

Figure 3.1: Schematic of a two-axis diffractometer, adapted from Gaulin [57]. S is the sample, M is the monochromator, C1, C2 and C3 are collimators. The incoming neutrons are collimated to produce a parallel beam. They are then monochromated to select a single wavelength before interacting with the sample. The beam is diffracted and the angle of diffraction is measured by the detector.

3.1.2 Neutron diffractometers

D15 thermal neutron diffractometer

D15 at the Institut Laue Langevin (ILL) in Grenoble is a single crystal diffractometer and can be used to solve a variety of problems including magnetic field and/or pressure induced phase diagrams as well as determining both nuclear and magnetic structures. Determining these structures requires the collection of a large number of Bragg reflections [59].

Three different wavelengths (and hence fluxes) are available and the instrument can be operated in normal beam or four-circle mode with a choice of monodetector or bidimensional microstrip detector. When using normal beam geometry either a 6T or 10T orange cryostat can be used. There is also the possibility of using 3GPa pressure cells, stress apparatus and furnaces [59]. See Figure 3.2.

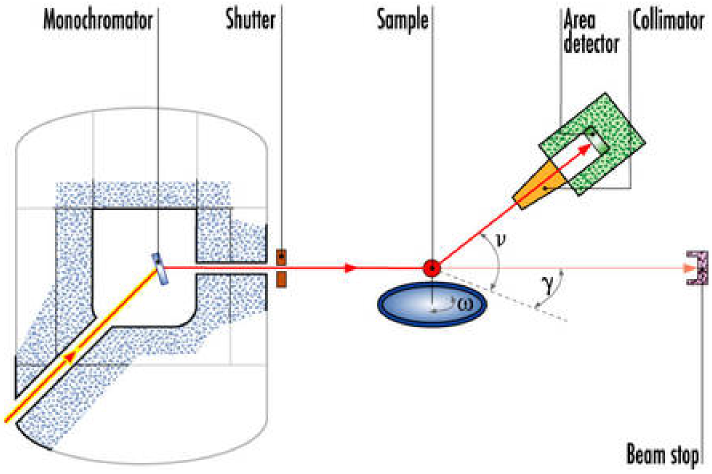

Figure 3.2: Schematic of the D15 thermal neutron diffractometer, taken from [59].

D10 four-circle diffractometer

D10 is a four-circle diffractometer at the ILL with the possibility of using energy analysis on three-axis spectrometers. Temperatures as low as T = 65mK can be reached using its four-circle cryostat and high reciprocal space resolution and low intrinsic background (or medium real space resolution) can be achieved. The cryostat allows the crystal to be easily orientated in the beam and the techniques are similar to those used in high altitude balloons and satellites [60]. See Figure 3.3.

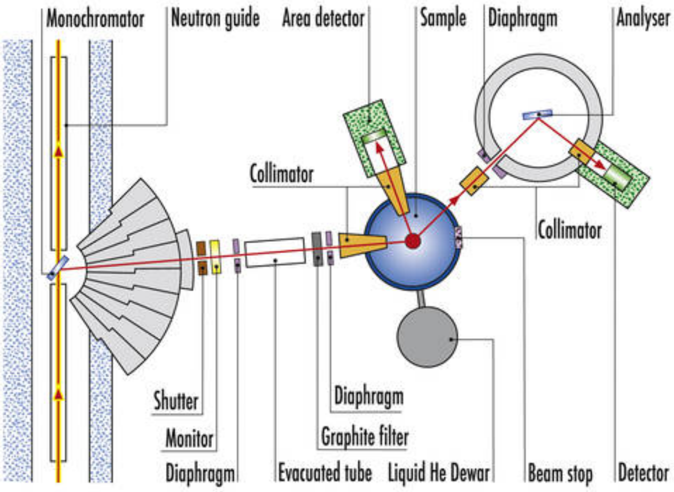

Figure 3.3: Schematic of the D10 four-circle diffractometer, taken from [60].

Neutrons are detected by a ^{3}He detector. The scattered neutron is absorbed by the pressurised gas which results in this reaction occurring:

$$ {}^{3}_{2}He + {}^{1}_{0}n \rightarrow {}^{3}_{1}H + {}^{1}_{1}p \tag{3.1} $$

The gas regenerates itself as the ${}^{3}_{1}$H decays back to ${}^{3}_{2}$He via β-decay. A helium cooled cryomagnet can be used to apply a field of up to $\mathbf{B} = 3$T. A pyrolytic graphic filter can be used to reduce background and remove higher order Bragg contamination [61].

D9 hot neutron diffractometer

This hot neutron source at ILL is close to the core of the nuclear reactor and hence produces neutrons with high incident energies which makes it especially useful as it allows strongly absorbing materials such as Gadolinium to be investigated since hot neutrons are more strongly penetrating than thermal neutrons, see Figure 3.4.

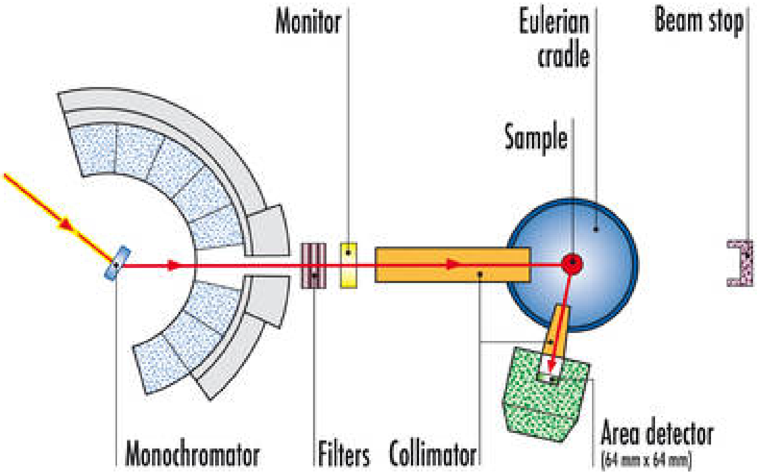

Figure 3.4: Schematic of the D9 hot neutron diffractometer, taken from [62].

Monochromators can be used to select the smallest wavelengths which allows a large area of **Q** to be investigated [62]. Structures can be more accurately determined as more Bragg reflections can be measured. D9 has a two-dimensional multidetector and is well suited for experiments which require high resolution nuclear density maps to give accurate analysis of the structure. Atomic displacements as small as 0.001Å can be discerned because of the short neutron wavelength [62]. It uses an Eulerian cradle sample holder with four-circle geometry which allows the sample to be positioned accurately in any orientation in the beam. Displex, He-flow cryostats, furnaces and cryomagnets can be used to achieve various temperatures and magnetic fields [62].

3.1.3 Operating principles of triple-axis spectrometers

The triple-axis spectrometer (TAS) was developed by Bertram Brockhouse in 1961 [63]. It is used at reactor sources for carrying out inelastic scattering experiments. The TAS has the first and second axes described in Section 3.1.1. In addition, it has a third axis centred on the analyser crystal A, see Figure 3.5.

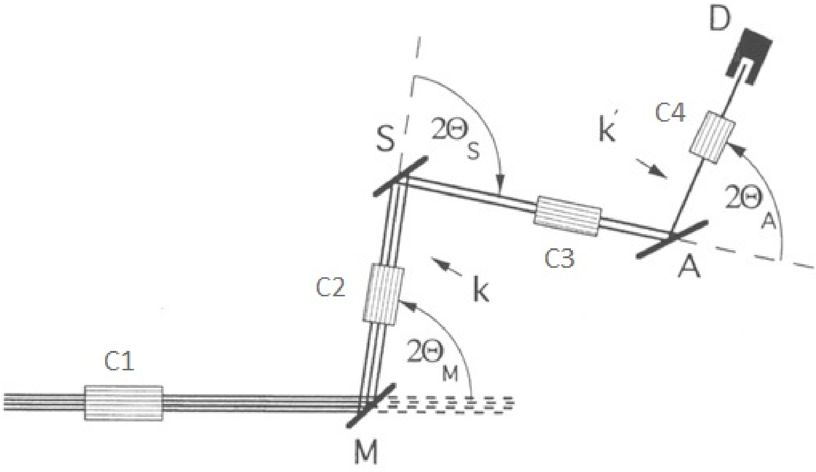

Figure 3.5: Schematic of a triple-axis spectrometer, adapted from [64]. M is the monochromator, S is the sample, A is the analyser, C_1, C_2, C_3 *and* C_4 are collimators and D is the detector. The incoming neutrons are collimated to produce a parallel beam. They are then monochromated to select a single wavelength before interacting with the sample. The beam is diffracted by an angle $2\theta_S$ and the final wavelength is measured by the analyser crystal before being counted by the detector.

The direction of the final wavevector is determined by the scattering angle of the diffracted beam from δ - A. The TAS can be set to measure neutrons of a given final wavelength by rotating the analyser crystal to the Bragg angle θ_A and the A-D direction to $2\theta_A$. The angles of the monochromator and analyser crystals can both be changed independently which allows neutrons with a large range of energy and momentum to be measured [7, 13, 63].

The angles θ_M, $2\theta_M$, θ_S, $2\theta_S$, θ_A and $2\theta_A$ are adjusted to probe a particular point in reciprocal space $(\mathbf{Q}, \hbar\omega)$. Figure 3.6 shows the scattering triangle. In this thesis the final energy of the neutron was chosen to remain fixed in inelastic TAS scans to make the corrections to the data more reliable.

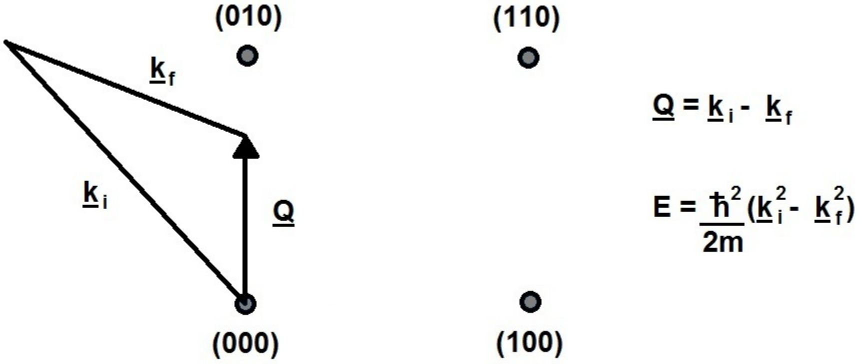

Figure 3.6: The scattering triangle. The magnitude of the incident wavevector k$_i$ is determined by θ_M and $2\theta_M$. In general, θ_S, $2\theta_S$, θ_A and $2\theta_A$ need to be adjusted for a given wavevector transfer and energy transfer.

The wavevector and energy transfer resolutions are determined by the collimators, C_1, C_2, C_3 and C_4, the mosaic of the monochromator, sample and analyser, and the sense of rotations. Highest resolution is achieved with the 'ω' configuration shown in Figure 3.2. For flat regions of the dispersion it is best to perform constant Q scans, whereas for steep regions of the dispersion it is better to scan Q holding E fixed. These instruments can also be used to measure quasielastic energy broadening of diffuse scattering, and in this case constant Q scans are required. [13, 63, 64]

The use of monochromator and analyser crystals can lead to spurions caused by higher order effects but these can be reduced by using filters. Although the use of TAS is slow and requires expert knowledge, there are many advantages of using this instrument. The experiment can be focussed on the area of reciprocal space that is important. Measurements can be carried out along high-symmetry directions and the parallel-perpendicular polarisation method can be used to separate magnetic and phonon signals [13,63–65].

3.1.4 Triple axis spectrometers

IN20 triple axis spectrometer

This thermal neutron three-axis spectrometer at the ILL is used for inelastic scattering experiments and can be used with magnets up to $\mathbf{B} = 15\mathrm{T}$, see Figure 3.7.

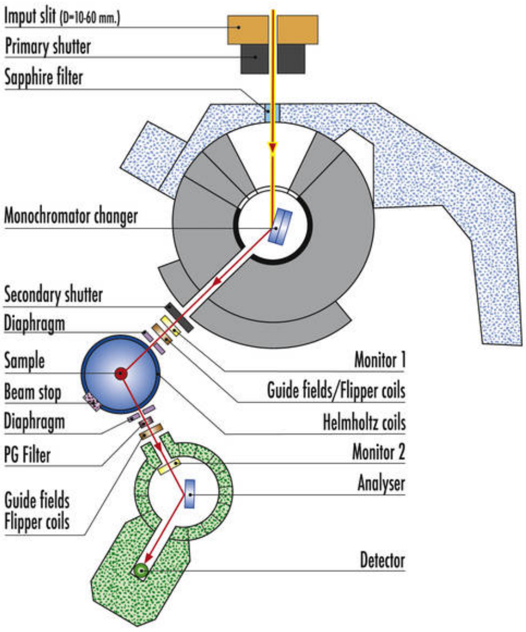

Figure 3.7: Schematic of the IN20 triple axis spectrometer, taken from [66].

High resolution linewidth studies of dispersionless excitations can be investigated using TASSE, the spin echo technique. Full polarization analysis can be employed using CRYOPAD [66]. XYZ polarisation analysis can be employed where Heusler (111) crystal monochromators are used to select the neutron energy and spin state and a Heusler (111) analyser is used to determine the properties of the scattered beam. It has a single ^{3}He detector and parallel-perpendicular polarisation analysis can also be used. For this, Helmholtz coils are placed around the sample and a field of about 15 Gauss can be applied in any direction [66].

3.1.5 Time-of-flight spectrometers

At a pulsed neutron source such as ISIS the TAS design is inappropriate since it does not exploit the available neutrons efficiently. Instead new types of spectrometers have been developed that collect neutrons in large banks of detectors and use is made of the time-of-flight of the neutron to determine its energy. There are two types of spectrometer, direct geometry (where the incident energy is selected and the final energy is calculated from the time-of-flight) and indirect geometry instruments (where the final neutron energy is selected). During the course of this thesis a direct geometry time-of-flight spectrometer was used.

The incident beam is monochromated using a velocity selector called a 'chopper'. A rotating absorbing disc has a hole that allows neutrons to pass through once per revolution. This is synchronised with pulses of neutrons so that the time-of-flight from moderator to chopper only allows neutrons of one wavelength to pass [49].

For a given orientation of the sample, the direction of $\mathbf{k}_i$ is fixed, and the magnitude is fixed by the chopper. For each detector, the direction of $\mathbf{k}_f$ is fixed, but the magnitude of $\mathbf{k}_f$ varies and it is determined by the time-of-flight. Thus each detector measures the scattered intensity for an arc in reciprocal space.

Data can be acquired much more efficiently if it is collected in arrays of detectors. Combining detectors in a one-dimensional array allows the intensity of scattered neutrons to be measured simultaneously over a surface of reciprocal space in the scattering plane. By using an area detector information is obtained in the third spatial dimension. Information can be obtained very efficiently in this way from two-dimensional systems, such as spin chains and two-dimensional magnets, by appropriate orientation of the sample.

For the three-dimensional system studied in this thesis the rotational method is used. Data is acquired in a large area detector and the sample is rotated about a vertical axis. In this way a four dimensional data set is obtained. The steps in the rotation need to be small enough, typically 5°, so that there are no gaps in the data. The angular range is determined by the symmetry of the crystal, so that 90° is sufficient for a cubic system.

In order to visualise the data specialist software is required, in this case Horace [67]. Because the rotational method gives the complete four-dimensional data set, any cuts in reciprocal space can be obtained. Furthermore, it generates a huge data set for comparison with theory. A complete survey of reciprocal space is also attractive since it also yields any additional features that have not been anticipated, increasing the likelihood of discovering new science [68].

MAPS spectrometer

The TOF instrument used during the course of this thesis was the direct geometry MAPS spectrometer at ISIS (See Figure 3.8). MAPS at ISIS in Oxfordshire has been designed specifically to measure high energy magnetic excitations in single crystals. Vast areas of the Brillouin zone can be mapped out due to its very large array of position sensitive detectors which give almost continuous coverage over a large solid angle [68].

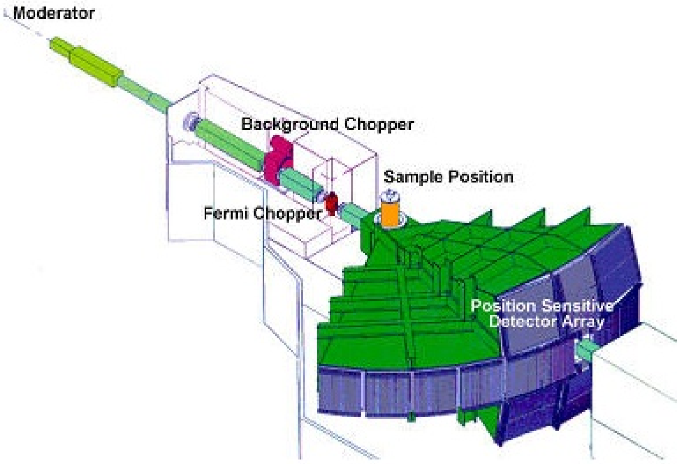

Figure 3.8: Schematic of the MAPS spectrometer, taken from [68].

MAPS uses a range of incident energy between 15-2000 meV and has a Fermi Chopper situated 10m from moderator. Sample position is 12m from the moderator [68].

The monochromated neutrons interact with the sample (where they lose or gain energy, resulting in a velocity change) and are scattered to the detector [63]. The detectors are position sensitive ^{3}He tubes positioned 6m from the sample position. They consist of a 16m^2 array of 147,456 pixel elements [68].

The neutron transfers energy E and momentum Q to the sample and hence the scattering function S(Q,E) can be mapped out. Momentum transfer can be calculated using the cosine rule [49]:

$$Q^2 = k_i^2 + k_f^2 - 2 \cdot k_i \cdot k_f \cdot \cos\theta \tag{3.2}$$

where k$_i$ is the incident wavevector, k$_f$ is the final wavevector and θ is the scattering angle [49].

3.2 X-ray instruments

ID20 single crystal diffractometer

ID20 at the European Synchrotron Radiation Facility (ESRF) in Grenoble is designed for investigating magnetic, charge and orbital ordering properties of solids. The following techniques can be implemented : Polarization Analysis (PA), Non Resonant Magnetic X-ray Scattering (NRMXS) and Resonant X-ray Scattering (RXS). PA allows the magnetic signal to be isolated and the magnetic moment direction can be determined. Use of an X-ray phase plate allows the polarisation of the incident beam to be controlled. ID20 can be used to scan an element's absorption edge with very good resolution (1eV) and harmonics can be removed via the use of two mirrors. In addition, many sample environments can be maintained; low temperature, pressure and high magnetic fields [54]. Situated on an insertion device, it has a very large signal with which to detect the usually very weak magnetic scattering.

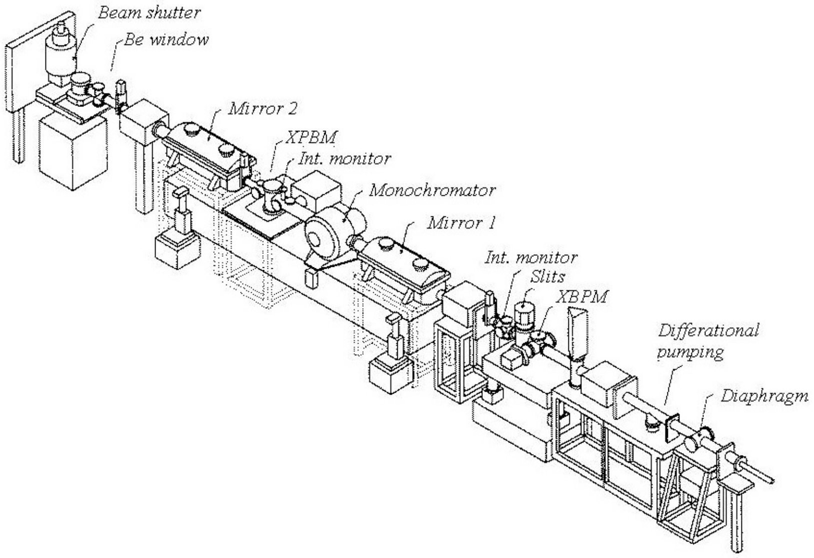

Figure 3.9: Schematic of the ID20 single crystal diffractometer, taken from [54].

XMaS single crystal diffractometer

The **X**-ray **Ma**gnetic **S**cattering (XMaS) beamline, (otherwise known as BM28) at the ESRF can be used for high resolution and magnetic single crystal diffraction over an energy range of 2.3 to 15keV. It is situated on a bending magnet and as a consequence is less sensitive than ID20. However, provided the signal is sufficiently large, it is a very versatile instrument with a flexible sample environment. The white synchrotron radiation is monochromated by the use of a watercooled Si (111) crystal monochromator. It has a diamond phase plate, to enable the polarisation to be changed as required, and a polarisation analyser. Temperatures of T = 1-1200K can be achieved and a 1T magnet for both vertical and horizontal scattering geometries can be utilised [69].

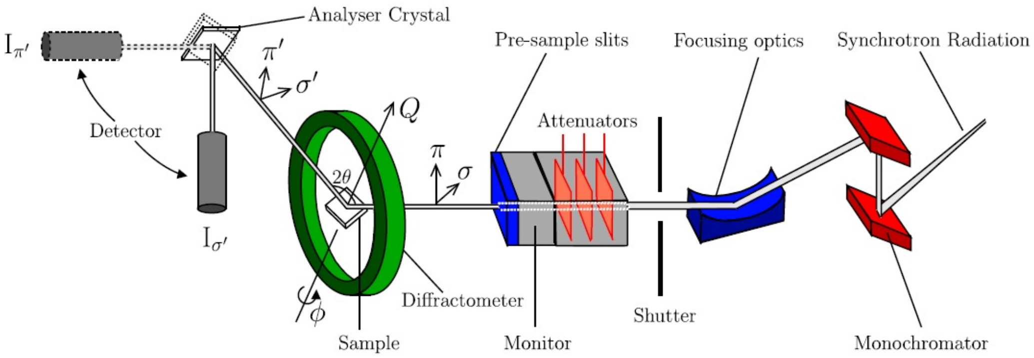

Figure 3.10: Schematic of the XMaS single crystal diffractometer, taken from [53] who adapted diagram from [70].

Several detectors are available: standard scintillator detector, avalanche photodiodes, Si drift diode and a MarCCD is also available. A 4T superconducting magnet for horizontal and vertical scattering geometries can also be utilised [69].

3.3 SQUID

A SQUID (Superconducting Quantum Interference Device) makes use of the Josephson Effect to measure extremely small voltages, currents and magnetic fields and allows the total sample magnetisation to be measured very accurately.

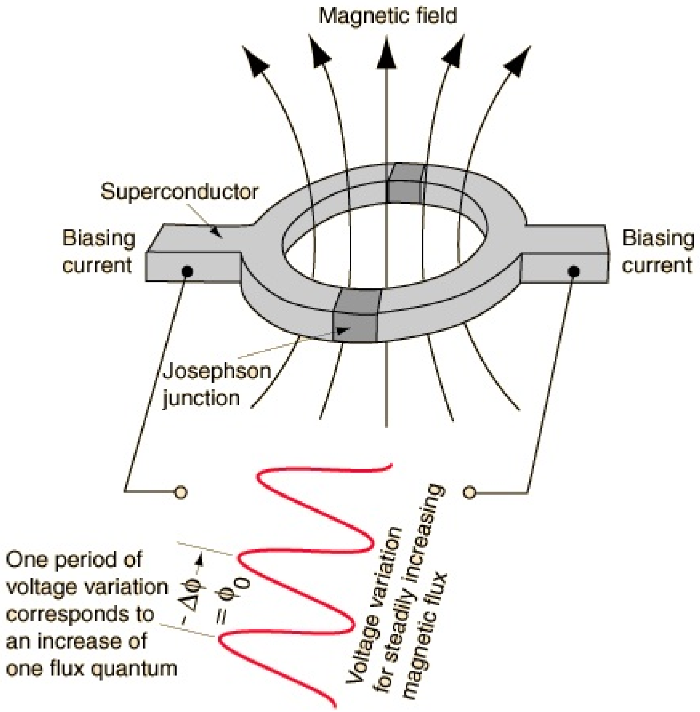

Figure 3.11: Schematic of a SQUID magnetometer. Taken from [71].

The Josephson Effect is a name for any of the phenomena that occur when a current flows through a thin insulating layer between two superconducting substances when the temperature is sufficiently low. The very thin film of insulating material between the superconductors is known as the Josephson Junction. As a result of the Tunnel Effect, electrons forming part of the current are able to move across this junction. The d.c. Josephson Effect is when the current can flow across the junction without the application of an externally applied voltage. The superconducting current in a SQUID can be highly sensitive to the effect of an external magnetic field in certain configurations. Hence it can be used as an extremely fast electronic switch with very low power dissipation. Measurements can be taken over a temperature range of T = 1.8 - 300K and a magnetic range of B = 0 - 7T. Graphs of longitudinal moment (emu) against temperature (K) are plotted to determine the magnetisation in the sample to great accuracy.

4 MnV$_2$O$_4$ structure

4.1 Background

4.1.1 Crystal structure of MnV$_2$O$_4$

MnV$_2$O$_4$ has a spinel structure comprising a network of corner-sharing tetrahedra in which the vanadium ions form a pyrochlore lattice, this is typical of systems that are geometrically frustrated in three dimensions [33, 34, 38, 42–45, 72–74].

In the case of MnV$_2$O$_4$, the V^{3+} 3d electrons occupy two out of three t$_{2g}$ orbitals and, therefore, the orbital degrees of freedom come into play leading to complicated magnetic ordering and excitations [41–45, 74–76]. The presence of the magnetic manganese ions leads to a ferrimagnetic structure and hence it is potentially possible to control both the magnetism and the orbital physics via an applied magnetic field.

Although it has been agreed that the high temperature structure is Fd$\bar{3}$m, as shown in Figure 4.1, there has been debate as to whether the low temperature

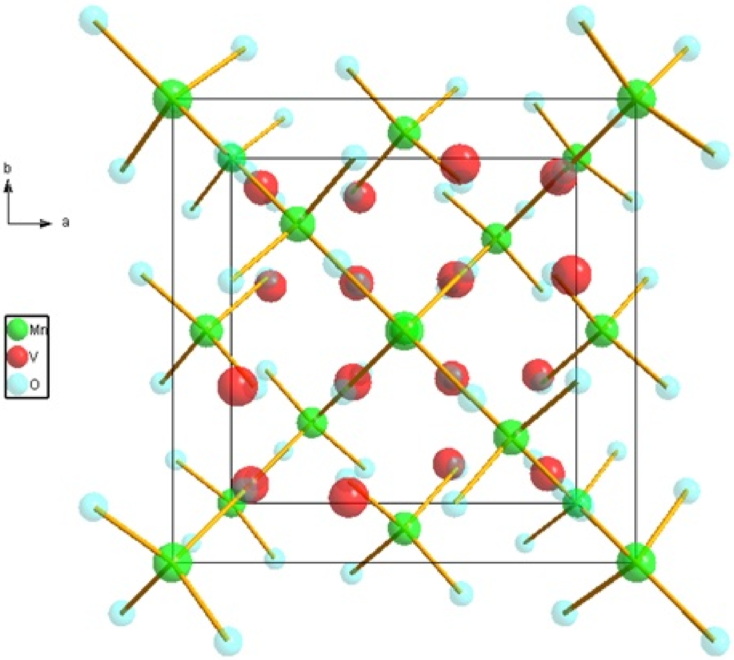

Figure 4.1: The Fd$\bar{3}$m cubic crystal structure of MnV_2O_4 at room temperature. (Produced using Diamond software from Crystal Impact [77]).

tetragonal structure of MnV_2O_4 is I4_1/amd [38–40] or I4_1/a [33, 41, 42]. This has been solved by single-crystal X-ray diffraction by Suzuki *et al.* who measured weak reflections at the Photon Factory, KEK in Japan [75]. In an I4_1/amd structure the (802) and (421) peaks are both forbidden, but for I4_1/a only the (421) is forbidden. Suzuki's results, shown in Figure 4.2, show the (802) peak clearly and the absence of the (421) thus proving that the structure is I4_1/a [75].

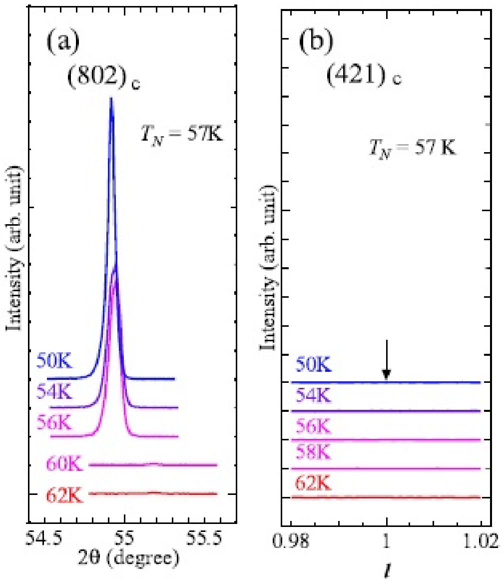

Figure 4.2: Results from Suzuki *et al.*showing the temperature dependence of X-ray diffraction of the MnV$_2$O$_4$ single crystal around (a) the (802) peak and (b) the (421) absence (in the cubic setting) [75].

This result proves that the low temperature tetragonal structure is I4$_1$/a. A structural phase transition from the cubic to the tetragonal phase occurs at T$_N$ = 57K and the results suggest that this transition is dominated by the orbital degrees of freedom, and that they interact with the spin [75].

4.1.2 Orbital ordering of MnV_2O_4

In MnV_2O_4 the Manganese ions (Mn^{2+}) have spin $S = \frac{5}{2}$ and no orbital degrees of freedom, the Vanadium ions (V^{3+}) have spin S = 1 and the d_2 electrons occupy two out of three t_{2g} levels [41–45, 74–76]. Three possible orbital orders have been proposed. The first by Tsunetsugu and Motome, see Figure 4.3, presumes tetragonal distortion which lowers the energy of the d_{xy} level and predicts staggered occupation of d_{yz} and d_{zx} orbitals leading to antiferro-orbital order and $I4_1/a$ structure [33].

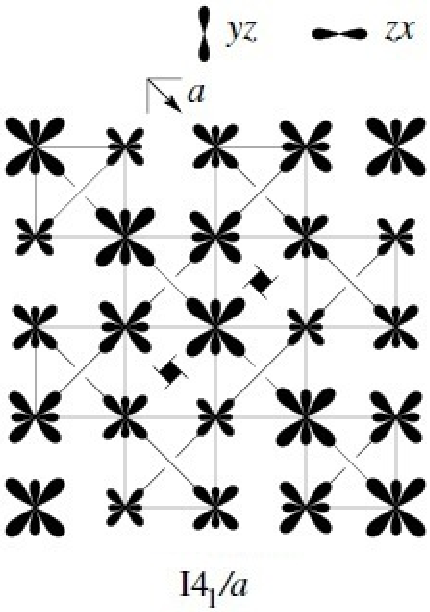

Figure 4.3: The orbital order of vanadium ions below the structural phase transition, viewed down the (001) direction. As proposed by Tsunetsugu and Motome [33]. Ions which are further away are smaller. After Tchernyshyov *et al.* [38].

The second by Tchnernyshyov *et al.*, predicted equal occupation of d_{yz} and d_{zx} orbitals and hence ferro-orbital order and $I4_1$/amd structure (again presuming tetragonal distortion) [38]. See Figure 4.4.

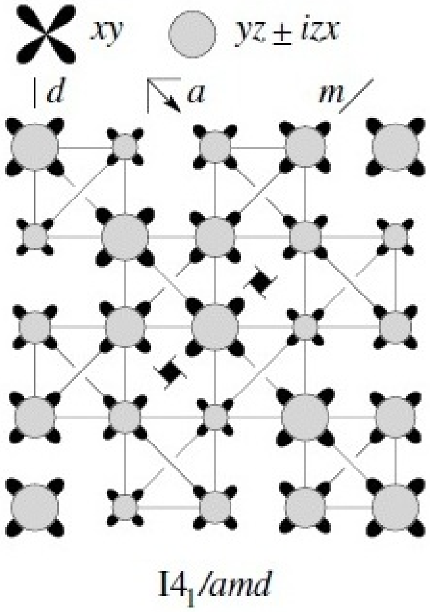

Figure 4.4: The orbital order of vanadium ions below the structural phase transition, viewed down the [001] direction. Ions which are further away are smaller. As proposed by Tchernyshyov *et al.* [38].

Lastly Sarkar *et al.* used density functional calculations with all t_{2g} levels partially occupied which predicted orbital chains running along a and b, ferro-orbital order and $I4_1/a$ structure. A staggered trigonal distortion causes the orbitals within each chain to be rotated alternately by 45° [41].

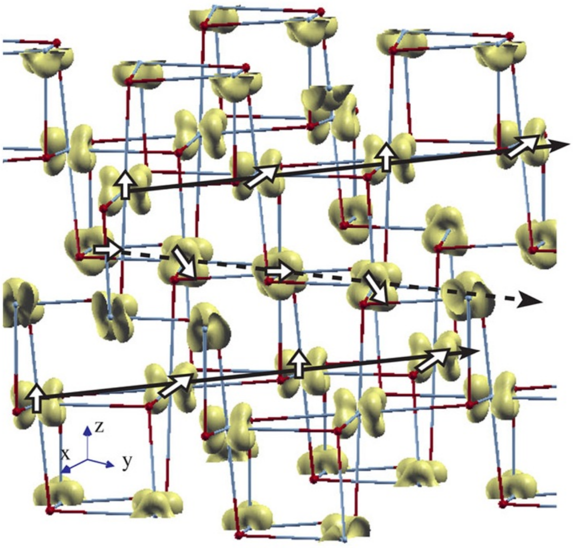

Figure 4.5: Orbital ordering as predicted by Sarkar *et al.* [41]. The black solid and dashed lines show the orbital chains and the arrows show the orbitals within each chain rotated alternately by 45°.

Experiments were carried out in order to determine which of these models is correct.

4.1.3 Magnetic structure of MnV_2O_4

The magnetic structure of MnV_2O_4 was first solved by Plumier *et al.* [36,37] using powder neutron diffraction. MnV_2O_4 exhibits ferrimagnetic ordering below $T_N = 57K$, where the Mn and V moments align in opposite directions along [001], Figure 4.6 (a). There is a change in this collinear configuration to a non-collinear 'triangular' magnetic structure with vanadium moments lying in (H00) sheets below $T_M = 53K$, Figure 4.6 (b). The fitted angle of canting of the V^{3+} moments, μ is 63° [36, 37].

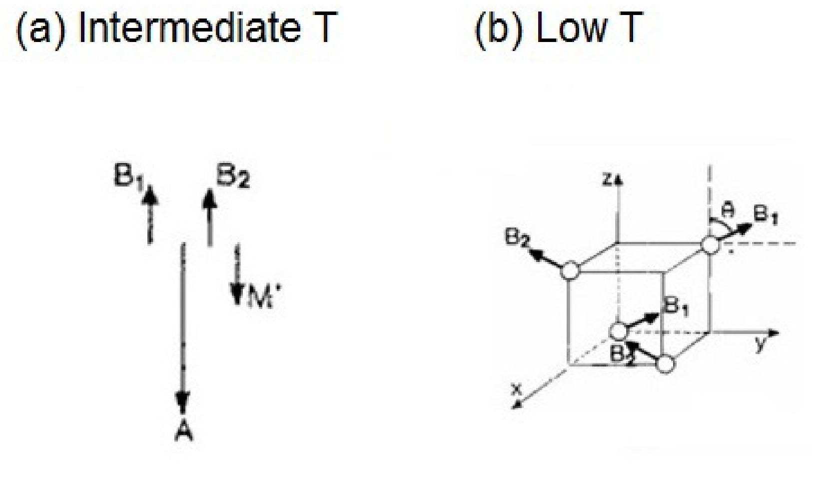

Figure 4.6: (a) The collinear ferrimagnetic ordering of MnV_2O_4 at intermediate temperature; (b) The triangular magnetic structure at low temperature. After Plumier *et al.* [37]. The moments shown are those of the V^{3+} ions at the B sites. The Mn moments at the A sites are along the c direction, in the opposite direction to the ferromagnetic component on the vanadium sites, as is the resultant magnetization.

However, it was later deduced that this ground state was incorrect when Garlea *et al.* resolved the magnetic structure of MnV_2O_4 using high-resolution powder neutron diffraction at NIST. Garlea proposed that the V^{3+} moments have antiferromagnetic components in the ab plane, staggered along the c axis, (angle of canting of V^{3+} moments from c axis, $\theta = 65.12°$) [42].

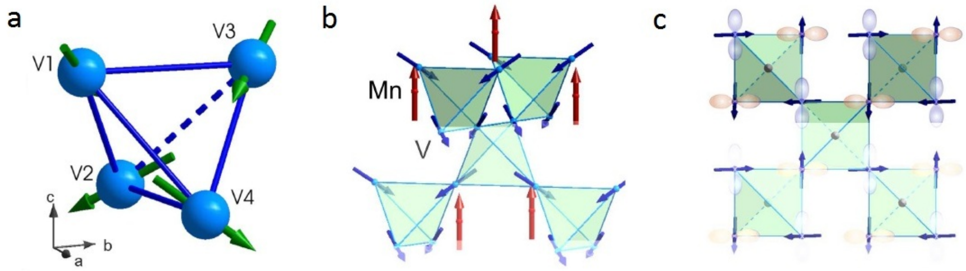

Figure 4.7: (a) and (b): Low-temperature non-collinear ferrimagnetic structure of MnV_2O_4. The Mn moments are aligned parallel to the c axis, while the V moments are canted by approximately 65°. (c) Projection of the magnetic structure on the tetragonal basal plane. After Garlea *et al.* [42].

4.2 Experimental procedure

Single crystals of MnV_2O_4 were grown by Le Duc Tung using the floating-zone technique at the University of Warwick. X-ray diffraction studies at the University of Liverpool confirmed the high structural quality. Several small crystals were produced for bulk physical property measurements and diffraction experiments and one large 6g crystal was produced for inelastic scattering experiments.

XMaS experiment

Single-crystal resonant X-ray scattering was performed on the XMaS beamline at the ESRF with the aid of Laurence Bouchenoire, Peter Normile and Paul Thompson. Samples were polished to obtain a flat (111) plane. The experiment was carried out in the vicinity of the vanadium K edge.

D10 experiment

The magnetic structure of MnV_2O_4 was determined using zero field measurements performed in the D10 cryostat at the ILL. Many reflections could be accessed but at zero field MnV_2O_4 has multiple domains. Single-crystal neutron scattering experiments were completed with Garry McIntyre and Bachir Ouladdiaf using an MnV_2O_4 single crystal aligned with the (100) plane perpendicular to the crystal surface. An energy of 52meV was used and structure factor scans were performed at T = 2K, 57K, 75K and 295K. The details of the magnetic structure determined on D10 are a prerequisite to model the orbital ordering using *ab initio* calculations. A low wavelength of 1.25Å was used to enable a large number of structure factors to be measured.

D15 experiment

The Néel temperature was determined using single-crystal neutron diffraction on D15 at the ILL and a cryomagnet was used to map out the phase diagram. The experiment was carried out with Garry McIntyre using an energy E = 52meV and a wavelength λ = 1.2Å. Measurements were performed at zero field in the cryomagnet to compare directly with the measurements on D10. The sample was placed in the cryomagnet with the (100) plane perpendicular to the crystal surface giving (HK0) in the horizontal scattering plane. About 270 structure factors were measured at T = 2K and 70K. A 2T field was applied along the [001] direction and 284 structure factors were measured at T= 2K. The field was applied in the paramagnetic phase at T= 70K.

4.3 Results

4.3.1 SQUID results

Figure 4.8 shows the bulk single-crystal magnetic susceptibility results obtained using an MPMS SQUID magnetometer at The University of Liverpool. The magnetic transition temperatures can be seen at T_N = 57K and T_M = 53K.

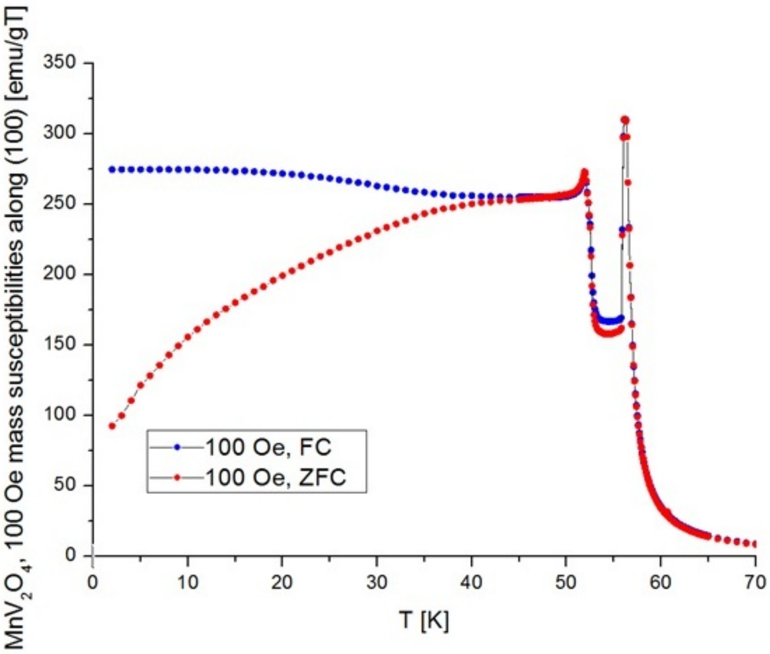

Figure 4.8: Magnetic susceptibility of MnV_2O_4 using a field of 100 Oe applied in the [100] direction. The magnetic transition temperatures can be deduced from the sharp features at T_N = 57K and T_M = 53K.

Single crystals allow the magnetic susceptibilities to be studied as a function of the direction of magnetic field applied along [100], [011] and [111], see Figure 4.9.

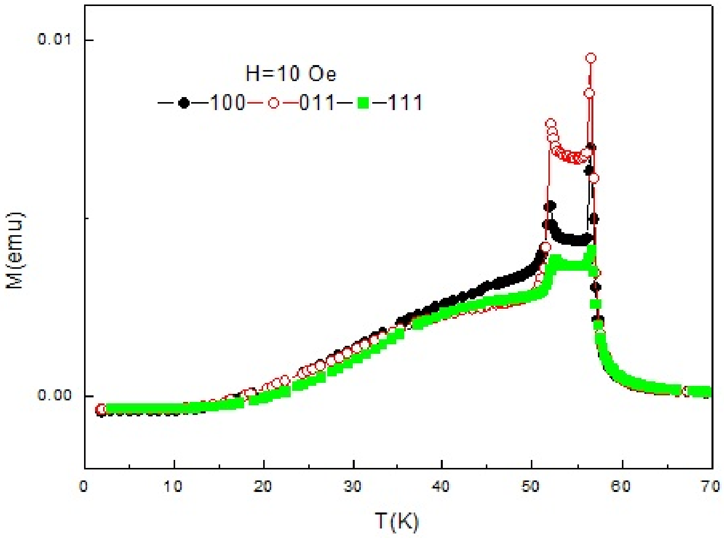

Figure 4.9: Magnetisation of MnV_2O_4 with applied field along [100], [011] and [111]. Transitions can be seen at $T_N = 57K$ and $T_M = 53K$. Measurements performed by Le Duc Tung.

Again, the zero-field magnetic phase transitions are at $T_N = 57K$ and $T_M = 53K$. The hysteresis measurements give the same behaviour for fields applied in [001] and [110] cubic directions. The temperature dependencies show two clear transition temperatures in small fields. However at fields of $B = 2.5$ T and above, the [001] and [110] directions follow each other and show only one transition whereas the [111] direction maintains two decipherable transitions throughout and hence is used to produce the phase diagram (Figure 4.20).

Hysteresis

SQUID measurements of MnV_2O_4 show a small hysteresis, of about 1K, between warming and cooling as shown in Figure 4.10. Cooling measurements only were used to produce the phase diagram.

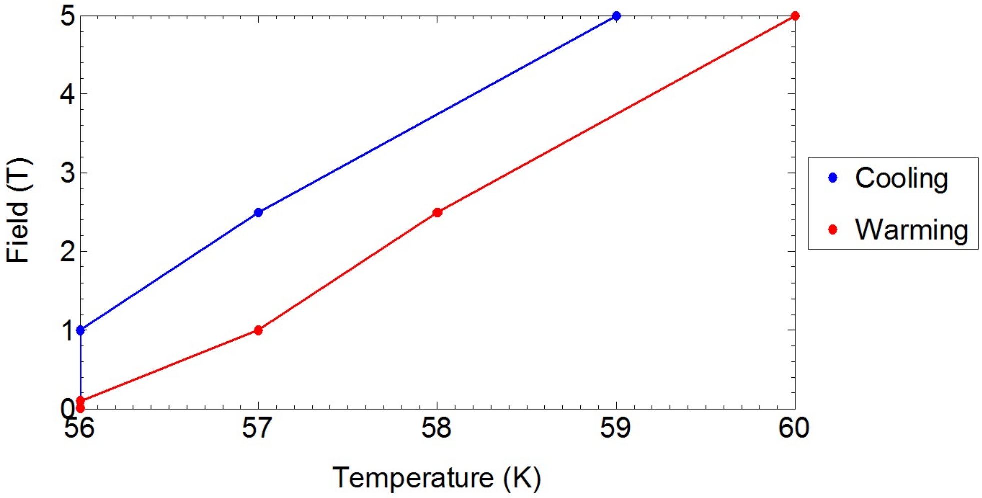

Figure 4.10: SQUID measurements of MnV_2O_4 showing a small hysteresis, of about 1K, on heating and cooling.

4.3.2 XMaS results

The experiment was carried out in the vicinity of the vanadium K edge as can be seen in Figure 4.11(c). Di Matteo *et al.* [74] used the FDMNES program to perform a numerical simulation calculating the intensity of signal produced by complex orbital occupancy for CdV_2O_4, the result of which can be seen in Figure 4.11(b). This calculated orbital ordering is the same as that proposed by Tchernyshyov [38]. Our results show no peak at the (111) position (Figure 4.11 (a)). This null result is consistent with the results of Suzuki *et al.* [75], which rules out the ferro-orbital model of Tchernyshyov [38]. Di Matteo *et al.* predict no peak for the orbital ordering models with space group $I4_1/a$ [74].

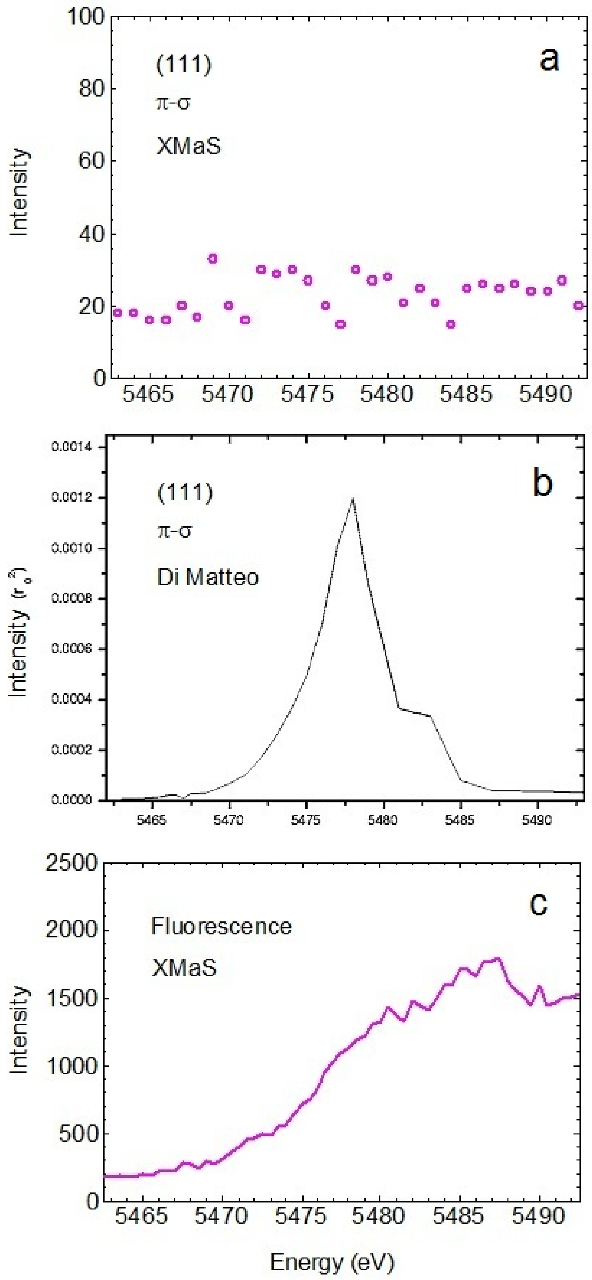

Figure 4.11: (a) XMaS data for MnV_2O_4 at (111) showing the absence of a peak. (b) The calculated intensity at (111) from the ferro-orbital model of Tchernyshyov [38] from Di Matteo [74] and (c) the Vanadium edge fluorescence scan.

The cubic-to-tetragonal phase transition was studied using an MnV_2O_4 (100) sample and T_S was determined as a function of applied magnetic field.

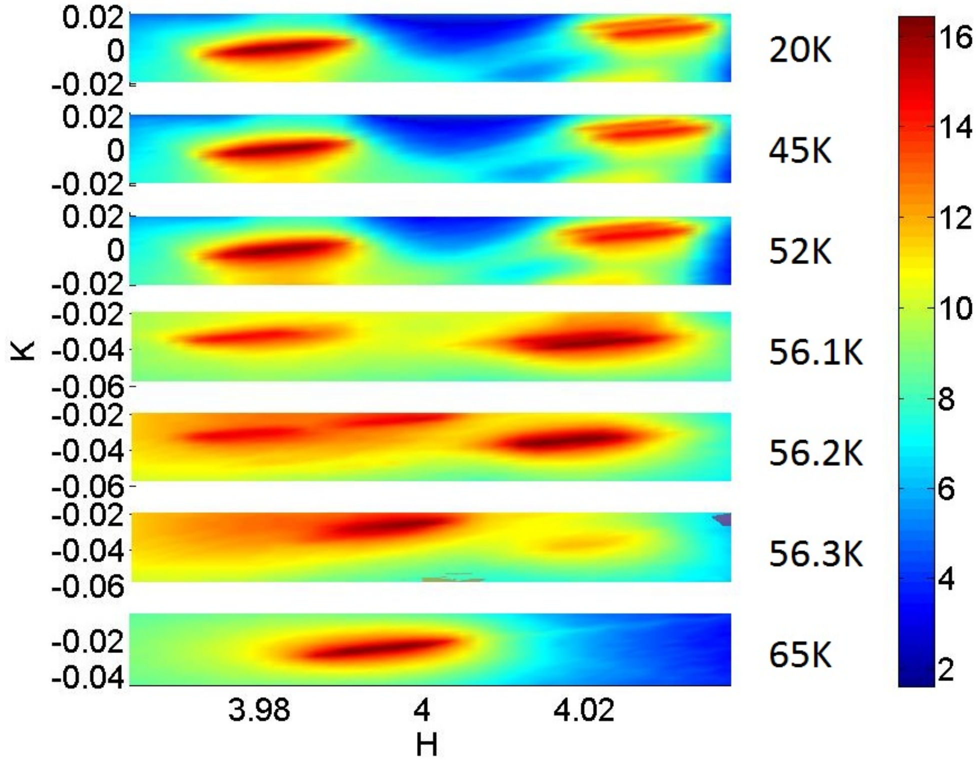

Figure 4.12: (H,K) mesh plot at 0T showing the temperature dependence of the MnV_2O_4 structural (400) peak. The structure changes from the cubic phase at 65K to the tetragonal phase at 56.1K and below. Coexistence of these phases can be seen at 56.2K and 56.3K.

The data from these mesh plots is shown in Figure 4.12 and the formation of two peaks indicates the transition from the cubic to the tetragonal phase. Figure 4.13, shows h-scans and the fitted peak positions. From these data the transition temperature is estimated to be $T_S = 56.3 \pm 0.2$ K. Figure 4.14 shows the fitted peak positions as a function of applied field. These XMaS data are used to produce the MnV_2O_4 phase diagram shown in Figure 4.20.

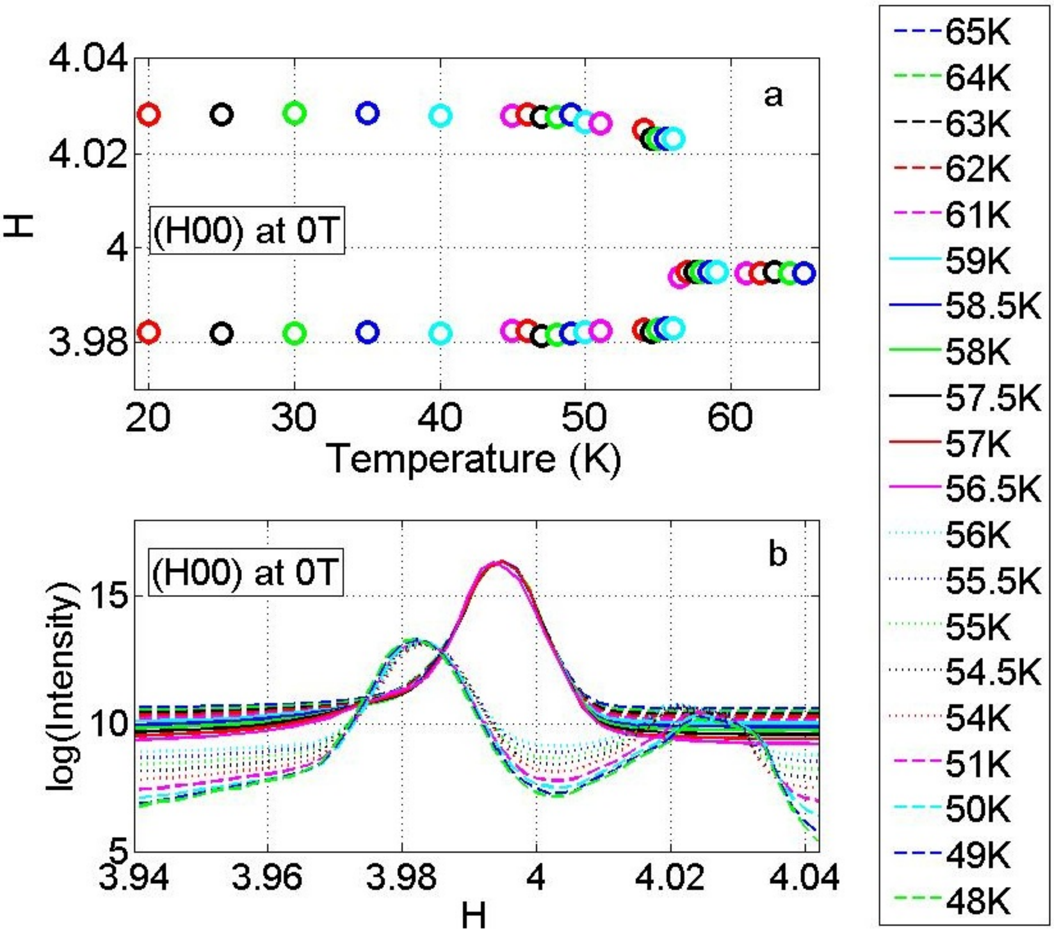

Figure 4.13: (a) and (b) The temperature dependence of the MnV_2O_4 (400) peak at B = 0T from XMaS. The structural transition can clearly be seen where the crystal changes from tetragonal (double peak) to cubic (single peak) as the temperature increases.

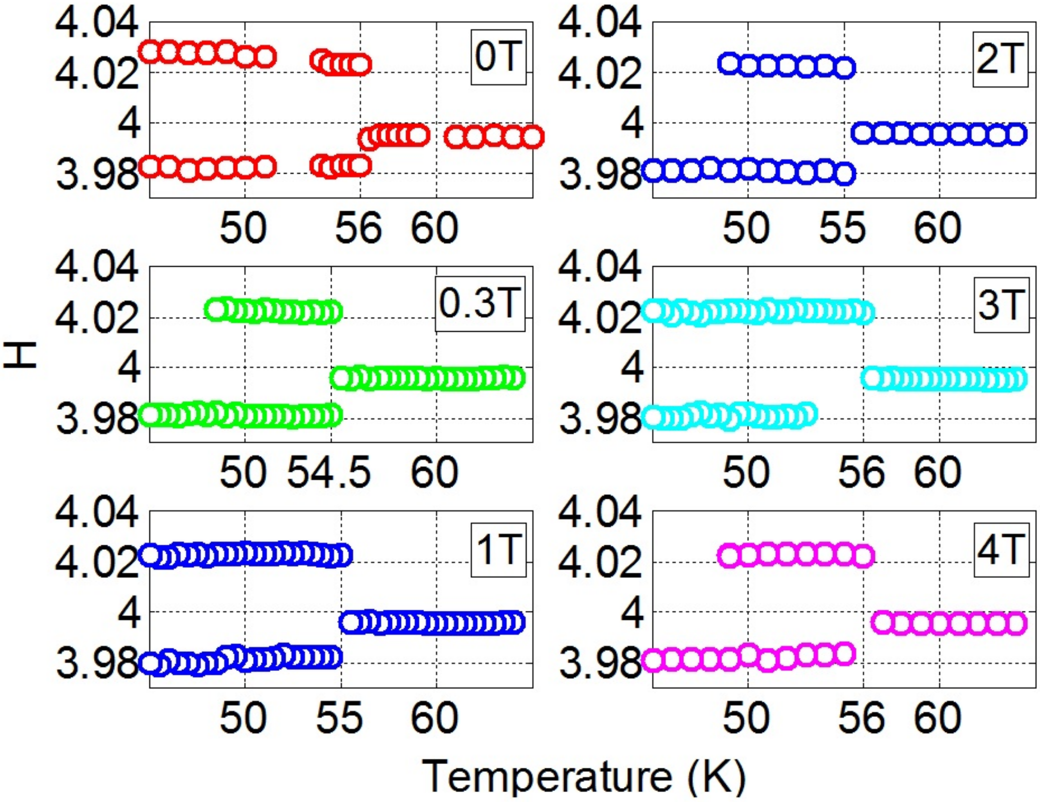

Figure 4.14: XMaS results showing the temperature dependence of the position of the MnV_2O_4 (400) structural peak at various fields (temperature decreasing).

4.3.3 D10 results

The following refinement of the zero-field magnetic structure was carried out by Garry McIntyre at the ILL. The absorption correction was calculated by following the method described by Coppens, Leiserowitz and Rabinovich [78].

	T = 75 K $Fd\bar{3}m$	T = 2 K $I4_1/amd$ (untwinned)
a [Å]	8.5117(5)	8.5142(8)
Mn1		
(x, y, z)	$(\frac{1}{8}, \frac{1}{8}, \frac{1}{8})$	$(0, \frac{3}{4}, \frac{1}{8})$
B_{is}	0.108(63)	1.01(27)
V1		
(x, y, z)	$(\frac{1}{2}, \frac{1}{2}, \frac{1}{2})$	$(0, 0, \frac{1}{2})$
B_{is}	0.108(63)	1.01(27)
O1		
x	0.26306(10)	0
y	0.26306(10)	0.02424(89)
z	0.26306(10)	0.2619(12)
B_{is}	0.348(43)	1.13(18)
Observations	222	81
R1	4.470	11.01
R2	6.914	13.04
R3	3.680	13.82
R4	6.028	15.63
χ_2	15.4	129

Table 4.1: Structural refinement of MnV_2O_4 B_{IS} = Isotropic temperature factor

The following magnetic refinement was carried out assuming these magnetic form factors: Mn^{2+} $\langle j_0 \rangle$, V^{3+} $\langle j_0 \rangle$. The reflections are separated into two groups, those which are allowed by the structural space group and those which are not. Ferromagnetic components are in the structural reflections along with the antiferromagnetic components which are canted. Non-canted antiferromagnetic components go into other reflections. The scale factor, atom coordinates and thermal parameters are fixed.

	Ferromagnetic	Antiferromagnetic	Garlea et al.
$\mu_{Mn}(\mu_B)$	3.4(1.1)		4.2
$\mu_V(\mu_B)$	-0.96(79)	1.02(10)	1.3
ϕ_V		54.9(5.1)	65.12
Observations	53	28	
R1	12.07	37.49	
R2	21.60	31.48	
R3	11.21	17.18	
R4	14.30	20.03	
χ_2	133	22.2	

Table 4.2: Magnetic structure refinement of MnV_2O_4

In summary, Table 4.2 shows that the manganese moment, μ_{Mn}, is $3.4(1.1)\mu_B$, along the c direction, and the vanadium moment, μ_V, is $1.4(5)\mu_B$ canted with an angle, ϕ, of 54.9(5.1)° from the c direction. Basal plane components in each tetrahedra rotated by 90°. This is in good agreement with Garlea *et al.*, see Figure 4.7. The results of the magnetic moments calculated using McPhase (discussed in Chapter 5) also agree with this magnetic structure.

4.3.4 D15 results

Measurements in zero field

We started doing $\omega - 2\theta$ scans for our structure factor measurements and found multiple peaks. We realised that there was severe contamination by powder lines from the cryomagnet. Therefore we performed ω - scans so that any contribution from powder lines would appear as a flat background. The data set at B = 2T, T = 2K are ω - scans so we know that these data are reliable.

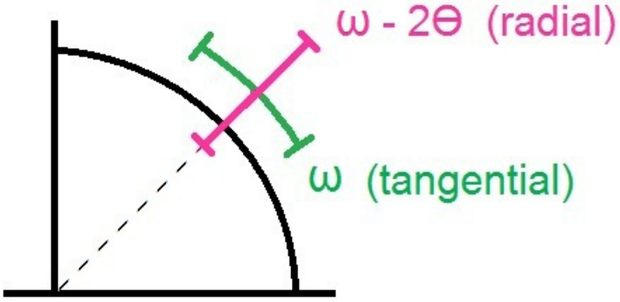

Figure 4.15: Scan directions used in the D15 experiment. Data from radial $\omega - 2\theta$ scans were difficult to use due to the presence of powder lines. Tangential ω - scans contain only a constant contribution from powder lines and so the peak intensities on top of a flat background are used.

The following temperature dependencies were obtained for the cubic (400) reflections (Figure 4.16) and (200) reflections (Figure 4.17). (These are (220) and (110) in the tetragonal phase).

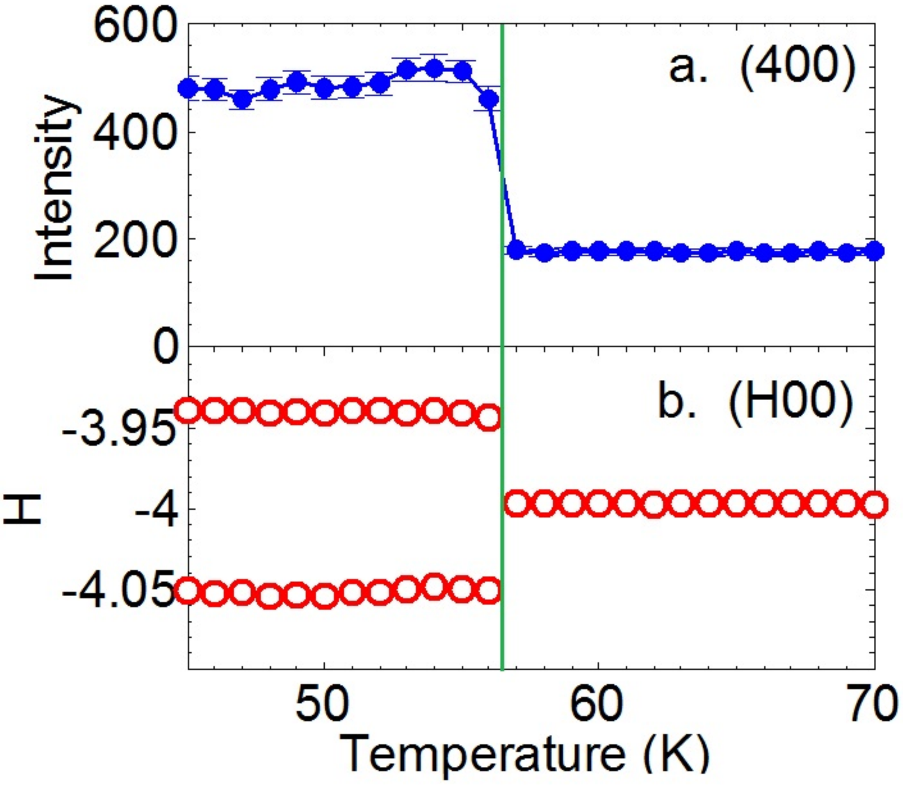

Figure 4.16: Temperature dependence of (a) the intensity and (b) the position of the (400) Bragg reflection at B = 0T. The peak splitting due to the tetragonal distortion occurs at 56.5K, the same temperature as the onset of magnetic ordering.

The temperature dependence of the **Q**-scans through the (400) reflection shows two peaks up to 56K in both the H and K directions, this is due to the presence of multiple domains. The structural transition can be seen to occur at 57K (where the double peak becomes a single peak). The **Q**-scans through the structural/magnetic (400) and purely magnetic (200) peaks all show domains below T_S = 57K. All our data sets imply a cubic-to-tetragonal distortion at T_S = 57K. We agree with Suzuki *et al.* [75], who performed single-crystal synchrotron measurements and determined T_S to be 57K. It also seems to be logical for the structural distortion to occur around T_S = 57K, when all agree that the system orders with a net ferromagnetic moment along the c direction. The (200) reflection arises from the non-collinear low temperature magnetic structure and it is not expected in the intermediate ferrimagnetic phase.

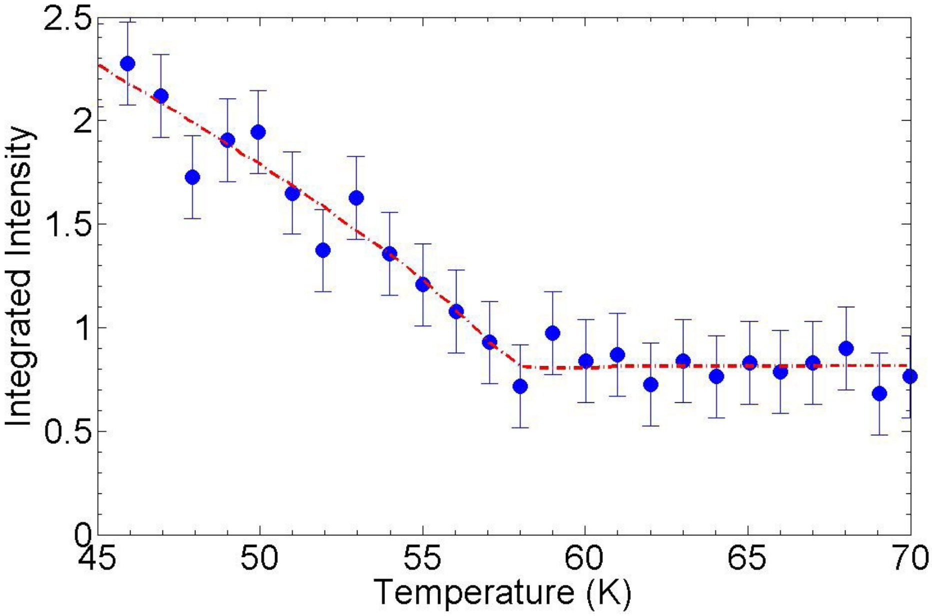

Figure 4.17: Temperature dependence of the intensity of the magnetic peak (200) at B = 0T.

The presence of a peak above T_M suggests the presence of higher order contamination. The increase in intensity from the magnetic ordering would be expected at $T_M \approx$ 53K. However, the fact that the higher order contamination will have an additional magnetic component below $T_N = 57K$ may explain the observed increase in intensity at (200) below T_N.

Measurements in a field

The measurements in a field were an attempt to map out the phase diagram and measure the magnetic structure for a single domain. The domains of MnV_2O_4 seen on D15 are shown in Figure 4.18. The Néel temperature, T_N, was determined as a function of applied magnetic field. The temperature dependence in a field was also measured. See Figure 4.19.

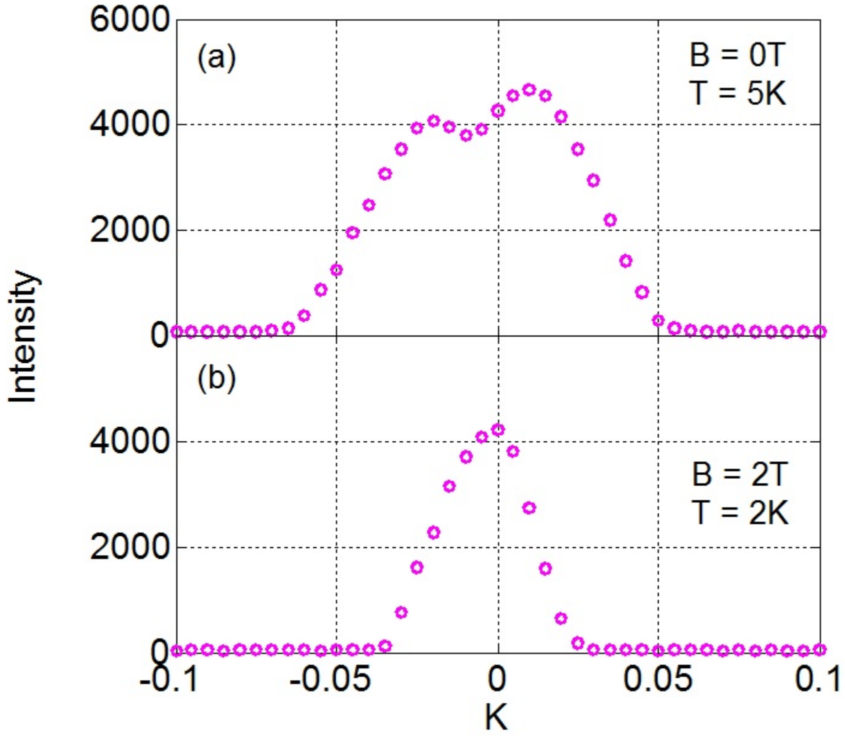

Figure 4.18: Domains of MnV_2O_4 seen on D15. At zero field the presence of domains is shown by the double peak. With a field of 2T applied the sample becomes a single structural and magnetic domain

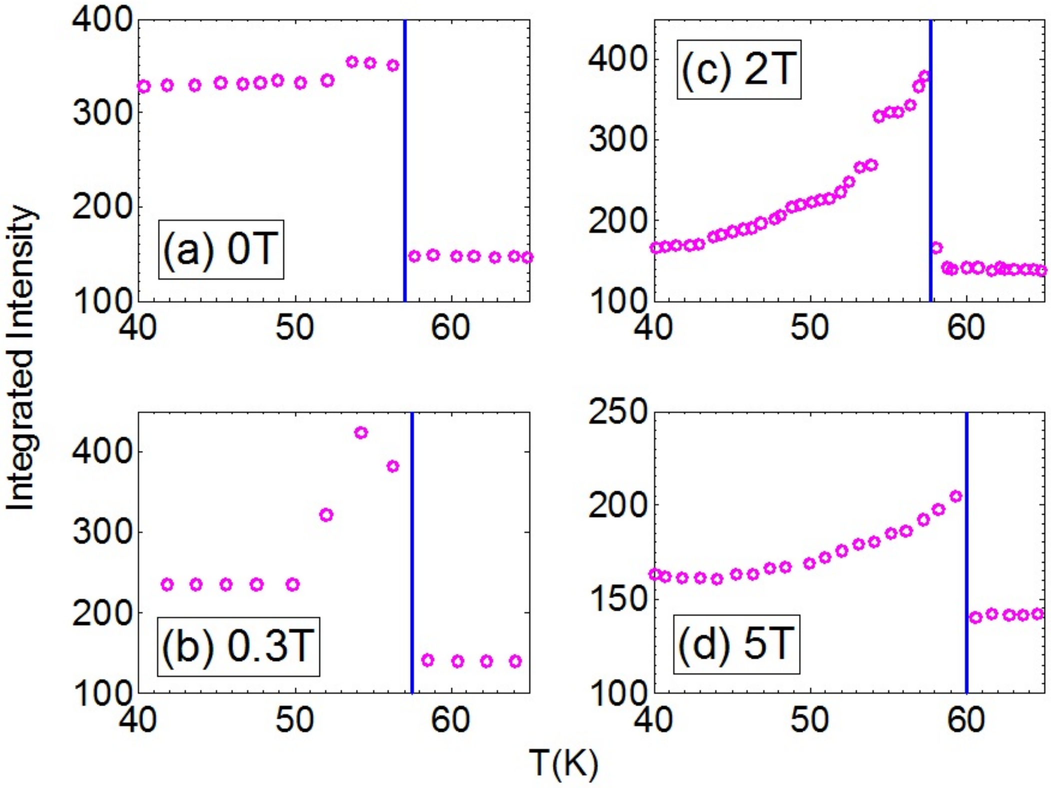

Figure 4.19: D15 measurements showing the integrated intensity of the (400) peak at various fields (a) B = 0T (b) B = 0.3T (c) B = 2T (d) B = 5T with temperature cooling. The transition temperatures can be clearly seen and are marked by blue lines. An intermediate phase can also be clearly seen in the 0.3T data (b), but this phase is less well defined at higher fields.

A model was used in which the manganese and vanadium moments are fixed at the values found using D10 (Table 4.2) and the scale factor and extinction factor were deduced. The Cambridge Crystallographic Subroutine Library can be used to model the extinction but the sample dimensions need to be known. A good fit to the data was obtained but with a large extinction factor.

4.3.5 Phase diagram

The following phase diagram (Figure 4.20) was produced using SQUID, neutron and X-ray diffraction and lattice striction measurements (taken from Adachi *et al.* [43]). All measurements shown are with temperature cooling.

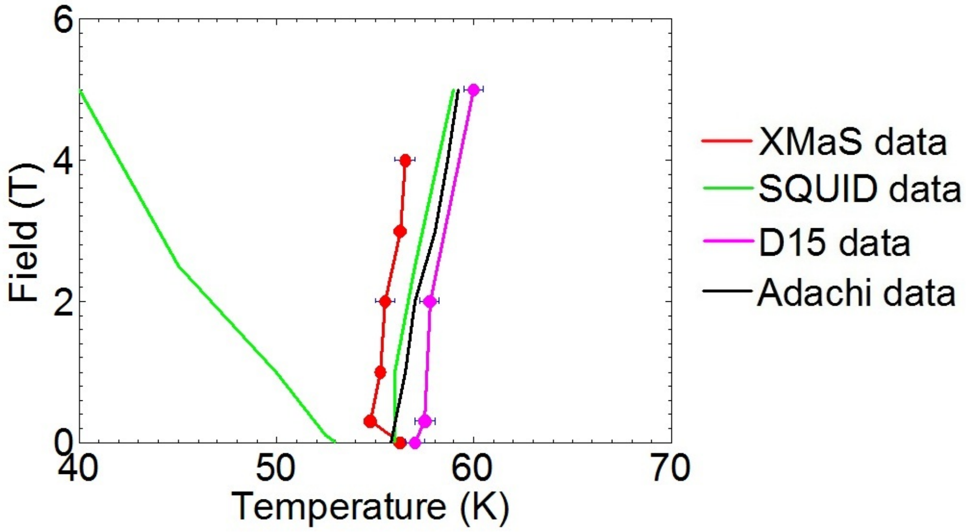

Figure 4.20: MnV_2O_4 phase diagram produced using SQUID (green line), neutron (pink line) and X-ray diffraction (red line) and lattice striction measurements (black line) with cooling temperature.

It is clear from the measured structural transition temperature and the slope of the phase boundary that the transition from cubic to tetragonal occurs at the Néel temperature, $T_N = 57$K. This is in contrast to the result stated, but not explicitly shown by Plumier *et al.* [37], and restated by most subsequent authors [38, 42–45], that the structural distortion occurs at $T_M = 53$K. Our result agrees with single crystal synchrotron X-ray study of the structural transition by Suzuki *et al.* [75].

4.4 Discussion

The structure deduced from our single crystal measurements agrees with that predicted by Garlea *et al.* [42]. Measurements on D10 are affected by extinction. Extinction occurs if the diffracted beam is at the correct angle for a second diffraction to take place. This internal scattering in the crystal causes the exiting beam to miss the detector. At a strong Bragg point there is a higher probability of the beam diffracting again which decreases the relative intensity of the strong reflections.

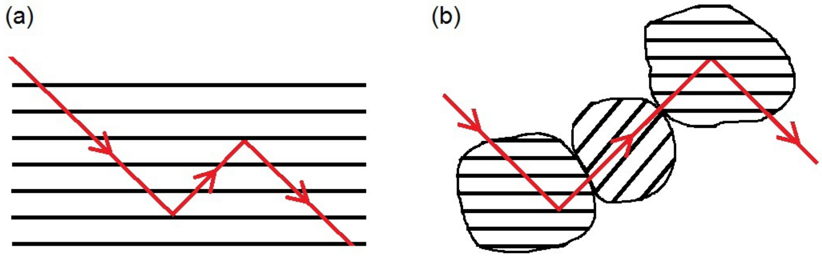

Figure 4.21: (a) Primary extinction caused by multiple reflections from different atomic planes in a perfect crystal and (b) Secondary extinction caused by multiple reflections from a crystal with domains. Both situations result in a loss of intensity but the effect is worse for a single domain crystal.

In the D15 experiment the use of a magnetic field enabled us to obtain measurements in a single structural and magnetic domain (see Figure 4.18), but since the sample was mounted in a cryostat, we had access to fewer reflections than on D10. These single phase measurements also agree with Garlea *et al.* [42].

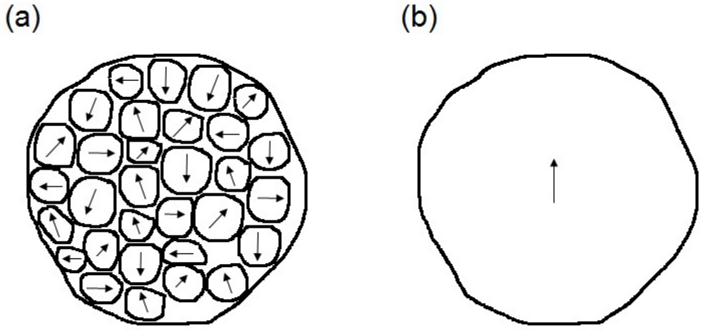

Figure 4.22: (a) Domains present on D10 (b) Use of a field on D15 produced a single structural and magnetic domain but this leads to more extinction. The formation of a single domain also leads to a higher extinction factor.

The formation of a single domain also leads to a higher extinction factor. This means that the single domain approach does not add much, but it is the best that we can do. Our results clearly show that the structural transition from cubic to tetragonal occurs at the Néel temperature.

5 MnV_2O_4 excitations

5.1 Background

5.1.1 Magnetic excitations from MnV_2O_4

The magnetic excitations of MnV_2O_4 were measured using single-crystal neutron scattering at NIST by Chung *et al.* [79]. Figure 5.1 shows the magnetic intensity along the [4-l, 0, l] and [2, 0, l] directions, in the cubic setting, in the non-collinear phase at T = 5K. The dispersion relations shown in this figure were calculated from the excitations from the non-collinear ground state proposed by Plumier *et al.* [36, 37]. There is certainly good qualitative agreement with the data. There are two energy bands. The lower band is mostly due to magnetic fluctuations of Mn^{2+} and the upper band is mostly due to the fluctuations of the V^{3+} ions. The problem with this interpretation of the results is that the magnetic ground state proposed by Garlea *et al.* [42] using powder neutron diffraction, and confirmed by us in the previous chapter using single-crystal neutron diffraction, is different to that proposed by Plumier *et al.* [36,37]. Thus the calculated excitations in Chung *et al.* [79] are from the wrong magnetic ground state. In this chapter we have re-examined the magnetic excitations from MnV_2O_4 in the light of new, more accurate inelastic neutron scattering data. First, we have obtained a much more comprehensive data set in zero field using unpolarised neutrons, sampling a much larger region of reciprocal space, using the MAPS spectrometer at ISIS. Secondly, we have focussed on selected regions of the dispersion using polarised inelastic neutron scattering studies from a single domain using the IN20 spectrometer at the ILL.

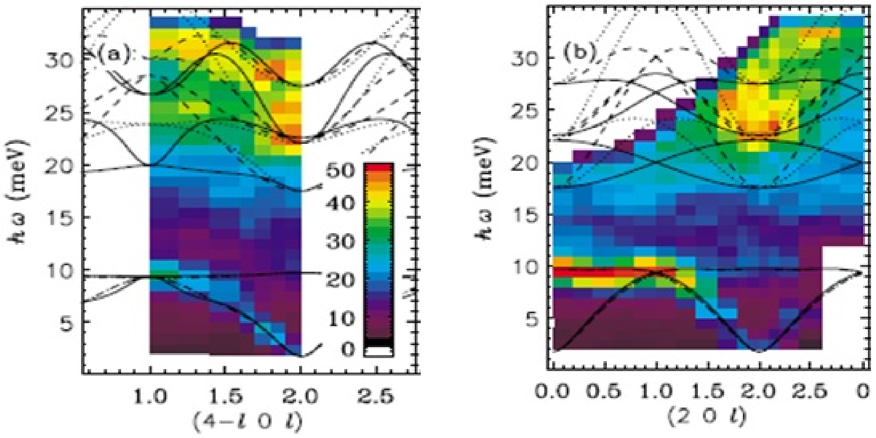

Figure 5.1: Inelastic neutron scattering intensity from the non-collinear phase of MnV_2O_4 at T = 5K by Chung *et al.* [79]. The magnetic excitations are calculated from the non-collinear ground state proposed by Plumier *et al.* [36,37]. In (a) [(b)], the dotted, dashed and solid lines correspond to dispersions calculated along (0kl), (h0l) and (hk0) [(h00), (0k0) and (00l)] directions respectively, which are superimposed due to the pseudocubic symmetry.

5.2 Experimental procedure

Sample preparation

A large 6g single crystal was produced by Le Duc Tung at the University of Warwick which was six times larger than the crystal used by Chung *et al.* [79].

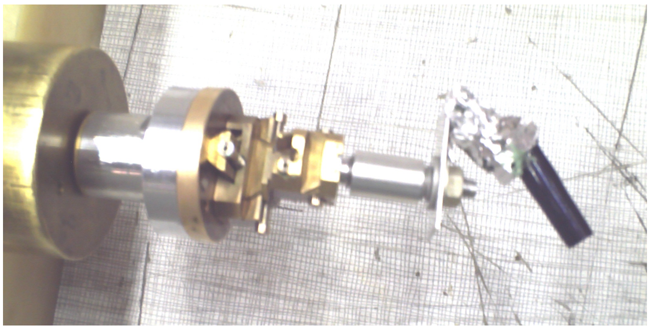

Figure 5.2: Photograph showing MnV_2O_4 6g sample mounted on cryostat sample stick.

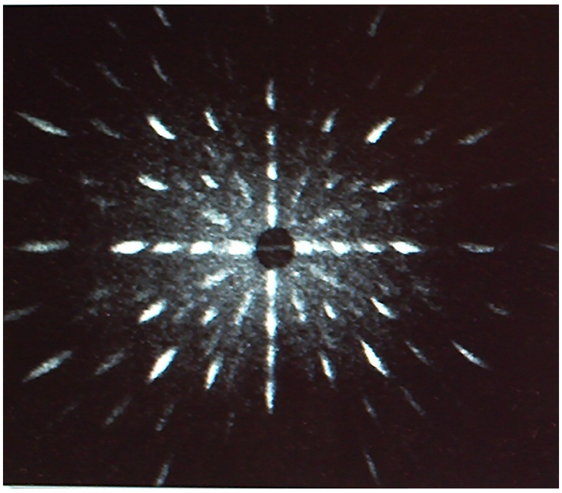

Figure 5.3: MnV_2O_4 Laue diffraction pattern, showing a 4-fold axis, produced on Orient Express at the ILL with the help of Bachir Ouladdiaf.

MAPS experiment

A single-crystal inelastic unpolarised neutron scattering experiment was carried out on MAPS at ISIS with Christopher Frost. The crystal was mounted with the (110) crystallographic plane horizontal. Four-dimensional data sets were produced in the low temperature, non-collinear phase at T = 5K. No field was applied and, therefore, the sample was multi-domain. These results can be compared directly with those of Chung *et al.* [79]. Data sets were obtained with incident energies E_i = 30meV, to focus on the lower energy excitations with high resolution, and E_i = 60meV to probe the highest energy regions of the dispersion. The sample was rotated about its vertical axis by one degree over a total range of 45 to 135° at E_i = 30meV and from 45 to 69° at E_i = 60meV, scanning one degree in 66 minutes.

IN20 experiment

The experiment on IN20 at the ILL was carried out with Mechthild Enderle. The sample was mounted in a vertical cryomagnet with the [001] direction vertical. As has been verified on D15, MnV_2O_4 adopts a single magnetic and structural domain at an applied field of $\mathbf{B}$ = 2T, see Section 4.3.4. These measurements of single-domain MnV_2O_4 were performed at a temperature of T = 2K and a field along the [001] direction of $\mathbf{B}$ = 2T. Unidirectional polarisation analysis was achieved using Heusler (111) monochromator and analyser crystals. The final energy was fixed at E_f = 14.8meV, and the incident energy was scanned with $\mathbf{Q}$ fixed along the [2+h, -2+h, 0], [h, 0, 0], [2, k, 0], [2+h, -h, 0] and [2.5-h/4, h, 0] directions. The first four were accessible high symmetry directions and the last was a more general scan.

5.3 Results

5.3.1 MAPS results

The data was analysed using HORACE (a computer program for the visualisation and analysis of datasets from TOF neutron inelastic scattering spectrometers) [67] with assistance from Russell Ewings of ISIS. Figures 5.4 and 5.5 show cuts through reciprocal space with an incident energy of E_i = 30meV. Figure 5.4 shows constant energy slices integrated over a narrow range of energy transfer as a function of **Q** in the (hk0) plane, with **Q** along the [00l] direction integrated over l = -0.2 to 0.2. Cones of scattering are seen to come from the (2, -2, 0) and (4, 0, 0) positions, and these are found to disperse by about 10meV. This enables a robust, qualitative conclusion to be drawn. The antiferro-orbital model of Tsunetsugu *et al.* [33] results in negligible interchain coupling (J' << J) and this would lead to perpendicular stripes of scattering in this plane from the perpendicular chains. The 3D excitations observed have ruled out this model. Thus, even the qualitative features of these data show directly that the interchain coupling is not negligible compared to the intrachain coupling.

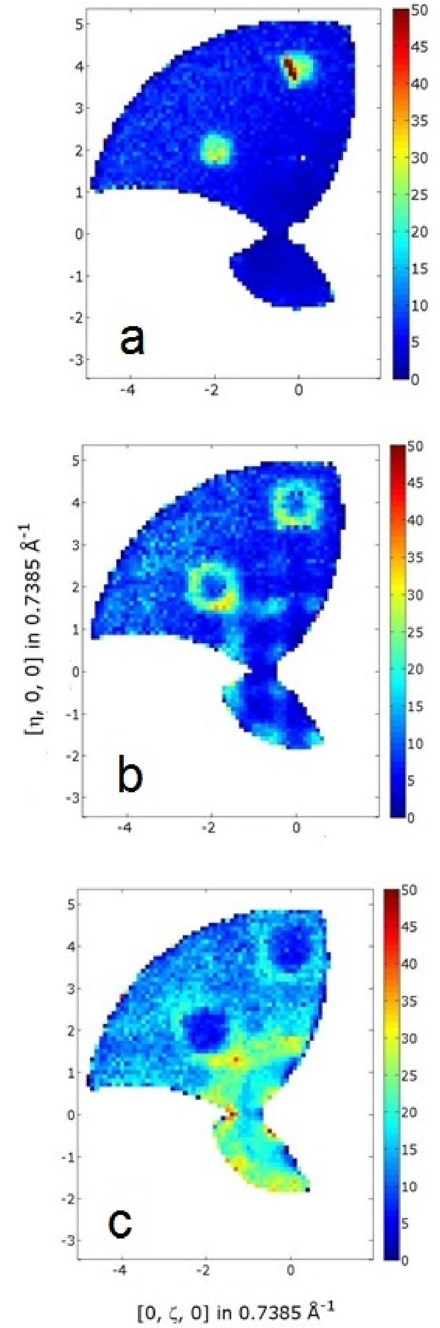

Figure 5.4: Magnetic excitations from MnV_2O_4 at T= 5K observed on MAPS with an incident energy $E_i = 30$meV. The cuts show data in the (HK0) plane integrated over the following energy transfer ranges: (a) 2-5meV (b) 5-7meV (c) 7-9meV

Selected spin wave dispersions are shown in Figure 5.5, where the data are plotted as a function of **Q** in one direction, energy in the other and an integration over a **Q** range -0.2 to 0.2 is performed over the perpendicular directions in **Q**. The data for $\mathbf{Q} = [\xi, -\xi, 0]$ in Figure 5.5(a) can be directly compared with the data of Chung *et al.* [79] along [4-l, 0, l] in Figure 5.1(a). The two data sets are found to be entirely consistent. The dispersion along $\mathbf{Q} = [\zeta, 0, 0]$ in Figure 5.5(b) can be compared with Chung *et al.* for $\mathbf{Q} = [2, 0, l]$ in Figure 5.1(b). In this case, the greater sensitivity of the MAPS data indicates an additional feature at $\mathbf{Q} =$ (200) that is not clear from the earlier data set. Figure 5.5(c) is an example of data in a new region of reciprocal space along $\mathbf{Q} = [\zeta, \zeta, \zeta]$.

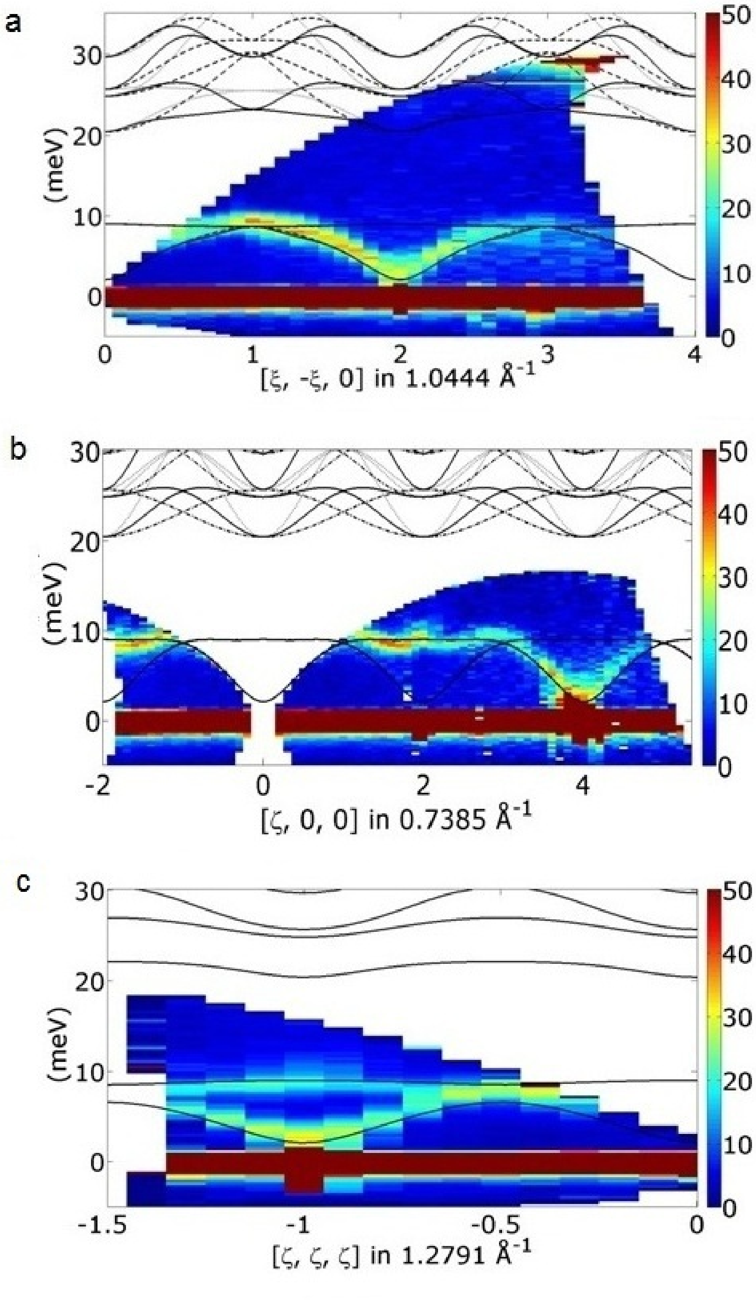

Figure 5.5: Magnetic excitations from MnV_2O_4 at T = 5K observed on MAPS with an incident energy E_i = 30meV. Data along (a) $(\xi, -\xi, 0)$(b) $(\zeta, 0, 0)$ and (c) (ζ, ζ, ζ). A crossing in the dispersion can be seen in (b) at the (200) position which is not seen in the calculation.

Figure 5.6 shows data obtained on MAPS with an incident energy of E_i = 60meV. The aim in this case was to probe the higher energy excitations.

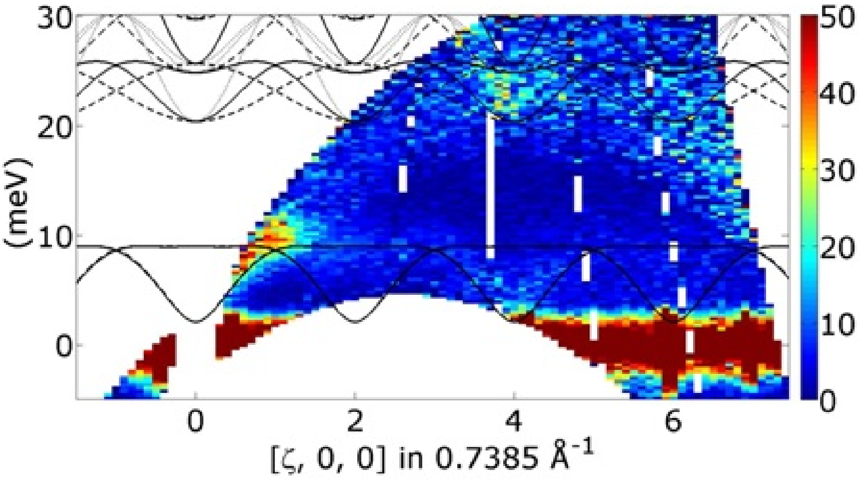

Figure 5.6: Magnetic excitations from MnV_2O_4 at T = 5K observed on MAPS with an incident energy E_i = 60meV.
Some scattering can be seen at high energy but it is not well defined.

The very broad feature above 20meV at **Q** = (400) is consistent with the data in Figure 5.1(b) by Chung *et al.* [79]. In the latter case the intensity at high energy transfer has been emphasised by multiplying by frequency. However, we note that in both cases it may prove difficult to resolve features of the models clearly using the rather washed out features at high energy.

5.3.2 IN20 results

Figure 5.7 shows the polarised inelastic neutron scattering for **Q** = (2+h, -2+h, 0) from a single domain of MnV_2O_4 in the non-collinear phase at a temperature T = 2K and a field **B** = 2T applied along the [00l] direction. Figure 5.7(a) shows the data in the spin-flip channel and Figure 5.7(b) shows the corresponding data in the non-spin-flip channel. The fact that the scattering is much stronger in the spin-flip channel directly confirms the magnetic origin of these excitations. These data can be directly compared with the MAPS data in Figure 5.5(a) and the NIST data of Chung *et al.* in Figure 5.1(a). It is clear that the signal-to-background is much better in the spin-flip channel on IN20 as expected.

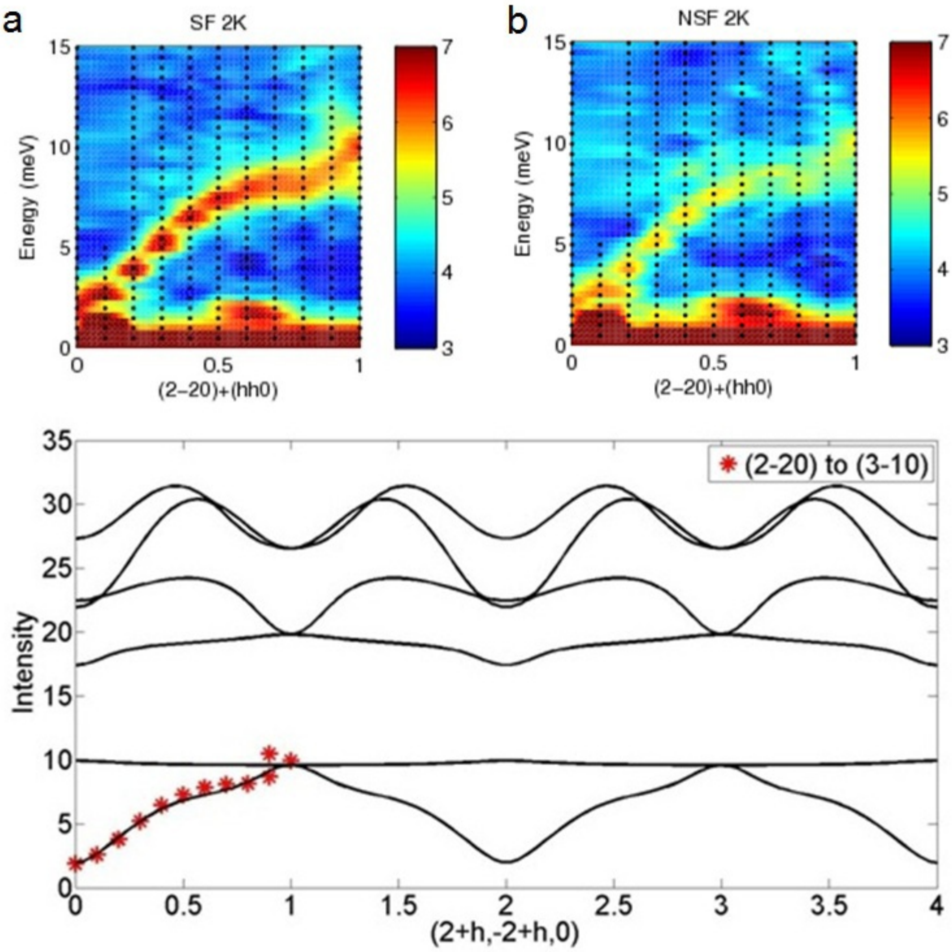

Figure 5.7: IN20 MnV_2O_4 data along (2+h, -2+h, 0). a) Data in the spin-flip channel. b) Data in the non-spin-flip channel. The calculation fits the observed dispersion fairly well.

Figure 5.8 shows the data in the spin-flip channel for **Q** = (h00). The feature first revealed at **Q** = (2,0,0) and Δ E = 10meV on MAPS, see Figure 5.5(b), is shown to be a crossing point. This qualitatively new feature was missed during the NIST experiment due to the lower signal-to-background. In fact, a closer inspection of Figure 5.7 reveals a similar, but weaker, feature near **Q** = (3,-1,0) and Δ E = 10meV. Figures 5.9, 5.10 and 5.11 show the spin-flip scattering for **Q** = (2, h, 0), (2+h, -h, 0) and (2.5 - h, 4 , -h, 0) respectively. The crossing point is particularly clear for Figure 5.10.

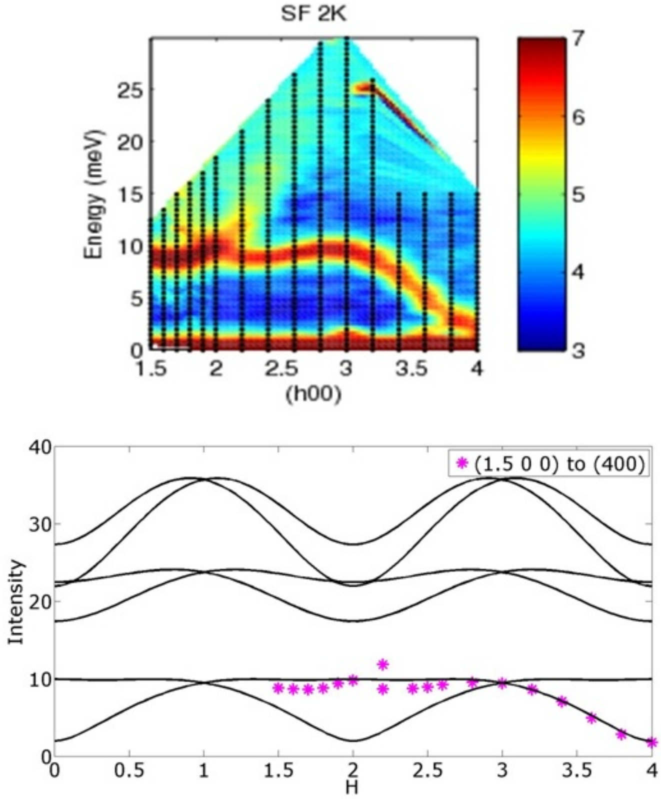

Figure 5.8: IN20 MnV_2O_4 data along (H00). A dipping and crossing in the dispersion can be seen at (200) which is not accounted for in the calculation.

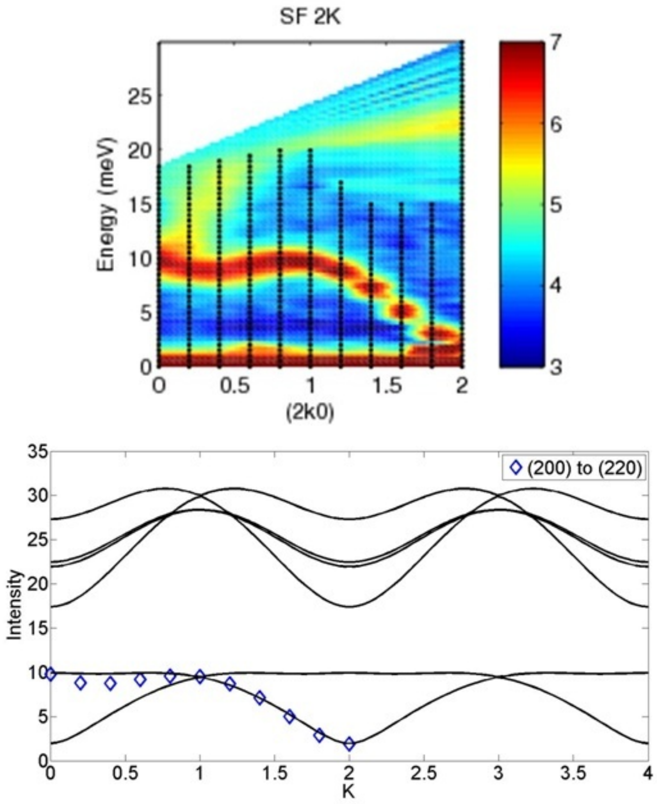

Figure 5.9: IN20 MnV_2O_4 data along (2K0). A dipping and crossing in the dispersion can be seen at (200) which is not observed in the calculation.

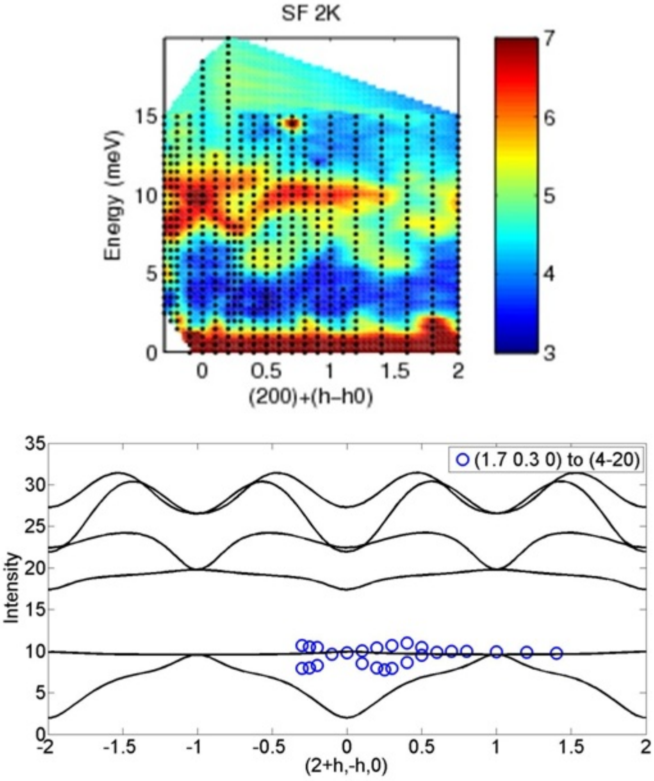

Figure 5.10: IN20 MnV_2O_4 data along (2+h, -h,0). A complex crossing is seen in the dispersion at (200) which is not accounted for in the calculation.

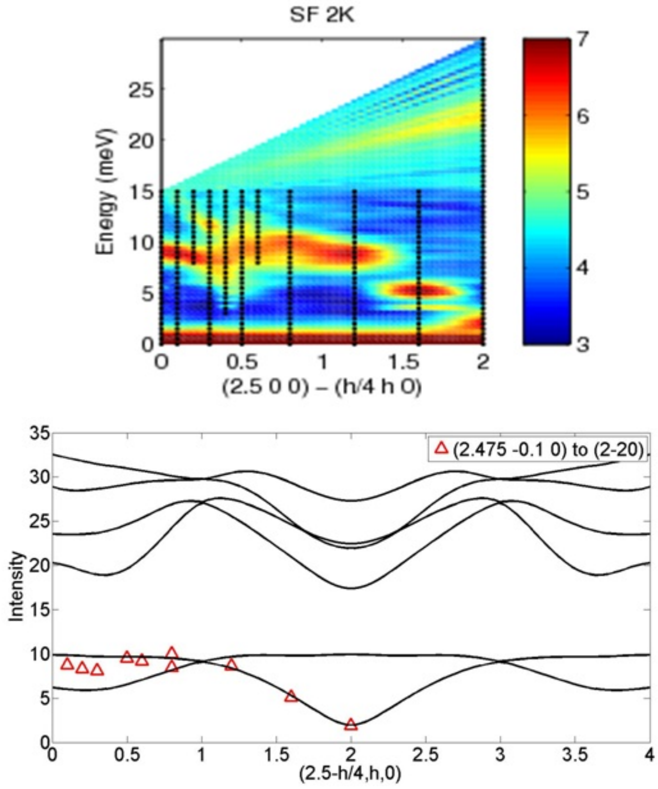

Figure 5.11: IN20 MnV_2O_4 off-symmetry data. This data can also be seen to depart from the calculation.

5.4 Magnetic model calculations

Spin wave dispersion

In order to compare our data with that of Chung *et al.* [79] we needed to reproduce Chung's magnetic model calculation. This was done by Peter Conlon (University of Oxford), he produced a Matlab program in which the spin wave dispersions could be calculated for any choice of model parameters and for any cut in reciprocal space [80]. The following is a brief overview of the steps he used to reproduce the spin wave dispersion calculation.

Firstly the lattice positions of the atoms in the tetragonal phase were determined and it was assumed for simplicity that this did not change. As described in Section 4.1.1, MnV_2O_4 has a spinel structure, the general formula of which is AB_2O_4. The A sites form a diamond lattice and have 12 B neighbours which form a pyrochlore lattice. The A sites can be thought of as being at the centre of a tetrahedron interacting with three spins on the face of each tetrahedron [80].

The next step was to define the spin Hamiltonian. J_{ij} are the Heisenberg exchange constants. The simplest Hamiltonian to give reasonable fits to the data include the nearest neighbour exchange interactions between A and B ions J_{AB}, the interactions between B ions J_{BB} and $J_{BB'}$ and single ion anisotropies for both ions (defined as D_i^d, where d is the axis of the anisotropy) [79].

$$\mathcal{H} = \frac{1}{2}\sum_{i \neq j} J_{ij}\mathbf{S}_i \cdot \mathbf{S}_j + \sum_{i,d} D_i^d (S_i^d)^2 \tag{5.1}$$

AB bonds were given an energy of $J_{AB}\mathbf{S}_A \cdot \mathbf{S}_B$, BB and BB' bonds have an energy of $J_{BB}\mathbf{S}_B \cdot \mathbf{S}_B$ and $J_{BB'}\mathbf{S}_B \cdot \mathbf{S}'_B$. The spin quantum numbers are $\mathbf{S}_A = \frac{5}{2}$ for Mn^{2+} and $\mathbf{S}_B = 1$ for V^{3+} [79, 80]. It was assumed that, classically, the MnV$_2$O$_4$ spin structure could be parameterised by one angle, θ_{YK} with a structure $\mathbf{S}_A = S_A$(0,0,-1) for both A sites [80]. The B sites can be defined as $\mathbf{S}_B^{1,2} = S_B(0, sin\theta_{YK}, cos\theta_{YK})$ and $\mathbf{S}_B^{3,4} = S_B(0, -sin\theta_{YK}, cos\theta_{YK})$. The total energy per unit cell was calculated and then differentiated with respect to θ to obtain a stationary point which is a minimum of the classical energy [80].

A quadratic Hamiltonian was then deduced using Holstein-Primakoff Bosons [80]. To do this it was assumed that each primitive cell is identical. The spinel has two A sites and four B sites in a primitive cell. The Holstein-Primakoff boson operators are defined relative to a quantisation axis and expresses the quantum fluctuation of a spin away from its classical direction. The operators are then converted to cartesian coordinates. [80]. Considering the products of spins (separated by the angle ϕ) gives:

$$J_{12}\mathbf{S}_1 \cdot \mathbf{S}_j \approx J_{12}S_1S_j\frac{1}{4\sqrt{S_1S_2}}(\mathbf{b}^{\dagger}\mathbf{b})Q(\phi_{12})\begin{pmatrix}\mathbf{b}\\ \mathbf{b}^{\dagger}\end{pmatrix} \qquad for\ \mathbf{b} = (b_1b_2) \tag{5.2}$$

To calculate the spin wave spectrum, the quadratic part of all bonds is retained and a Fourier transform is applied to arrive at a 12 × 12 matrix M($\mathbf{q}$). This is a quadratic form for bosons at wavevector $\mathbf{q}$ [80].

The quadratic Hamiltonian is 'Bogoliubov-diagonalised' via canonical variables [80]. The basis transformation from bosons to canonical x = (p, q) is:

$$\begin{pmatrix} \mathbf{b} \\ \mathbf{b}^\dagger \end{pmatrix} = \frac{1}{\sqrt{2}} \begin{pmatrix} i & 1 \\ -i & 1 \end{pmatrix} \begin{pmatrix} p \\ q \end{pmatrix} \tag{5.3}$$

The Hamiltonian was then expressed as a quadratic form for canonical variables in the form $\mathcal{H} = \frac{1}{2}x^T A x$ where

$$A = 2\frac{1}{2} \begin{pmatrix} -i & i \\ 1 & 1 \end{pmatrix} M \begin{pmatrix} i & 1 \\ -i & 1 \end{pmatrix} \tag{5.4}$$

The spectrum of the quadratic spin wave Hamiltonian are the eigenvalues of IA [80] where

$$I = \begin{pmatrix} 0 & -E \\ E & 0 \end{pmatrix} \tag{5.5}$$

and E is the identity matrix. This is then possible to calculate on a computer [80].

It is possible to reproduce Chung's dispersion using the same exchange and anisotropy parameters listed in Table 5.1, but only when the spin of the Mn (S_A)

is set to the incorrect value of 1 instead of $\frac{5}{2}$.

S_B	S_A	J_{AB}	J_{BB}	$J_{BB'}$	D^z_A	D^y_B	D^z_B
1	1	2.8(2)	9.8(9)	3.0(8)	-0.6(4)	-4.0(4)	2.7(9)

Table 5.1: Exchange parameters of MnV_2O_4 used by Chung to create spin wave dispersions [79]. Nearest neighbour exchange interaction between A and B ions = J_{AB}. The exchange along orbital chains = J_{BB}. The exchange between orbital chains = $J_{BB'}$. The values of D^d_i are the single ion anisotropies where d is the axis of the anisotropy.

In order to fit the data with the correct value, $S_A = \frac{5}{2}$, the exchange parameters had to be changed to those given in Table 5.2. The new values were determined via trial and error. Each parameter was varied through a range from -10 to +10 to see how it affected the calculation. Combinations of parameters were then varied to see if the fits could be improved. Because the spin of the Mn has been changed it makes sense that J_{AB} changes by more than J_{BB} and $J_{BB'}$. The single-ion anisotropies also change substantially.

S_B	S_A	J_{AB}	J_{BB}	$J_{BB'}$	D^z_A	D^y_B	D^z_B
1	5/2	4.3	10.0	3.0	-1.0	-6.0	0.5

Table 5.2: Exchange parameters of MnV_2O_4 as deduced via trial and error. Nearest neighbour exchange interaction between A and B ions = J_{AB}. The exchange along orbital chains = J_{BB}. The exchange between orbital chains = $J_{BB'}$. The values of D^d_i are the single ion anisotropies where d is the axis of the anisotropy.

In the previous figures, showing data from MAPS at ISIS, the calculated dispersion fits the data along Q $=[\xi, -\xi, 0]$ very well (Figure 5.5 (a)). However, the data along $[\xi, 0, 0]$ (Figure 5.5 (b)) does not correspond to the dispersion calculated in this model. A closer examination of Chung's data in Figure 5.1 (b) is consistent with this conclusion. Furthermore, there appear to be crossing points at, for example, the (200) position (Figure 5.5 (b)) that are completely inconsistent with the model. When we look in regions of reciprocal space further away from the Chung data, the extrapolation of the model does not work fully. For example, the splitting of the modes in the calculation at $(\frac{1}{2}\frac{1}{2}\frac{1}{2})$ is not found in the data (see Figure 5.5 (c)). The comparison with the higher energy modes is also problematic. In common with Chung *et al.*, we do not clearly resolve the high energy magnetic excitations. The scan performed with an incident energy of 60meV (Figure 5.6) shows some scattering at high energy but like the Chung data (Figure 5.1) it is rather washed out so it is difficult to compare with the calculations. Therefore, we investigated the excitations in particular regions of reciprocal space with greater sensitivity by using polarised neutrons on IN20 at the ILL. The measurements were performed with a magnetic field along the c-direction in order to select a single magnetic domain. The figures showing spin flip scattering data from IN20 at the ILL (Figures 5.7 to 5.11) have better experimental resolution than Chung *et al.* These results show that Chung *et al.* does not correctly model the excitations from MnV_2O_4 in the low temperature phase.

5.5 McPhase calculations

The program McPhase was designed to calculate the static and dynamic magnetic properties of a system given the crystal field and exchange parameters. Anisotropic and higher order terms such as quadrupolar interactions can be taken into account [81]. It has several independent modules. The module '*cfield* ' is used to calculate the crystal field transitions. The module '*mcphas*' deals with the pair interactions, it calculates the thermodynamic properties and the free energy by running a combined mean-field/Monte-Carlo algorithm. The most stable magnetic structure at a given field and temperature is deduced using randomly chosen initial moment configurations. Calculations at several temperatures and magnetic fields can be run in order to map a magnetic phase diagram [81]. The module '*msdisp*' uses a mean-field random phase approximation to calculate the dispersion and intensity of magnetic excitations and diffuse magnetic scattering cross section [82]. McPhase uses the following Hamiltonian:

$$\mathcal{H} = \sum_i \left[B_l^m O_l^m(\mathbf{J}_i) - g_{J_i}\mu_B \mathbf{J}_i \mathbf{H} - \frac{1}{2}\sum_j \mathcal{J}(ij)\mathbf{J}_i\mathbf{J}_j \right] \tag{5.6}$$

where the first term describes the crystal field using Stevens operators O_l^m, the strength of the crystal field is given by the crystal field parameters B_l^m. (l = angular quantum number, m = magnetic quantum number). The second term is the Zeeman energy if a magnetic field is applied. The third term is the bilinear magnetic interaction [81].

Manh le Duc, from HZB in Berlin attempted to model the magnetism of MnV_2O_4 using McPhase (with assistance from Martin Rotter, University of Oxford). He used orbital angular momentum and spin angular momentum values as follows: $S = \frac{5}{2}$ and $L = 0$ for Mn^{2+} and $S = 1$, $L = 3$ for V^{3+}, with parameters determined using Peter Conlon's Matlab program (Table 5.2). The crystal field was calculated using a point charge model rather than the anisotropy parameters. The crystal field has no effect in the case of Mn^{2+} because it only operates on the orbital part of the electronic wavefunctions and L=0 for the ground state of Mn^{2+} [83]. V^{3+} has a slight trigonal distortion [45], this was calculated by reducing the space group symmetry of MnV_2O_4 from $Fd\bar{3}m$ to R3m. The O^{-2} position is (x,x,x) in $Fd\bar{3}m$ but is (x,x,z) in R3m. The trigonal distortion was calculated by reducing z by 0.02rlu (reciprocal lattice units), this displaced the oxygen atoms by about 0.15Å. However, this lowering of the space group does not affect the positions of the Mn^{2+} and V^{3+} ions and so, as the oxygen ions are not included in the mean field calculations, the cubic $Fd\bar{3}m$ space group was used for the calculations [83]. The crystal field parameters B_l^m obtained from running McPhase are shown in Table 5.3.

${B_2}^0$	${B_4}^0$	${B_4}^3$
7.19483 meV	1.16733 meV	37.8707 meV

Table 5.3: McPhase crystal field parameters

These parameters give a doublet ground state ($|$S $=$ 1, L $=$ 3, m$_L$ $=$ 0, m$_S$ $=$ $\pm$1 $\rangle$), and excited singlet at 1.4meV, ($|$S $=$ 1, L $=$ 3, m$_L$ $=$ 0, m$_S$ $=$ 0$\rangle$) and an excited doublet at 8meV ($|$S $=$ 1, L $=$ 3, m$_L$ $=$ 2, m$_S$ $=$ $\pm$1$\rangle$), with other levels above 50meV.

The calculations by Manh le Duc using the McPhase program have been quite successful. Including the orbital interactions gives a magnetic structure similar to that of Garlea *et al.* [42] which agrees with our single crystal neutron diffraction data and there is a qualitative agreement with the experimental excitations. Figure 5.12 shows that it is possible to reproduce the observed crossing points.

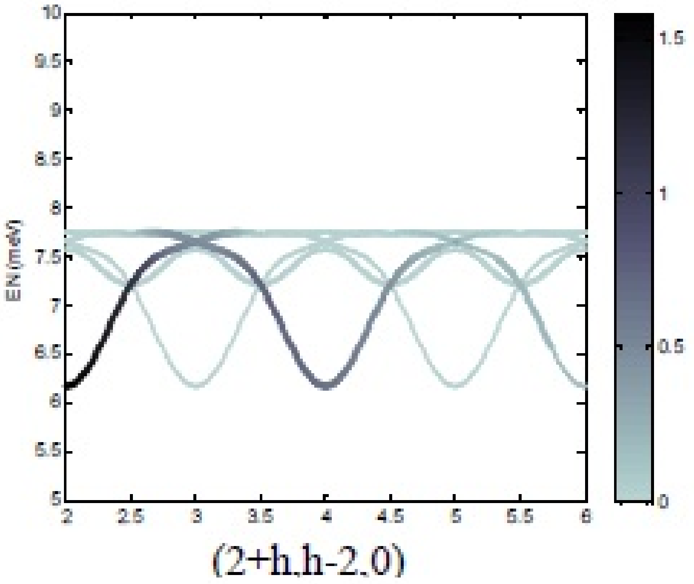

Figure 5.12: McPhase calculation of MnV_2O_4 excitations showing the crossing point which was not produced using the Chung model.

5.6 Discussion

The fact that the magnon dispersion has cones corresponding to a three dimensional system, rather than the streaks from a one dimensional system and the results support a non-negligible $J_{BB'}$, rules out the anti-ferro orbital ordering model suggested for AV_2O_4 compounds by Tsunetsugu and Motome [33]. The ferro-orbital model of Tchernyshyov *et al.* [38] is already excluded by the space group $I4_1/a$ determined by Suzuki *et al.* [75]. Thus the orbital order proposed by Sarkar *et al.* [41] is the only remaining candidate. It has the correct space group and it agrees with the magnetic structure measured in Chapter 5 and calculated using McPhase. Furthermore, in this model all of the orbitals are partially occupied so it readily explains why the excitations should be three dimensional. Sarkar *et al.* [41] predict an interchain to intrachain ratio of J'/J $\approx$ 0.2, and this agrees qualitatively with our estimate of J'/J $\approx$ 0.3.

In the light of Garlea's proposed magnetic structure [42], and our new evidence in support of this structure, it is now clear that the Chung model [79] uses the wrong ground state. Our inelastic neutron scattering studies show empirically that this model is wrong. Attempts to model the excitations using the correct ground state are already promising. The model of Chung gives manganese modes at low energy and vanadium modes at high energy transfer. The crossing points in our data seem to suggest that the vanadium modes extend to lower energy transfer. The calculations using McPhase seem to imply that the rather simple dispersion measured experimentally is just the mode with the strongest intensity and, in fact, the full dispersion is rather more complicated. The approach of using a ‘black box’ programme such as McPhase is, therefore, a very suitable starting point for understanding a system with so many magnetic atoms in its unit cell.

6 GdVO$_3$

6.1 Background

6.1.1 Crystal structure of GdVO$_3$

The RVO$_3$ compounds have an orthorhombic perovskite structure at room temperature (Figure 6.1) [84]. The Vanadium ions are situated in the centre of corner sharing octahedra with the rare earth cation situated between the octahedra. The structure has the orthorhombic spacegroup (Pbnm) rather than a cubic spacegroup (Pm3m) because the octahedra are tilted in order to accommodate the large cations (This is known as GdFeO$_3$-type distortions) [85–87].

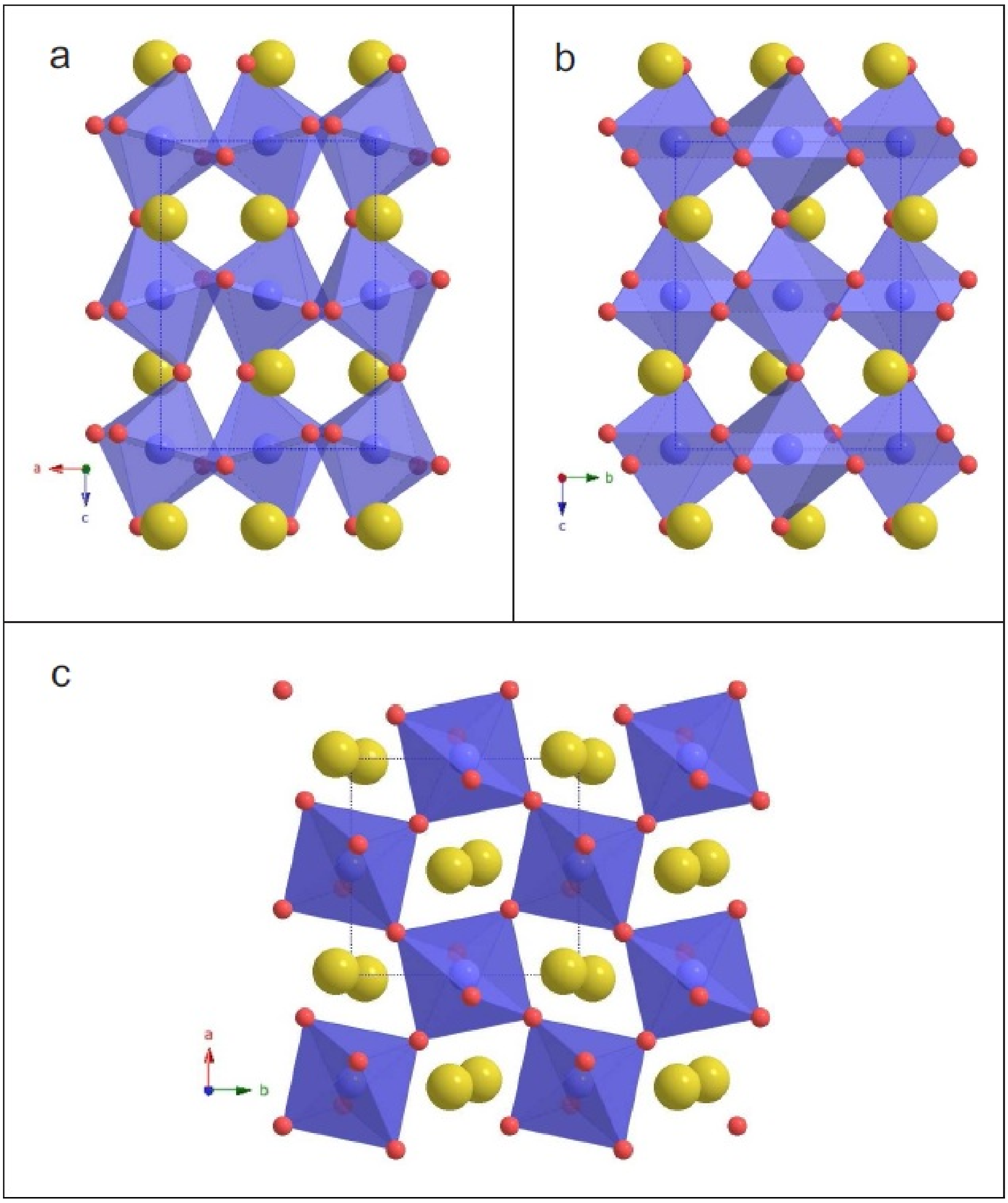

Figure 6.1: The crystal structure of GdVO$_3$ at room temperature with space group *Pbnm* after Skoulatos [53]. The Vanadium octahedra (blue) are surrounded by 6 corner-shared Oxygen ions (red) and Gadolinium (yellow). The ionic radii of V and Gd differ giving rise to GdFeO$_3$-type distortions.

6.1.2 Orbital ordering of $GdVO_3$

Cuprate superconductors and manganites with colossal magnetoresistance belong to the transition metal oxides (TMO) with the 3d e_g bands at the Fermi level. In these systems the Jahn Teller (JT) interaction is relatively strong and the orbital degeneracy is lifted well above the magnetic ordering temperature. The situation is different for the perovskite orthovanadates RVO_3 (R = rare earth or Y) with 3d t_{2g} bands at the Fermi level where the JT interaction is much weaker. As a result, the intrinsic frustration between spin and orbital degrees of freedom is believed to be crucial for understanding the interplay between ordering mechanisms [88–90].

In a crystal with TM ions the 5 fold degenerate d level is split into the 2 fold degenerate level (eg) and the 3 fold degenerate level (t_{2g}), see figure 1.1. There are two t_{2g} electrons in V^{3+}, and these adopt the high-spin configuration S=1 due to Hund's-rule coupling. One electron always occupies the d_{xy} orbital due to the orthorhombic distortion and the other electron occupies one of two possible states d_{yz} or d_{zx} [7, 91, 92]. As described in Section 1.1.2, an ion in a solid experiences a crystalline electric field, known as the 'crystal field', due to the charge on neighbouring ions. Because the d orbitals are not spherically symmetrical, the different orbitals behave in different ways in reaction to the form of the crystal field.

Jahn Teller effect

For many orbitally ordered transition metal systems the Jahn Teller (JT) effect is an important concept. The Jahn Teller effect was discovered in 1937 and has been extensively studied for the past 70 years. The theorem states that "any non-linear molecular system in a degenerate electronic state will be unstable and will undergo distortion to form a system of lower symmetry and lower energy thereby removing the degeneracy." [11].

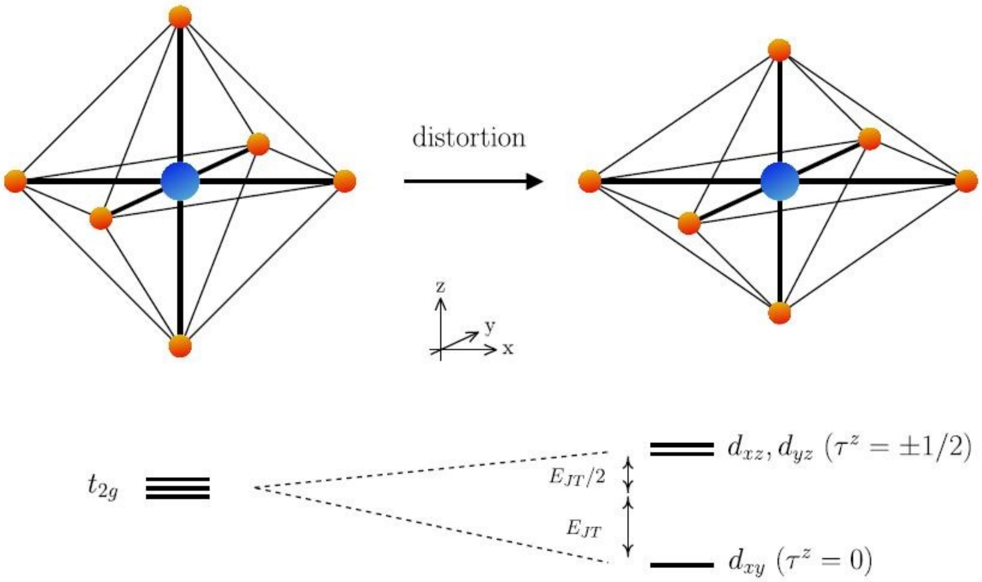

Figure 6.2: The Jahn Teller effect for a t_{2g} system. The distortion of the crystal lifts the degeneracy of the orbital energy levels. Figure from [53].

When this degeneracy is lifted, a 'vibron' (an electron-vibrational interaction), is emitted from the orbital-lattice coupling [92, 93]. This can be thought of as an interaction between the distorted lattice and the electrons of the degenerate level. When it is energetically favourable, the Jahn Teller effect can often cause distortion of the lattice which alters the orbital energy levels and lowers the symmetry of the crystal [94].

6.1.3 Magnetic structure of GdVO$_3$

The magnetic properties of RVO$_3$ compounds were studied in the 1970's [95–98] and were shown to display a variety of commensurate magnetic structures. A systematic investigation was carried out in 1976 by Zubkov, Bazuez and Shveikin using low-temperature, powder neutron diffraction [99]. Their study concluded that the beginning of the Vanadate series (Lanthanum to Dysprosium) showed C-type magnetic ordering of the Vanadate ions whereas the end of the series (Yttrium to Lutetium) had G-type magnetic ordering. These magnetic orderings are characterised by antiferromagnetic interactions on the ab plane with ferromagnetic interaction between planes for C-type and antiferromagnetic interaction between the planes for G-type [99]. Their investigations using X-ray diffraction showed that the C-type compounds also exhibited a structural phase transition around the Néel temperature, accompanied by a change in the degree of orthorhombic distortion [99]. At the time, Samarium, Gadolinium and Europium were not studied due to their strong absorption of neutrons at thermal wavelengths. Subsequent magnetisation measurements for GdVO$_3$ reveal intriguing magnetic properties including an unusual magnetic memory effect at the transition temperature T_M and a series of magnetic-field-induced phase transitions at low temperatures below T$_M$ [88].

The neutron measurements by Markos Skoulatos *et al.* reveal the onset of spin ordering at T$_{SO}$ in a C-type magnetic structure, with spins arranged ferromagnetically along the c direction and antiferromagnetically in the ab plane. G-type orbital ordering was observed below T$_{OO}$ using resonant X-ray scattering with alternating occupation of d$_{yz}$ and d$_{zx}$ orbitals in all three directions [53] in accordance with the Goodenough-Kanamori rules [100].

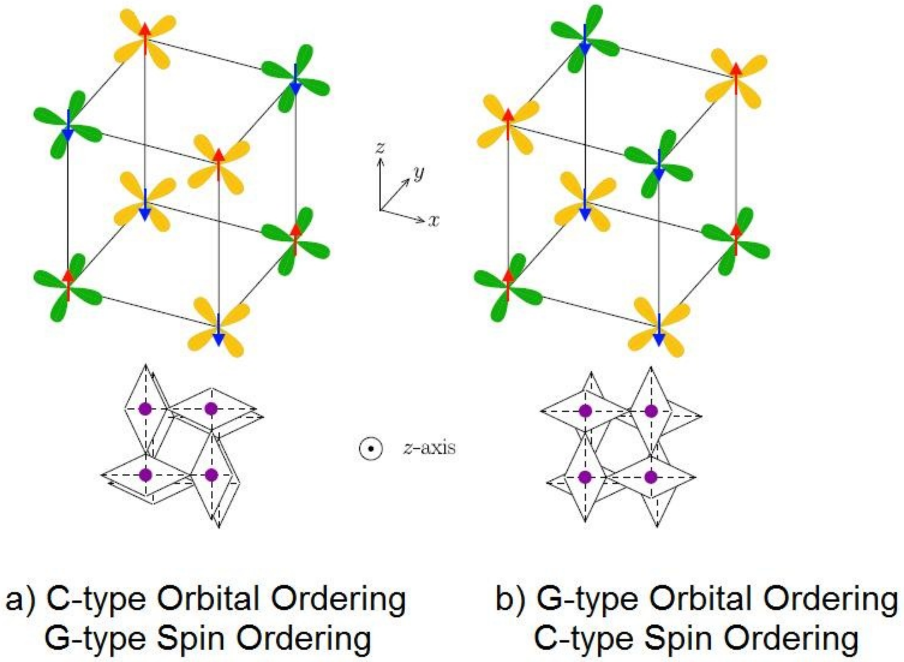

Figure 6.3: Structures of spin and orbital patterns often adopted by RVO$_3$ compounds. Jahn Teller distortions are in the ab plane. (a) V-O bond arrangements are in phase. (b) V-O bond arrangements are 90° out of phase. Orbitals in green are yz, orbitals in yellow are zx (the commonly occupied xy orbitals are not plotted). Vanadium sites are in purple, oxygen ion at corners of octahedra are not shown. Figure taken from Skoulatos [53].

6.1.4 Magnetisation reversal

Multiple temperature induced magnetisation reversals have been reported in YVO_3 [101] which has the same $GdFeO_3$ type distorted crystal structure as $GdVO_3$. Normally magnetic moment reversals are observed in ferrimagnets with strong magnetic anisotropy, however in YVO_3 all the magnetic V^{3+} sites are equivalent. The distortion of the crystal leads to canted spins and the antisymmetric Dzyaloshinsky-Moriya (DM) interaction is present because the oxygen ions mediating the superexchange between the V ions are not at an inversion centre [101]. A temperature-induced magnetization jump is also seen in $GdVO_3$, along the a axis (See Figure 6.4) [53], but whereas YVO_3 has only magnetic vanadium ions, $GdVO_3$ has both magnetic Vanadium, V^{3+}, and Gadolinium ions, Gd^{3+}. $GdVO_3$ also displays an unusual magnetic memory effect below $T_M \approx 8K$. Above T_M the material appears to be a homogeneous antiferromagnet, as it shows no remnant magnetization or coercivity, but the history dependent magnetism which is seen when heating the material through T_M suggests that there are domains present in the crystal [35].

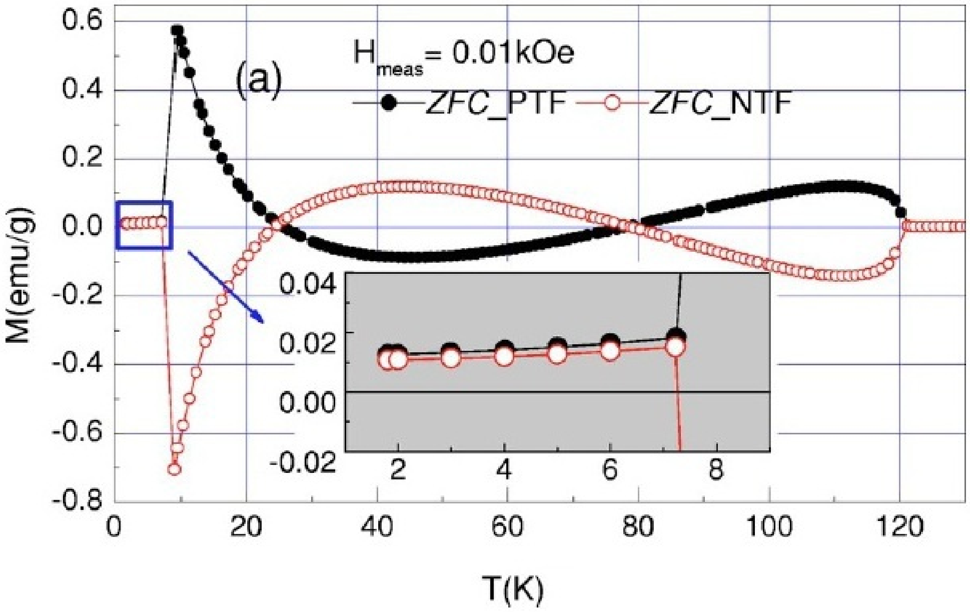

Figure 6.4: Effect of a trapped field on the ZFC magnetisation measured along the a axis of the GdVO$_3$ single crystal in applied field H$_{meas}$ of 10 Oe. After Tung [35].

Hubbard model

GdVO$_3$ is a Mott insulator and as such its properties can be explained by the Hubbard model. It does not exhibit normal metallic behaviour, where the electrons save kinetic energy by delocalising over the whole crystal, because in TMOs the Coulomb energy (the cost of putting an extra electron on a site) is very strong and cannot be overcome. As a result the electrons cannot move freely throughout the crystal, metallic behaviour ceases and electrons can no longer be treated as free particles, hence electron correlations become important. Such systems are therefore insulating [7,9]. The Hubbard model expresses the competition between the metallic behaviour and the Coulomb repulsion energy (U). If U is not infinite an antiferromagnetic structure is formed, as two electrons can occupy the same site providing that their spins are antiparallel. The internal degrees of freedom, spin and orbital, are still present in a Mott insulator unlike in a conventional band insulator. However, metallic behaviour can occur if the electronic band width, W, is larger than U. A metal-insulator transition occurs when U $\approx$ W [7, 9].

6.2 Experimental method

D9 Experiment

We studied single-crystal $GdVO_3$ on D9 at the ILL with the aid of local contact Garry McIntyre. Magnetic reflections in each of the four metamagnetic phases of $GdVO_3$ were measured from T= 2K to 10K. Having considered the magnetisation results shown in Figure 6.6, we applied the following magnetic fields along the vertical a axis: 15 kOe (between H1 and H2), 23 kOe (between H2 and H3), 28 kOe (between H3 and H4) and 40 kOe (above H4). Temperature dependencies of selected reflections were also measured. In addition to the interest in the magnetic memory effect below T_M [35], the results were required for ab-initio calculations of the resonant X-ray scattering at the Vanadium K edge from field-driven orbital transitions.

ID20 experiment

In order to unravel the anomalous magnetic properties of this compound [35], we performed magnetic X-ray scattering at the ESRF on instrument ID20 with Luigi Paolasini, Le Duc Tung and Martin Rotter. The single crystal $GdVO_3$ was aligned with the surface parallel to (011) and (100) directions and mounted in the $\mathbf{B}$ = 12T vertical field split coil cryomagnet with magnetic field applied along the (100) direction. This orientation of the crystal allows access to reflections close to or within the bc plane. The energy was set to the Gadolinium L_{II}-edge in order to measure the Gadolinium ordering. We performed k-scans at T = 2.4 K in different magnetic fields in both the $\pi\sigma$ and $\pi\pi$ channels.

6.3 Results

6.3.1 Bulk characterisation measurements

The following measurements were carried out by Le Duc Tung at The University of Warwick. The two transitions at T_{SO} and T_M observed in the heat capacity data (Figure 6.5) are again shown up in the magnetization data (Figure 6.7, a axis). There is no kink in the magnetisation data at T_{OO} and this is consistent with orbital ordering.

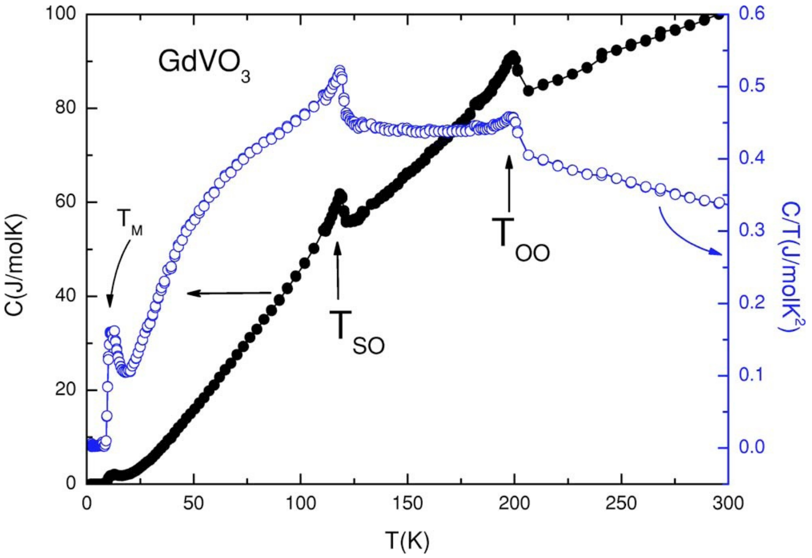

Figure 6.5: Heat capacity measurements for GdVO$_3$ reveal a phase transition at T_{OO}= 199 K, magnetic ordering at T_{SO} =118 K, and a further magnetic transition at T_M= 8 K [35].

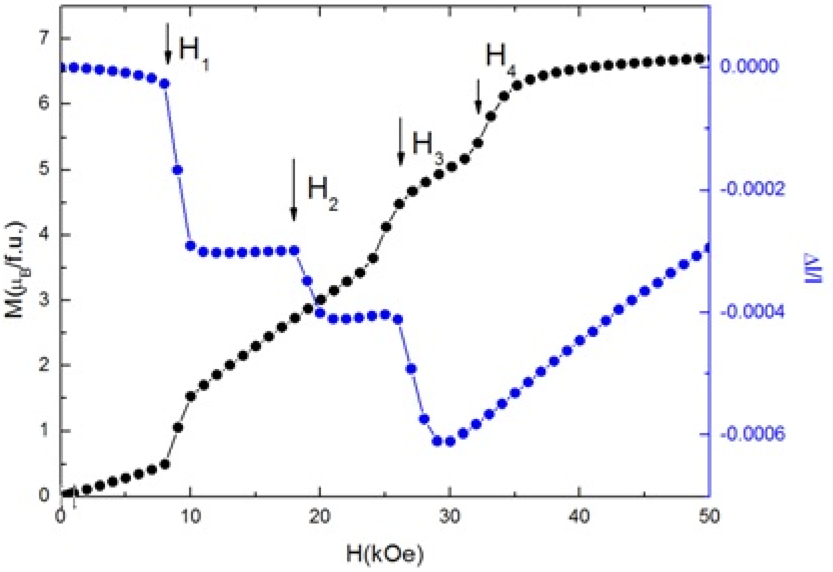

Figure 6.6: SQUID magnetisation and magnetostriction measurements below T$_M$ as a function of applied field. Four metamagnetic phase transitions are formed by the application of an increasing magnetic field along the a axis [35].

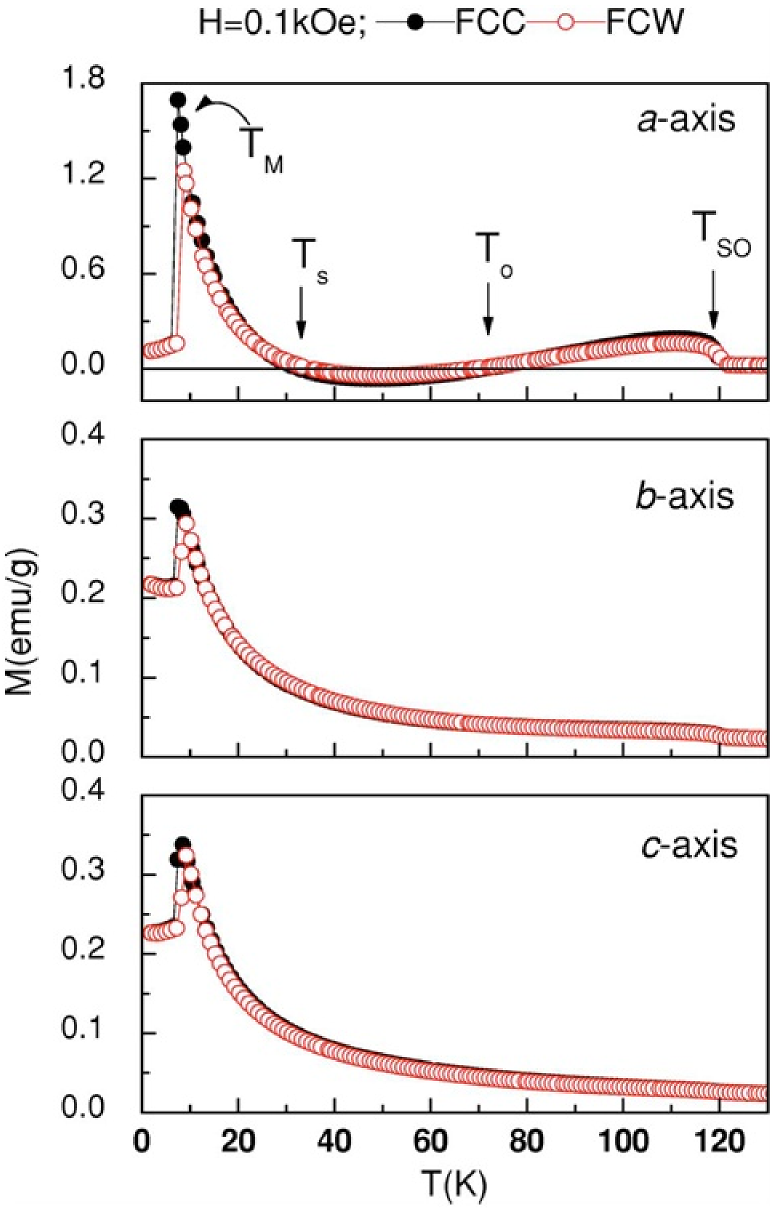

Figure 6.7: FCC (Field Cooled Cooling), FCW (Field Cooled Warming) magnetisation of the GdVO$_3$ single crystal measured at 0.1 kOe along the main axes. After Tung [35].

6.3.2 D9 results

The following results show the field dependence of the $(00\bar{2})$ peak at T = 4.5K.

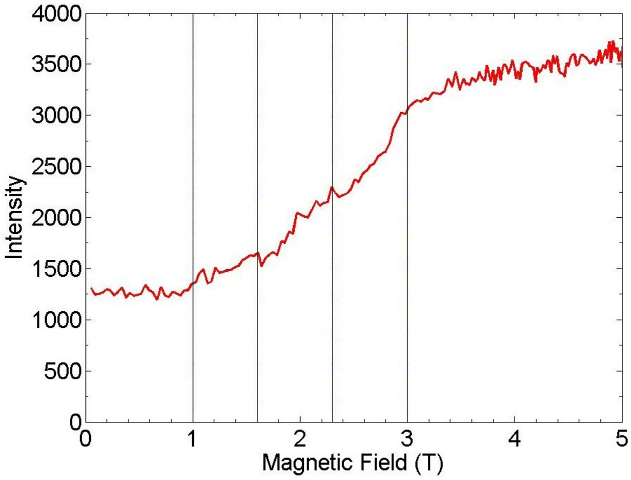

Figure 6.8: D9 field dependence of the GdVO$_3$ $(00\bar{2})$ peak at 4.5K with field increasing. The lines indicate changes of slope and these are interpreted as phase transitions.

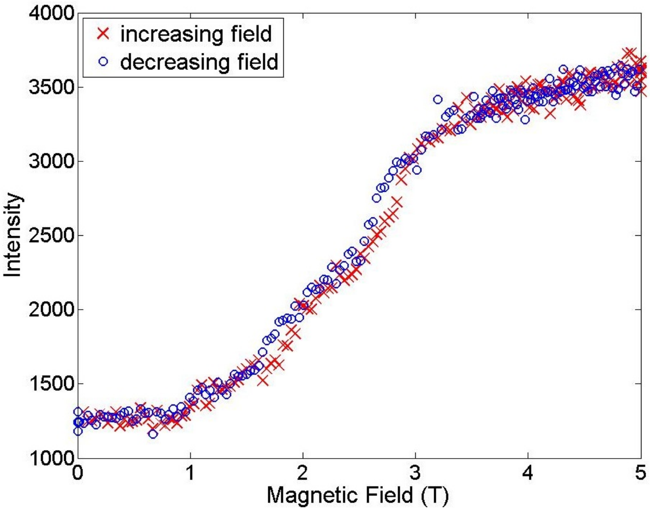

Figure 6.9: D9 field dependence measurements of the GdVO$_3$ $(00\bar{2})$ peak at 4.5K showing a very small hysteresis.

Our subsequent experiments on D9 show that GdVO$_3$ undergoes a transition to an incommensurate magnetic structure below T$_M$ (8K). Furthermore, we find that this is an intermediate phase and there is a transition to another incommensurate phase at T $\approx$ 7.5K.

The following results are from the hot neutron source, D9, at the ILL. Figures 6.10(a) and (b) show the temperature dependence of **Q** in zero field, and Figures 6.11 (a) and (b) show the field dependence of **Q** at 2K. We have focussed on the low temperature region of the phase diagram below TM (8K). We find incommensurate magnetic modulations for the first time in RVO$_3$ compound. Five distinct antiferromagnetic phases were found, labelled AF1 up to AF5.

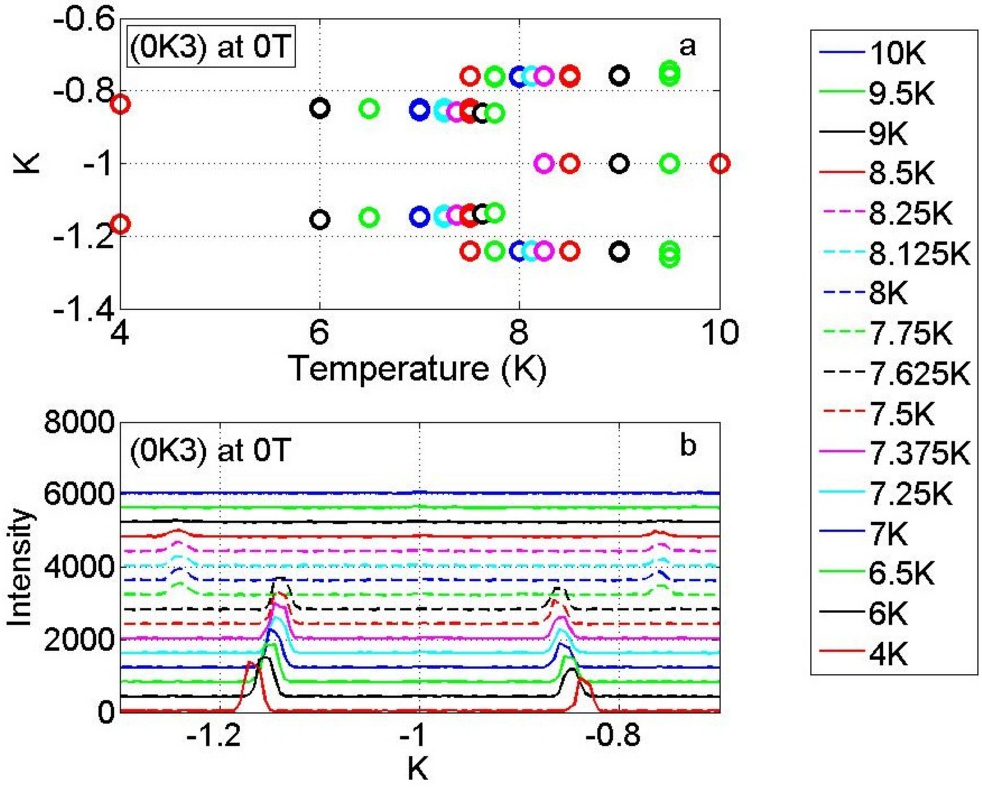

Figure 6.10: The temperature dependence of the incommensurate superlattice peaks of (0K3) in zero field using D9. There is a phase transition at about 7.5K, from AF1 to AF5 with a small region of coexistence between phases and a transition from AF5 to PM at about 9.5K.

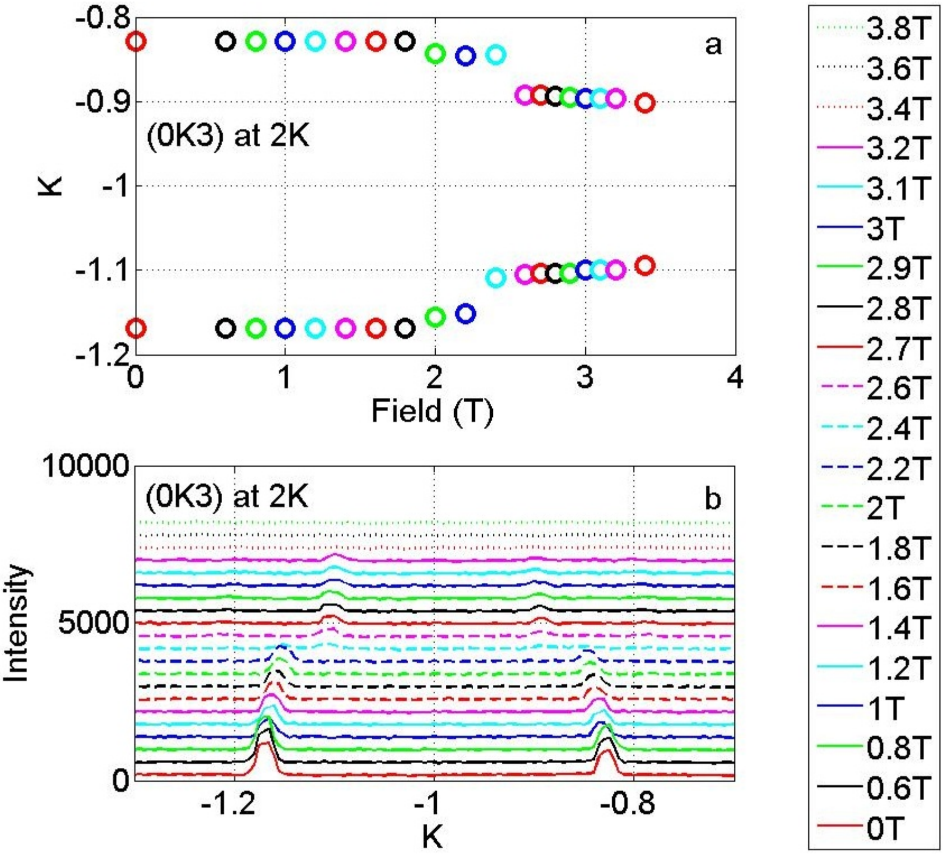

Figure 6.11: The field dependence of the incommensurate superlattice peaks of (0K3) at 2K using D9. Phase transitions can be seen at 1.8T (AF1 to AF2), at 2.4T (AF2 to AF3) and at 3.4T (AF3 to AF4). The crystal becomes ferromagnetic above 3.4T.

6.3.3 ID20 results

The species selectivity of resonant X-rays enables us to focus on the magnetism of the Gadolinium. Furthermore, since this is not a signal-limited technique, we are able to determine the phase diagram in much greater detail than before with neutrons.

Experiments using resonant X-ray scattering on ID20 at the ESRF confirmed the presence of an incommensurate phase below T = 8K. Magnetic scattering was not isolated at the Vanadium K edge (5.465 keV) and there was little resonance enhancement. On the other hand, strong resonant scattering was found at the Gadolinium L_{II} edge (7.932 keV). Figure 6.12 shows energy scans at this edge; the published Gadolinium L_{II} edge, E = 7.93 keV, is shown as a red line in the figure. It agrees to within 1 eV with the point of inflection of the fluorescence scan confirming instrumental energy calibration. Scans of X-ray energy with wavevector transfer fixed at $\mathbf{Q}$= (0, 2.84, 2) show a very large resonant enhancement of the signal within 1 eV of the Gadolinium L_{II} edge in both the $\pi\sigma$ and $\pi\pi$ channels. This signal is peaked in $\mathbf{Q}$ at an incommensurate wave-vector similar to that observed using magnetic neutron diffraction. We associate this peak with magnetic scattering from the Gadolinium moments.

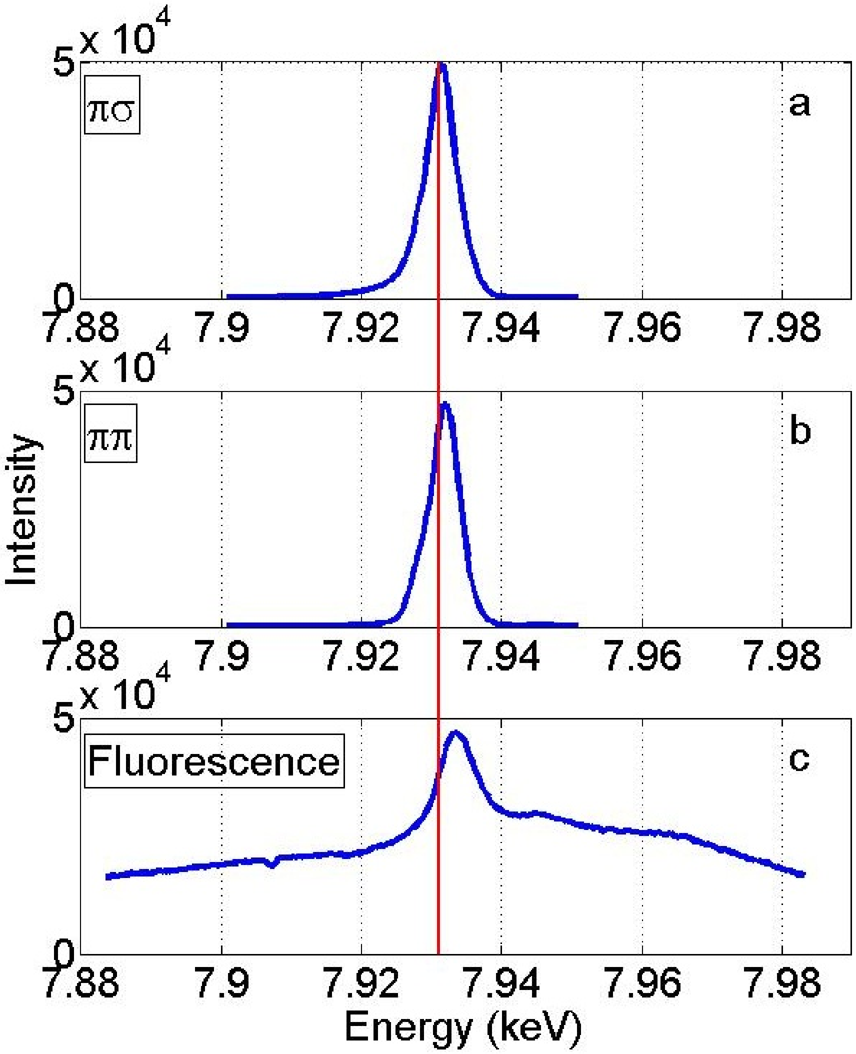

Figure 6.12: Resonant X-ray Scattering scans of (0K2) in a) $\pi\pi$ channel b) $\pi\sigma$ channel and c) the fluorescence spectrum (from ID20). The red line shows the Gadolinium L_{II} edge at ~7.93keV.

At temperatures below T = 10K, the Gadolinium moments were seen to order in four different competing magnetic phases apart from a forced ferromagnetic state at applied field greater than B = 3T. At T = 2K and zero field (see Figure 6.13), the Gadolinium moments order with the propagation vector (0, 2.833, 2)

(AF1 phase) which does not change significantly up to B = 0.75T. At B = 1T, the propagation vector shifts to (0, 2.843, 2) (AF2 phase). This corresponds well with a jump observed at around B = 0.9T observed both in the magnetisation and magnetostriction data. At around 1.75T, the third magnetic phase (AF3) with two distinct peaks located at around (0, 2.803, 2) and (0, 2.899, 2) in the $\pi\sigma$ channel appeared. These two peaks were slightly moved to higher k values with increasing applied field. At 2.5T, the compound changes to a new magnetic phase with propagation vector of about (0, 2.759, 2) (AF4) before reaching the forced ferromagnetic state (FM) at 3T. The positions of the three transitions AF2-AF3, AF3-AF4, and AF4-FM observed in the magnetic X-ray scattering data are in good agreement with the magnetisation and magnetostriction data. Figures 6.13 and 6.14 show the change in the propagation vector as temperature and field vary. Phases AF1 and AF2 have the same propagation vector but different moment directions. AF2 is seen only in the $\pi\sigma$ channel which is sensitive to moments in the b and c directions. AF1 is present in both channels. The $\pi\pi$ channel is sensitive only to moments in the a direction (the direction of the field). Figures 6.15 to 6.20 show the field and temperature dependence of Q in both the $\pi\pi$ and $\pi\sigma$ channels.

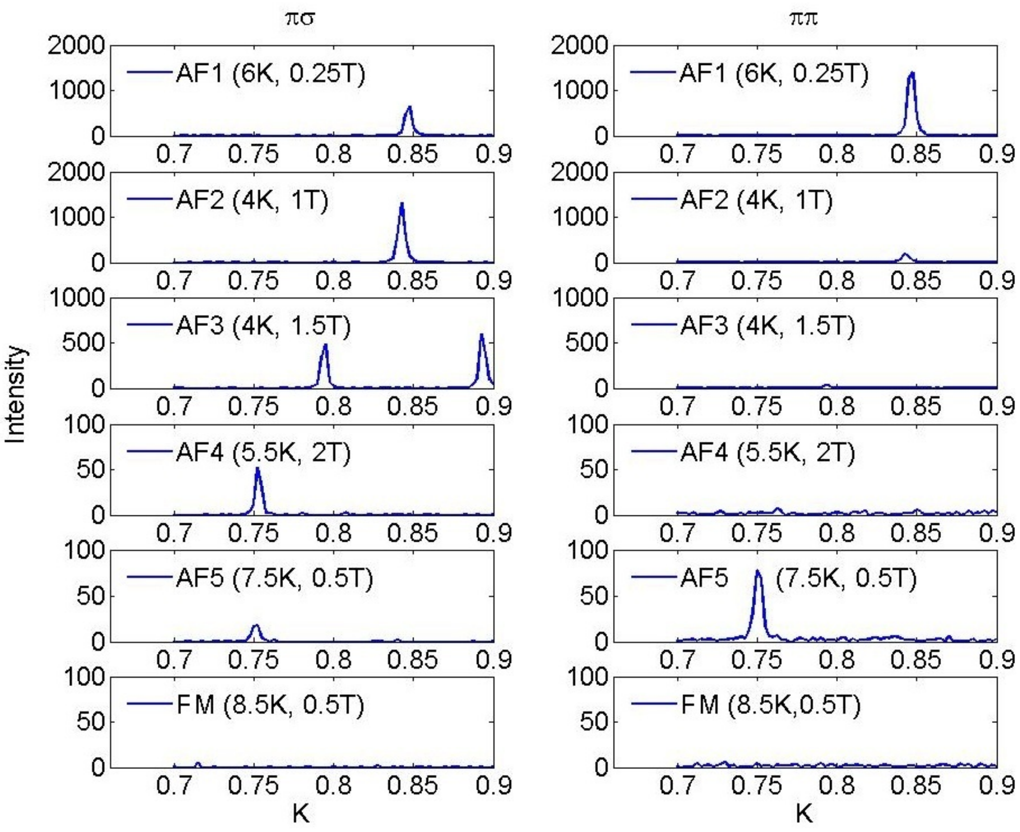

Figure 6.13: X-ray results from ID20 showing the typical data in each phase AF1, AF2, AF3, AF4, FM at different temperatures and fields at (0K4) in both the $\pi\sigma$ and $\pi\pi$ channels.

A systematic study at fixed temperature is shown in Figure 6.14; the signal in the $\pi\pi$ channel decreases as field increases. This infers that $GdVO_3$ has an antiferromagnetic structure with spin flop occurring (moments turning perpendicular to the field) as the field is raised. (The modulated Gadolinium moment component becomes restricted to the bc plane and there is only a ferromagnetic moment component along (100)). Phases AF4 and AF5 also have the same propagation vector but AF4 is seen in the $\pi\sigma$ channel and AF5 in the $\pi\pi$ channel.

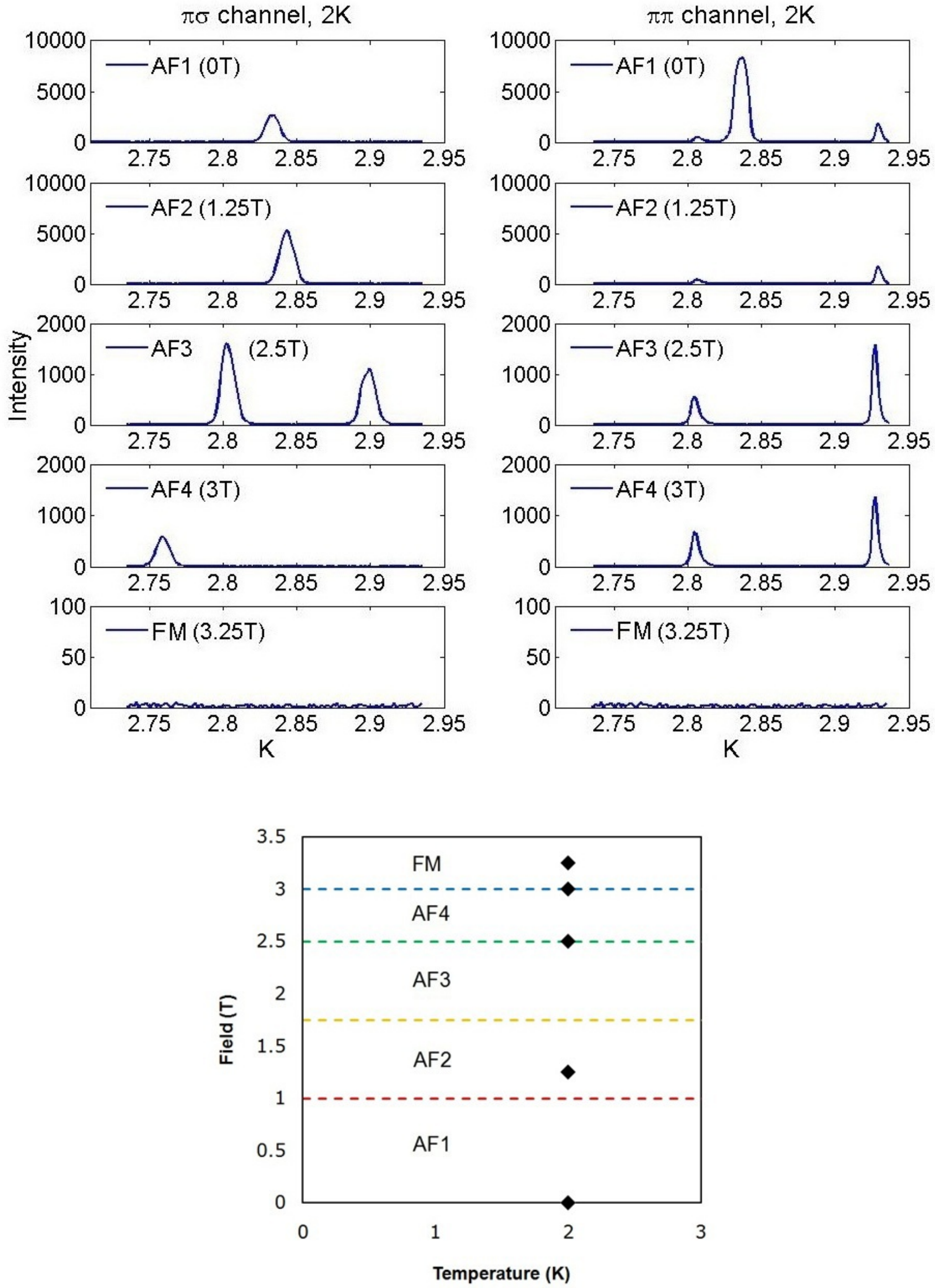

Figure 6.14: X-ray data from ID20 at 2K showing the phases AF1, AF2, AF3, AF4, FM of (0K2) as a function of field in the $\pi\sigma$ and $\pi\pi$ channels. The bottom panel shows the phase boundaries and where in each phase the measurements were taken.

Field dependence of Q

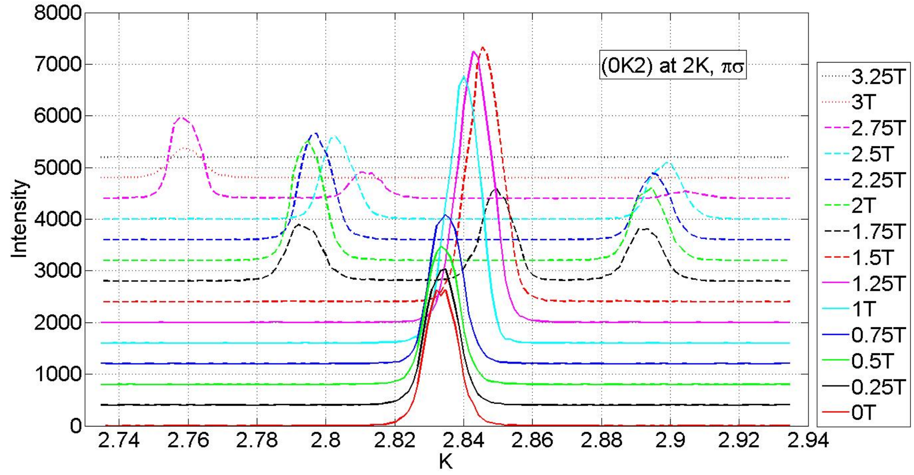

Figure 6.15: The scattering near (0K2) at 2K in the $\pi\sigma$ channel. Phase changes can be seen at 1T (AF1 to AF2), at 1.75T (AF2 to AF3), at 2.5T (AF3 to AF4). The material becomes ferromagnetic beyond 3T.

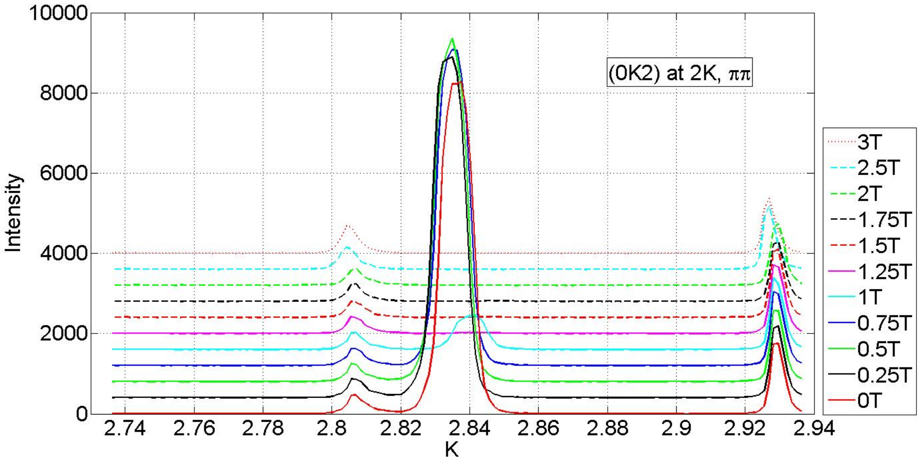

Figure 6.16: The scattering near (0K2) at 2K in the $\pi\pi$ channel. A phase transition can be seen at 1T (AF1 to AF2).

Temperature dependence of Q

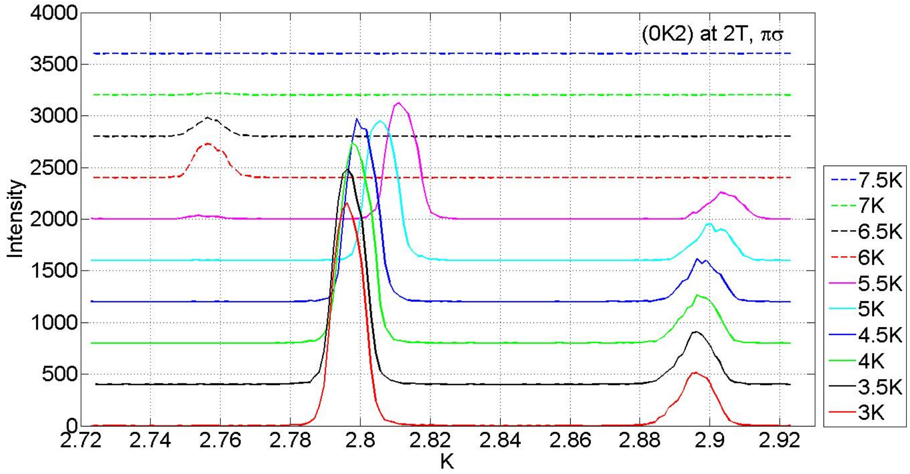

Figure 6.17: The scattering near (0K2) at 2T in the $\pi\sigma$ channel. A phase change can be seen at 6K (AF1 to AF4). The material becomes ferromagnetic beyond 7K.

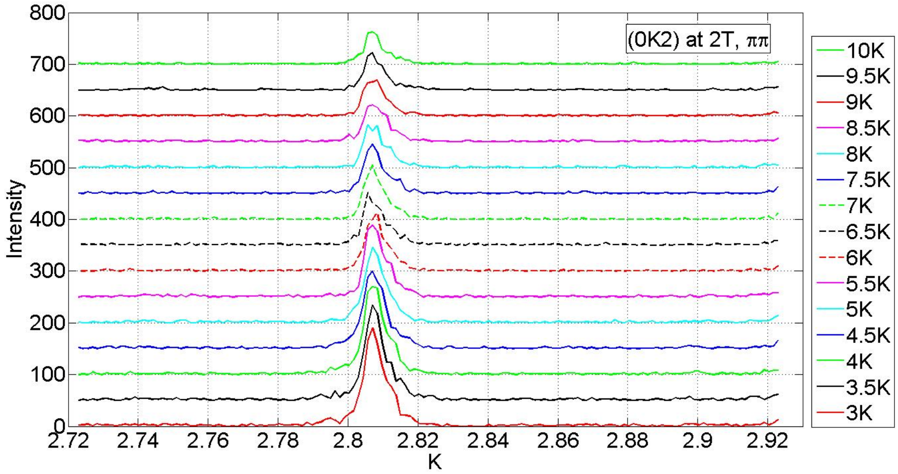

Figure 6.18: The scattering near (0K2) at 2T in the $\pi\pi$ channel.

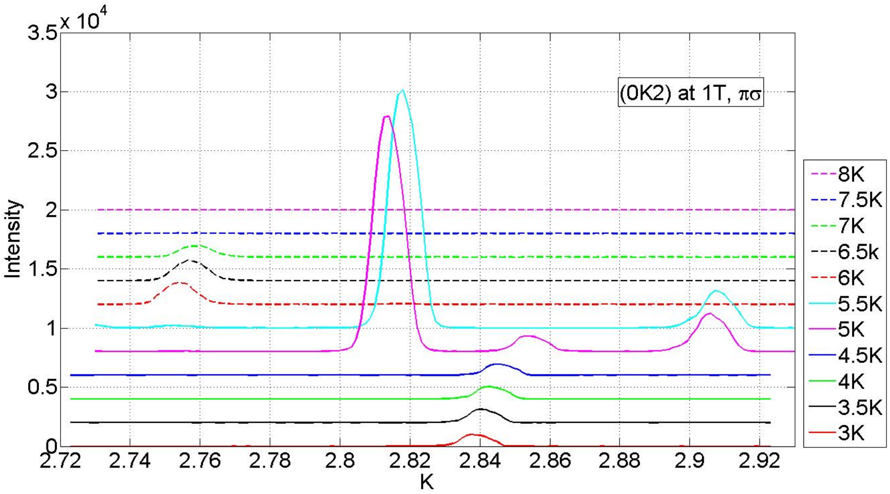

Figure 6.19: The scattering near (0K2) at 1T in the $\pi\sigma$ channel. Phase changes can be seen at 5K (AF2 to AF3) and at 6K (AF3 to AF4). The material becomes ferromagnetic beyond 7.5K.

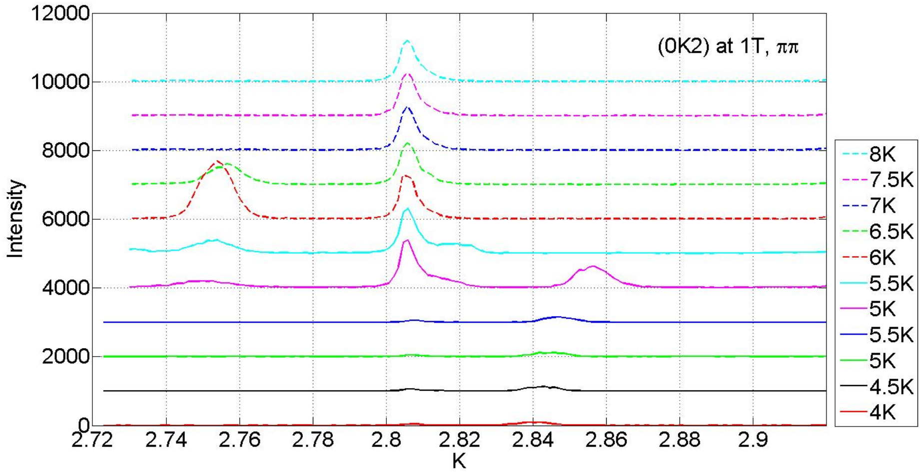

Figure 6.20: The scattering near (0K2) at 1T in the $\pi\pi$ channel. Again phase changes can be seen at 5K (AF2 to AF3) and at 6K (AF3 to AF4).

6.4 Phase diagram

The magnetic phase diagram of GdVO$_3$ at low temperature is comprised of incommensurate orderings of the Gd moments. Using neutrons we produced a phase diagram with four phases, AF1 to AF4, but by using polarised X-rays at ID20 we were able to deduce that there are in fact five separate phases in GdVO$_3$ (see Figure 6.21). AF4 and AF5 are phases with the same propagation vector but different moment directions. The phase boundaries determined from Figure 6.21 ($H1 = 1T$, $H2 = 1.75T$, $H3 = 2.5T$, $H4 = 3T$), correspond to the phase boundaries from magnetisation and magnetostriction data in Figure 6.6 ($H1 = 0.8T$, $H2 = 1.8T$, $H3 = 2.6T$, $H4 = 3.15T$). The small discrepancies in these values may be due to demagnetisation effects.

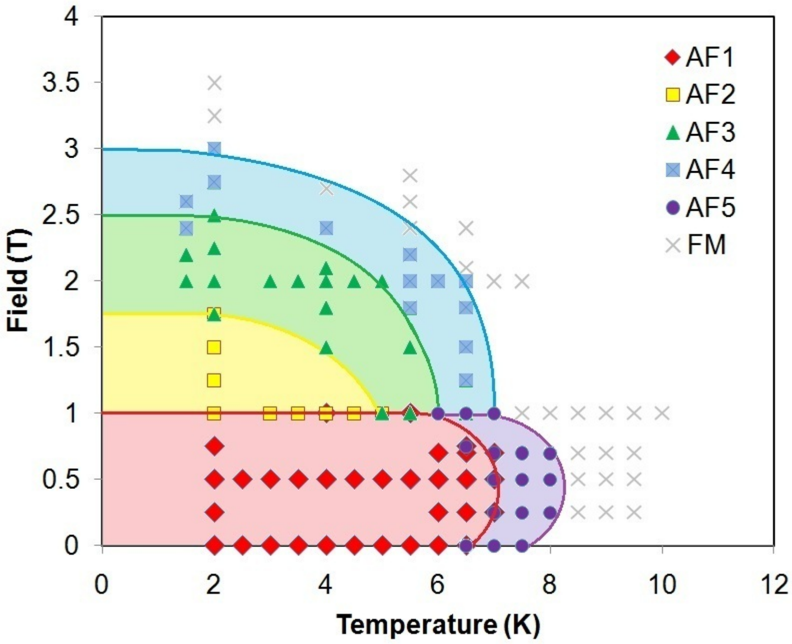

Figure 6.21: Phase diagram for GdVO$_3$ produced using data from ID20.

6.5 Modelling of resonant magnetic scattering

It is clear from the very large resonant enhancement at the Gd L$_{II}$ edge in Figure 6.12 that in order to model the data it is sufficient to consider the ordering of the Gadolinium moments only. For rare earths the dipolar contribution to the scattering is dominant at the L edges. The magnetic intensity is given by

$$I = |\sum_j f_{E1}\ e^{i\mathbf{Q}.\mathbf{r}_j}|^2 \tag{6.1}$$

where the summation is over the magnetic unit cell. The magnetic form factor for the $\pi\sigma$ channel is given by

$$f_{E1}^{\pi\sigma} = iF_{E1}(z_1 cos\theta + z_3 sin\theta) \tag{6.2}$$

and for the $\pi\pi$ channel it is

$$f_{E1}^{\pi\pi} = -iF_{E1}(z_2 sin2\theta) \tag{6.3}$$

Since one matrix element in the cross section dominates it is sufficient to treat F_{E1} as a constant experimental scale factor. The coordinate system for resonant x-ray scattering is shown in Figure 6.22. The moment components are $\mathbf{z}_1$ perpendicular to $\mathbf{Q}$ in the scattering plane, $\mathbf{z}_2$ perpendicular to $\mathbf{Q}$ and perpendicular to the scattering plane and $\mathbf{z}_3$ parallel to $\mathbf{Q}$. These cross sections also depend on the

Bragg angle θ [102].

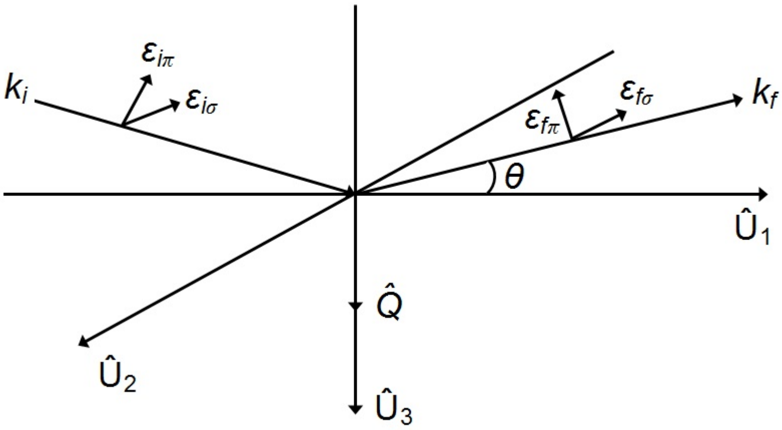

Figure 6.22: The coordinate system for resonant x-ray scattering

In order to compare calculated intensities with the data it is necessary to perform an absorption correction. The measurements were performed in reflection geometry from a polished surface. Hence the calculated intensity is multiplied by inverse absorption correction for a flat plate.

$$A^{-1} = \mu \left(1 + \frac{sin\ \psi}{sin(2\theta - \psi)}\right) \tag{6.4}$$

where 2θ is the scattering angle, μ is the linear absorption coefficient and ψ is the angle between the incident beam and the plate [103].

Figure 6.23 shows the calculated scattering with a transverse sinusoidal modulation of the moments along the a direction. This model predicts intensity in the $\pi\pi$ channel only. The observations of substantial intensity in the $\pi\sigma$ channel rules this model out. Similarly, the calculations for a longitudinal sinusoidal modulation with moments along the b-direction (Figure 6.24) and a transverse sinusoidal modulation with moments along the c-direction (Figure 6.25) predict intensity in the $\pi\sigma$ channel only. The observation of intensity in the $\pi\pi$ channel rules out these two collinear structures.

The calculations for a cycloidal structure with moments in the ab plane (Figure 6.26) and a helical structure with moments in the ac plane (Figure 6.27) give peaks where expected, and there is some qualitative agreement with the data. The model proposed for TbMnO$_3$ [104] has sinusoidal variation of components of the Tb along a and b. Application of this model to GdVO$_3$ (Figure 6.28) also gives some qualitative agreement with the data.

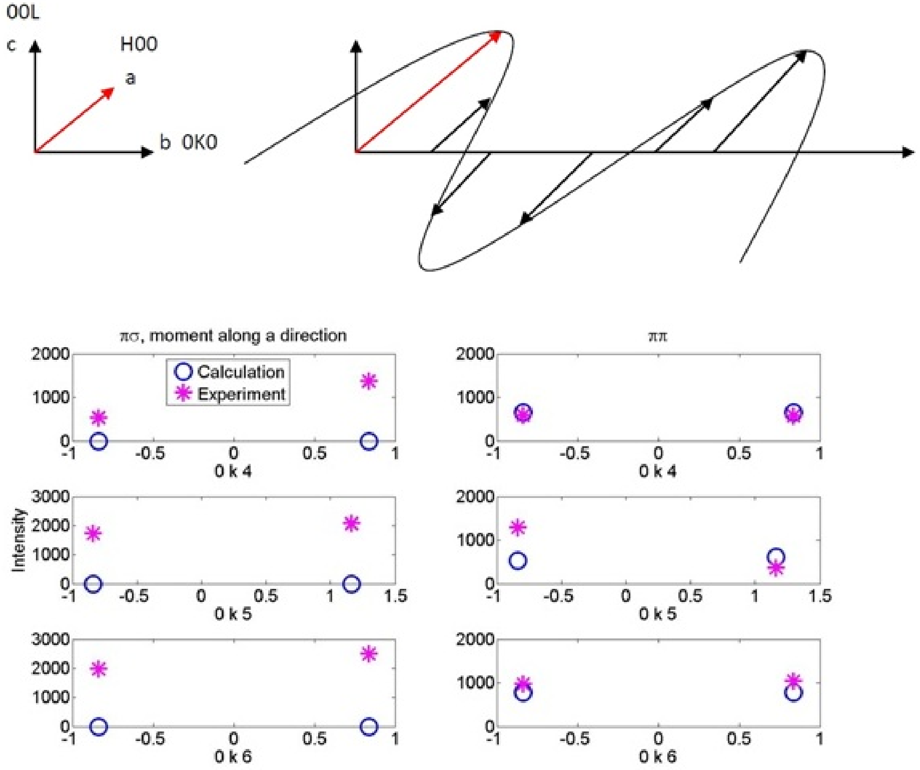

Figure 6.23: The experimental data (pink stars) are compared with calculations (blue circles) for the transverse sinusoidal modulation with moments along the a direction. The observed intensity in the $\pi\sigma$ channel rules out this model.

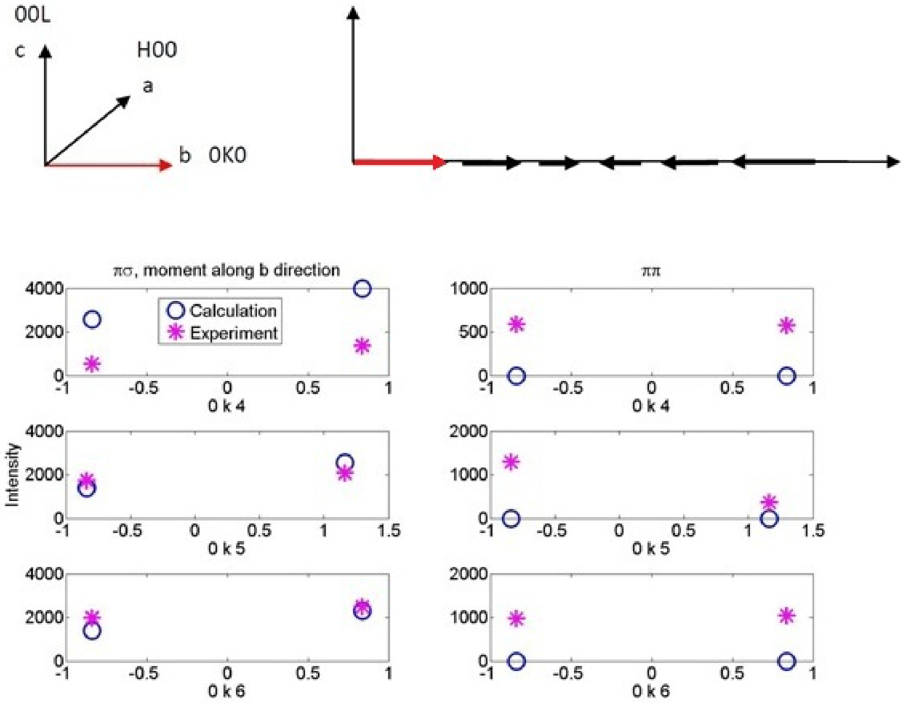

Figure 6.24: The experimental data (pink stars) are compared with calculations (blue circles) for the longitudinal sinusoidal modulation with moments along the b direction. The observed intensity in the $\pi\pi$ channel rules out this model.

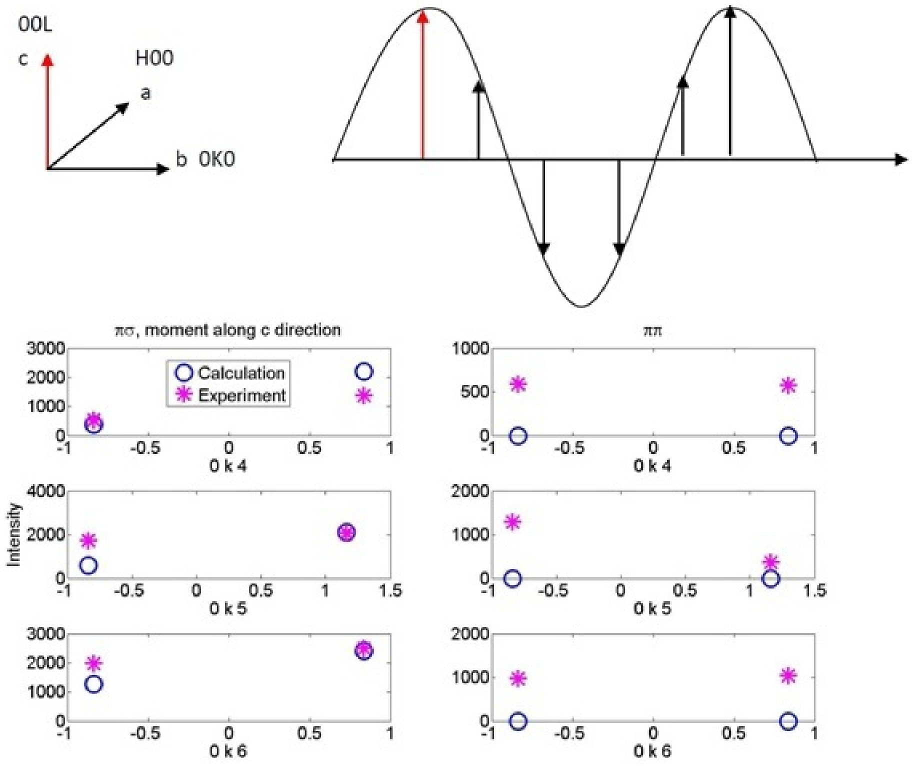

Figure 6.25: The experimental data (pink stars) are compared with calculations (blue circles) for the transverse sinusoidal modulation with moments along the c direction. The observed intensity in the $\pi\pi$ channel rules out this model.

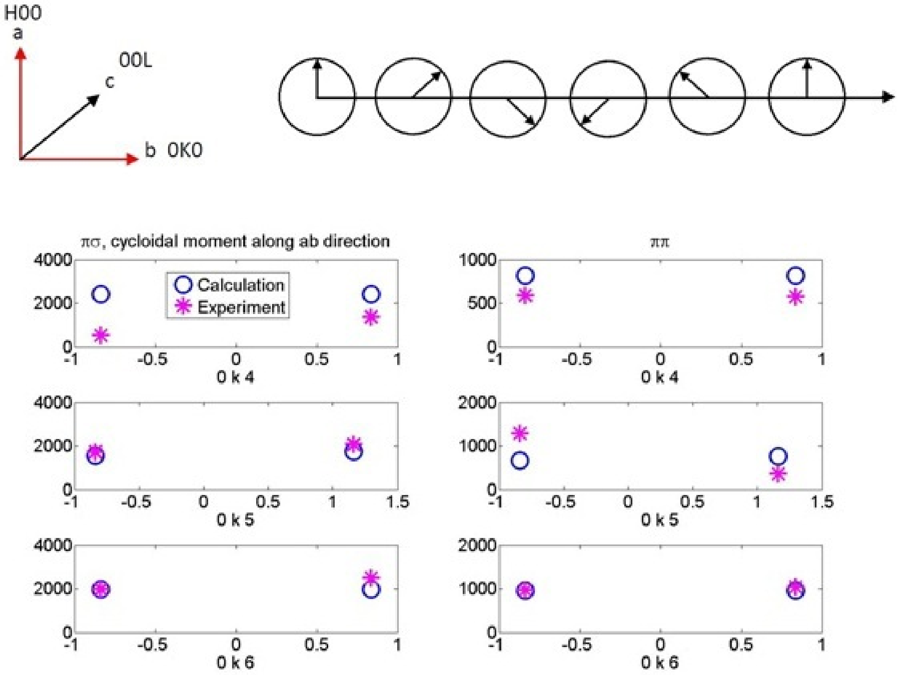

Figure 6.26: The experimental data (pink stars) are compared with calculations (blue circles) for a cycloidal structure with moments in the ab plane.

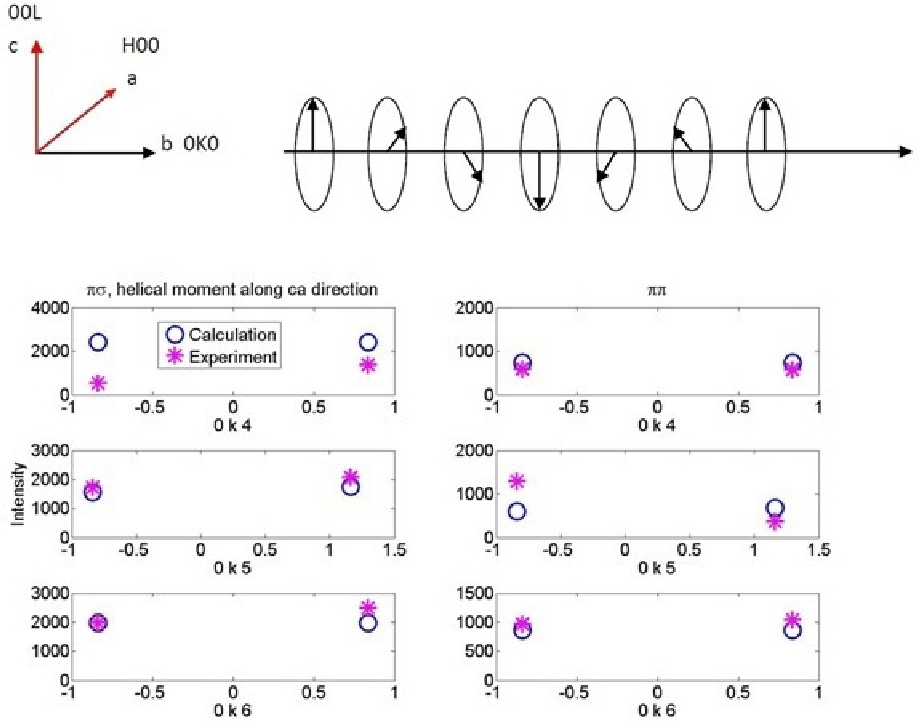

Figure 6.27: The experimental data (pink stars) are compared with calculations (blue circles) for a helical structure with moments in the ac plane.

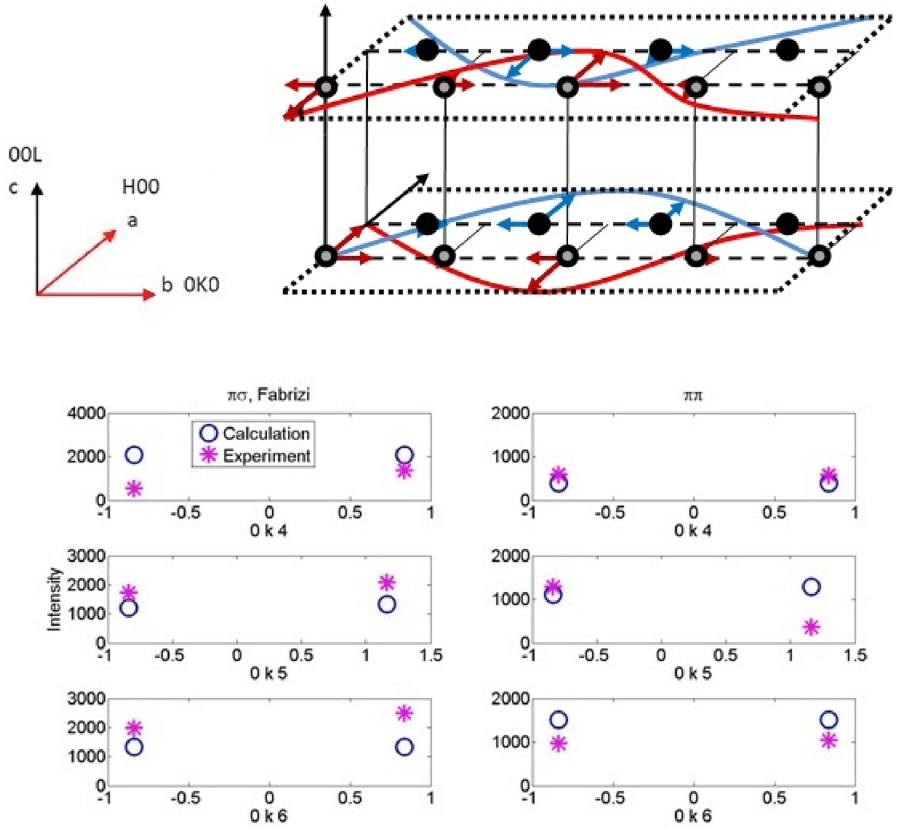

Figure 6.28: The experimental data (pink stars) are compared with calculations (blue circles) for a structure with both transverse and longitudinal components as described in Fabrizi *et al.* [104]

6.6 Discussion

Gadolinium has not been studied before due to its high neutron absorption cross section and GdVO$_3$ turns out to have very different magnetic properties to the other RVO$_3$ compounds at low temperature. We find a complicated phase diagram of incommensurate orderings at low temperature, and this may be linked to the unusual magnetic memory effect observed in bulk measurements. Gadolinium has a half-filled shell and, therefore, no anisotropy. This should make it easier to form incommensurate magnetic structures than the other RVO$_3$ compounds.

The resonant X-ray scattering technique allows us to focus on the ordering of the Gadolinium. Because it is not a signal limited technique, it is possible to map out the phase diagram accurately. Furthermore we find that two regions that looked the same using unpolarised neutrons are shown to have very different moment directions using the polarisation dependence of the X-ray scattering. Indeed the polarisation results allow some robust conclusions to be drawn on the magnetic structure. So, for example, the zero field structure has a significant component along the a direction. Transverse and longitudinal sinusoidal moments have been ruled out. The experimental uncertainty allows for the possibility of a helical structure, a cycloidal structure or a model with both transverse and longitudinal components, as reported for TbMnO$_3$ by Fabrizi *et al.* [104] (see Figure 6.29).

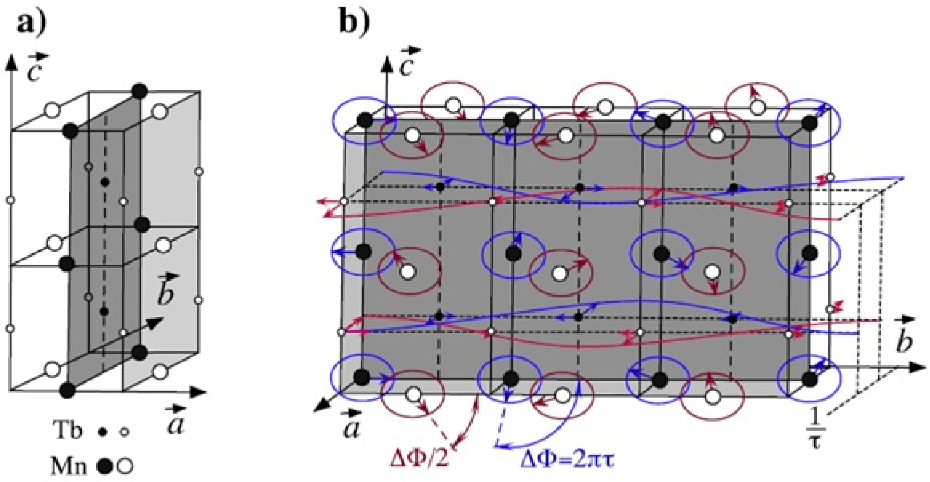

Figure 6.29: (a) Crystallographic and (b) magnetic structures of TbMnO$_3$ [104].

We attempted to measure a much larger set of magnetic reflections, but we were not confident that the peaks were fully maximised, except for those shown in Figures 6.23 - 6.28. Obtaining reliable structure factors over a wide range of **Q** is diffcult with X-rays, due to the movement of the beam on the sample, etc. Our approach of measuring the neutron structure factors in the zero-field phase at base temperature should at least have given reliable structure factors. However, to date we have not succeeded in obtaining a satisfactory fit to the data. An alternative promising approach that might work with X-rays might be to use non-resonant circularly polarised studies, as performed recently with TbMnO$_3$ (The full magnetic structure for TbMnO$_3$ is shown in Figure 6.29). This would have the advantage of only requiring data from a small range of **Q** and would also be sensitive to the vanadium moments.

7 Conclusions

The work presented in this thesis includes the study of the orbital ordering and magnetism of the spinel MnV_2O_4 (Chapters 4 and 5) and the perovskite ortho-vanadate $GdVO_3$ (Chapter 6) using synchrotron radiation and neutron scattering techniques.

The MnV_2O_4 single-crystal neutron diffraction data (Section 5.3.1 and 5.3.2) and the McPhase calculations (Section 5.5) agree with the magnetic structure predicted by Garlea *et al.* [42] who proposed that the V^{3+} moments have antiferromagnetic components in the ab plane, staggered along the c axis, with the angle of canting of V^{3+} moments from c axis, $\theta = 65.12°$ (Section 4.1.3 , Figure 4.7).

We also show that the structural transformation to $I4_1/a$ occurs at $T_N = 57K$ and not at T_M= 53K as reported by others [38, 42–45]. Our results agree with Suzuki *et al.* [75] who performed single crystal synchrotron measurements (Section 4.1.1). The $I4_1/a$ structural space group determined by Suzuki *et al.* and our three dimensional magnon dispersion results rule out several proposed orbital ordering models [33,38] which left only the model of Sarkar *et al.* [41]. This model predicts that all t_{2g} levels are partially occupied which gives orbital chains running along a and b, ferro-orbital order and the correct $I4_1/a$ structure. The orbitals within each chain are rotated alternately by 45° an effect caused by a staggered trigonal distortion [41] (Section 4.1.2, Figure 4.5). The fact that the orbitals are all partially occupied explains why the magnon excitations are three dimensional.

Also, Sarkar *et al.* [41] predict an interchain to intrachain ratio of $J_{BB'}/J_{BB} \approx 0.2$, and this agrees qualitatively with our estimate of $J_{BB'}/J_{BB} \approx 0.3$. Our results show that a previous attempt by Chung *et al.* [79] to model the excitations of MnV_2O_4 were incorrect (Section 5.1.1, Figure 5.1). The model was corrected and the parameters changed to produce the best fit to the data but some characteristics of the dispersions were unaccounted for. Our new evidence in support of the Garlea structure show that the Chung model uses the wrong ground state. The use of the correct ground state with the McPhase program showed that these features could be modelled, although this work is still ongoing (Section 5.5). Models of the dispersion produced using McPhase also show that the dispersion is very complicated and that it is just the higher intensity modes which had been seen in experiment (Figure 5.12). A detailed phase diagram for MnV_2O_4 was determined using synchrotron X-rays (Section 4.3.5, Figure 4.20).

The complex magnetic ordering in $GdVO_3$ was studied using hot neutrons (Section 6.3.2). This was not previously possible using thermal neutron instruments due to the strongly absorbing nature of Gadolinium [99]. Resonant X-ray scattering was also used to study the ordering of the Gadolinium (Section 6.3.3). The rich magnetic phase diagram of $GdVO_3$ has been determined at low temperature (Section 6.4, Figure 6.21) and is comprised of *incommensurate* orderings of Gadolinium moments which may be linked to its magnetic memory effect observed on bulk measurements [35]. It is likely that $GdVO_3$ forms incommensurate structures because Gadolinium has no anisotropy. Two regions on the phase diagram which appeared to be the same when using unpolarised neutrons have been shown to have different moment directions using polarisation dependence of X-ray scattering. An attempt has been made to model the magnetic structure (Section 6.5) and our results reveal sinusoidal modulation with components perpendicular and parallel to the modulation direction.

Bibliography

[1] Raymond A. Serway and Robert J. Beichner. *Physics for Scientists and Engineers with Modern Physics.* Saunders College Publishing, Orlando, 5th edition, 2000.

[2] R. V. Gaines, H. C. W. Skinner, E. E. Foord, B. Mason, and A. Rosenzweig. *Dana's New Mineralogy.* Wiley, New York, 8th edition, 1997.

[3] Mark T. Weller, Robert W. Hughes, Joanna Rooke, Christopher S. Knee, and Jon Reading. The pyrochlore family - a potential panacea for the frustrated perovskite chemist. *Dalton Trans.*, pages 3032–3041, 2004.

[4] Jason S. Gardner, Michel J. P. Gingras, and John E. Greedan. Magnetic pyrochlore oxides. *Rev. Mod. Phys.*, 82(1):53, Jan 2010.

[5] J. R. Hook and H. E. Hall. *Solid State Physics.* John Wiley & Sons, 2nd edition, 1991.

[6] J. M. D. Coey, M. Viret, and S. von Molnr. Mixed-valence manganites. *Advances in Physics*, 48(2):167–293, 1999.

[7] Stephen Blundell. *Magnetism in Condensed Matter.* Oxford University Press, Oxford, 2001.

[8] Des McMorrow. Order and excitations in condensed matter. *Course notes*, 2006.

[9] Y. Tokura and N. Nagaosa. Orbital Physics in Transition-Metal Oxides. *Science*, 288(5465):462–468, 2000.

[10] Russell A. Ewings. Neutron and x-ray scattering studies of strongly correlated electron systems. *PhD thesis*, 2008.

[11] H. A. Jahn and E. Teller. Stability of polyatomic molecules in degenerate electronic states. I. orbital degeneracy. *Proceedings of the Royal Society of London. Series A - Mathematical and Physical Sciences*, 161(905):220–235, 1937.

[12] H. A. Kramers. The interaction of magnetogenic atoms in paramagnetic crystals. *Physica*, 1(1-6):182 – 192, 1934.

[13] Jae-Ho Chung, William Ratcliff, and Owen Vajk. The magnetic phase transition and spin wave excitations in the perovskite $La_{0.7}Sr_{0.3}MnO_3$: An exper-

iment using the spins triple-axis spectrometer. *Summer School on Methods and Applications of Neutron Spectroscopy Course Notes*, 2005.

[14] Daniel Khomskii. Classifying multiferroics: Mechanisms and effects. *http://physics.aps.org/articles/v2/20*, March 2009.

[15] R. Moessner and A. P. Ramirez. Geometric frustration. *Phys. Today*, 59:2429, 2006.

[16] Narayani Choudhury, Laura Walizer, Sergey Lisenkov, and L. Bellaiche. Geometric frustration in compositionally modulated ferroelectrics. *Nature*, 470:513517, Feb 2011.

[17] A. P. Ramirez. Geometric frustration: Magic moments. *Nature*, 421:483 – 483, Jan 2003.

[18] Steven T. Bramwell and Michel J. P. Gingras. Spin ice state in frustrated magnetic pyrochlore materials. *Science*, 294(5546):1495–1501, 2001.

[19] M. J. Harris. Taking the frustration out of ice. *Nature*, 399:311312, 1999.

[20] S. H. Lee. Emergent excitations in a geometrically frustrated magnet. *Nature*, 418:856858, 2002.

[21] C. Castelnovo, R. Moessner, and S. L. Sondhi. Magnetic monopoles in spin ice. *Nature*, 451:4245, 2008.

[22] J. Hemberger. Relaxor ferroelectricity and colossal magnetocapacitive coupling in ferromagnetic $CdCr_2S_4$. *Nature*, 434:364367, 2005.

[23] I. S. Hagemann, P. G. Khalifah, A. P. Ramirez, and R. J. Cava. Geometric magnetic frustration in olivines. *Phys. Rev. B*, 62(2):R771–R774, Jul 2000.

[24] M. Mostovoy. Multiferroics go high-T C. *Nature Mater.*, 7:269270, 2008.

[25] L. Balents. Spin liquids in frustrated magnets. *Nature*, 464:199208, 2010.

[26] J. P. Sethna. Frustration and curvature: glasses and the cholesteric blue phase. *Phys. Rev. Lett.*, 51:21982201, 1983.

[27] Linus Pauling. The structure and entropy of ice and of other crystals with some randomness of atomic arrangement. *Journal of the American Chemical Society*, 57(12):2680–2684, 1935.

[28] L. Krusin-Elbaum, D. M. Newns, H. Zeng, V. Derycke, J. Z. Sun, and R. Sandstrom. Room-temperature ferromagnetic nanotubes controlled by electron or hole doping. *Nature*, 431:672– 676, Oct 2004.

[29] Vibha Kalra, Jung Hun Lee, Jay Hoon Park, Manuel Marquez, and Yong Lak Joo. Confined assembly of asymmetric block-copolymer nanofibers via multiaxial jet electrospinning. *Small*, 5(20):2323–2332, 2009.

[30] S. T. Bramwell, S. R. Giblin, S. Calder, R. Aldus, D. Prabhakaran, and

T. Fennell. Measurement of the charge and current of magnetic monopoles in spin ice. *Nature*, 461:956 – 959, 2009 Oct.

[31] D. J. P. Morris, D. A. Tennant, S. A. Grigera, B. Klemke, C. Castelnovo, R. Moessner, C. Czternasty, M. Meissner, K. C. Rule, J.-U. Hoffmann, K. Kiefer, S. Gerischer, D. Slobinsky, and R. S. Perry. Dirac strings and magnetic monopoles in the spin ice $Dy_2Ti_2O_7$. 326(5951):411–414, 2009.

[32] G. Khaliullin. Order from disorder: Quantum spin gap in magnon spectra of $\mathrm{LaTiO_3}$. *Phys. Rev. B*, 64(21):212405, Nov 2001.

[33] Hirokazu Tsunetsugu and Yukitoshi Motome. Magnetic transition and orbital degrees of freedom in vanadium spinels. *Phys. Rev. B*, 68(6):060405, Aug 2003.

[34] S. H. Lee, D. Louca, H. Ueda, S. Park, T. J. Sato, M. Isobe, Y. Ueda, S. Rosenkranz, P. Zschack, J. Íñiguez, Y. Qiu, and R. Osborn. Orbital and spin chains in $\mathrm{ZnV_2O_4}$. *Phys. Rev. Lett.*, 93(15):156407, Oct 2004.

[35] L. D. Tung. Tunable temperature-induced magnetization jump in a $\mathrm{GdVO_3}$ single crystal. *Phys. Rev. B*, 73(2):024428, Jan 2006.

[36] R. Plumier and M. Sougi. Observation of a first order transition in the ferrimagnetic spinel $\mathrm{MnV_2O_4}$. *Solid State Communications*, 64(1):53 – 55, 1987.

[37] R. Plumier and M. Sougi. Observation of a first-order transition at T < Tc in MnV_2O_4. *Physica B: Condensed Matter*, 155(1-3):315 – 319, 1989.

[38] O. Tchernyshyov. Structural, orbital, and magnetic order in vanadium spinels. *Phys. Rev. Lett.*, 93(15):157206, Oct 2004.

[39] M. Reehuis, A. Krimmel, N. Büttgen, A. Loidl, and A. Prokofiev. Crystallographic and magnetic structure of ZnV_2O_4. *The European Physical Journal B - Condensed Matter and Complex Systems*, 35:311–316, 2003. 10.1140/epjb/e2003-00282-4.

[40] Masashige Onoda and Junichi Hasegawa. A distortion of pseudotetramers coupled with the Jahn Teller effect in the geometrically frustrated spinel system CdV_2O_4. *Journal of Physics: Condensed Matter*, 15(3):L95, 2003.

[41] S. Sarkar, T. Maitra, Roser Valentí, and T. Saha-Dasgupta. Proposed orbital ordering in MnV_2O_4 from first-principles calculations. *Phys. Rev. Lett.*, 102(21):216405, May 2009.

[42] V. O. Garlea, R. Jin, D. Mandrus, B. Roessli, Q. Huang, M. Miller, A. J. Schultz, and S. E. Nagler. Magnetic and orbital ordering in the spinel MnV_2O_4. *Phys. Rev. Lett.*, 100(6):066404, Feb 2008.

[43] K. Adachi, T. Suzuki, K. Kato, K. Osaka, M. Takata, and T. Katsufuji. Magnetic-field switching of crystal structure in an orbital-spin-coupled system: MnV_2O_4. *Phys. Rev. Lett.*, 95(19):197202, Nov 2005.

[44] S. H. Baek, K. Y. Choi, A. P. Reyes, P. L. Kuhns, N. J. Curro, V. Ramanchandran, N. S. Dalal, H. D. Zhou, and C. R. Wiebe. AC susceptibility and 51 V NMR study of MnV_2O_4. *Journal of Physics: Condensed Matter*, 20(13):135218, 2008.

[45] Gia-Wei Chern, Natalia Perkins, and Zhihao Hao. Quantum 120° model on pyrochlore lattice: Orbital ordering in MnV_2O_4. *Phys. Rev. B*, 81(12):125127, Mar 2010.

[46] Jens Als-Nielsen and Des McMorrow. *Elements of Modern X-ray Physics.* John Wiley & Sons, Ltd, 2001.

[47] Peter Normile. Neutron and resonant x-ray magnetic scattering studies of single-crystal $U_{1-x}Pu_xSb$. *PhD thesis*, 2001.

[48] G. L. Squires. *Introduction to the theory of thermal neutron scattering.* Cambridge University Press, Cambridge, 1978.

[49] A. C. Hannon, S. M. Bennington, and S. Langridge. Neutron training course booklets. *ISIS*, 2008.

[50] J. Doucet. Hercules neutron course notes. *Course notes*, 2004.

[51] J. P. Goff. Neutron scattering studies of fluorite compounds. *D. Phil. thesis*, 1992.

[52] D. H. Templeton and L. K. Templeton. X-ray dichroism and polarized anomalous scattering of the uranyl ion. *Acta Crystallographica Section A*, 38(1):62–67, Jan 1982.

[53] Markos Skoulatos. Spin correlations and orbital physics in vanadates. *PhD thesis*, 2008.

[54] European Synchrotron Radiation Facility. Id20 magnetic scattering beamline. *http://www.esrf.eu/UsersAndScience/Experiments/ElectStructMagn/ID20*, July 2011.

[55] Kazumichi Namikawa, Masami Ando, Tetsuo Nakajima, and Hiroshi Kawata. X-ray resonance magnetic scattering. *Journal of the Physical Society of Japan*, 54(11):4099–4102, 1985.

[56] Doon Gibbs, D. R. Harshman, E. D. Isaacs, D. B. McWhan, D. Mills, and C. Vettier. Polarization and resonance properties of magnetic x-ray scattering in Holmium. *Phys. Rev. Lett.*, 61(10):1241–1244, Sep 1988.

[57] Bruce. D. Gaulin. Introduction to inelastic neutron scattering. *NXS School*, May 2009.

[58] Joachim Kohlbrecher. POLDI (project). *http://poldi.web.psi.ch/poldi/poldi-alt.html*, Jan 2002.

[59] Institut Laue-Langevin. CRG - thermal neutron diffractometer for

single-crystals D15. *http://www.ill.eu/instruments-support/instruments-groups/instruments/d15/*, Nov 2009.

[60] Institut Laue-Langevin. Four-circle diffractometer with three-axis energy analysis D10. *http://www.ill.eu/instruments-support/instruments-groups/instruments/d10/*, Oct 2009.

[61] S. J. Lee. Magnetic properties of metastable phases in rare earth and transition metal superlattices. *PhD thesis*, 2004.

[62] Institut Laue-Langevin. Hot neutron four-circle diffractometer D9. *http://www.ill.eu/instruments-support/instruments-groups/instruments/d9/*, Aug 2009.

[63] Gen Shirane, Stephen M. Shapiro, and John M. Tranquada. *Neutron Scattering with a Triple-Axis Spectrometer: Basic Techniques.* Cambridge University Press, 2002.

[64] European Neutron Portal. 3-axis spectroscopy with neutrons. *http://pathfinder.neutron-eu.net/idb/methods/3Axis*, March 2006.

[65] G. H. Lander. Oxford summer school. *Course notes*, 2007.

[66] Institut Laue-Langevin. Thermal neutron three-axis spectrometer with polarization analysis IN20. *http://www.ill.eu/instruments-support/instruments-groups/instruments/in20/*, Nov 2008.

[67] R. A. Ewings and T. G. Perring. *Horace: visualising and manipulating S(Q,ω) measured in all four dimensions, http://horace.isis.rl.ac.uk/Main_Page*. ISIS, 2011.

[68] ISIS. Maps. *http://www.isis.stfc.ac.uk/instruments/maps//*, Aug 2011.

[69] ESRF. XMaS the UK-CRG. *http://www.esrf.eu/UsersAndScience/Experiments/CRG/BM28*, Aug 2011.

[70] M. E. Gallagher. In-situ synchrotron x-ray scattering studies of the electrode/electrolyte interface. *PhD thesis*, 2005.

[71] Carl R. Nave. Squid magnetometer. *http://hyperphysics.phy-astr.gsu.edu/hbase/solids/squid.html*, 2011.

[72] R. Moessner and J. T. Chalker. Properties of a classical spin liquid: The heisenberg pyrochlore antiferromagnet. *Phys. Rev. Lett.*, 80(13):2929–2932, Mar 1998.

[73] B. Canals and C. Lacroix. Pyrochlore antiferromagnet: A three-dimensional quantum spin liquid. *Phys. Rev. Lett.*, 80(13):2933–2936, Mar 1998.

[74] S. Di Matteo, G. Jackeli, and N. B. Perkins. Orbital order in vanadium spinels. *Phys. Rev. B*, 72(2):020408, Jul 2005.

[75] T. Suzuki, M. Katsumura, K. Taniguchi, T. Arima, and T. Katsufuji.

Orbital ordering and magnetic field effect in MnV_2O_4. *Phys. Rev. Lett.*, 98(12):127203, Mar 2007.

[76] Vincent Hardy, Yohann Bréard, and Christine Martin. Phase diagram of the spinel oxide MnV_2O_4. *Phys. Rev. B*, 78(2):024406, Jul 2008.

[77] Diamond. Crystal and molecular structure visualization. *http://www.crystalimpact.com/diamond/Default.htm*, Feb 2011.

[78] P. Coppens, L. Leiserowitz, and D. Rabinovich. *Acta Crystallogr, 18:1035.* 1965.

[79] J. H. Chung, J. H. Kim, S. H. Lee, T. J. Sato, T. Suzuki, M. Katsumura, and T. Katsufuji. Magnetic excitations and orbital physics in the ferrimagnetic spinels MnB_2O_4 (B=Mn,V). *Phys. Rev. B*, 77(5):054412, Feb 2008.

[80] Peter. H. Conlon. Manganese vanadate calculations. *Rudolf Peierls Centre for Theoretical Physics, Oxford*, pages 1 – 6, Dec 2009.

[81] M. Rotter. Using mcphase to calculate magnetic phase diagrams of rare earth compounds. *Journal of Magnetism and Magnetic Materials*, 272-276(Supplement 1):481 – 482, 2004. Proceedings of the International Conference on Magnetism (ICM 2003).

[82] M. Rotter, Duc Manh Le, Lucian G. Pascut, Till Hoffmann, M. Doerr, R. Schedler, P. Fabi né Hoffmann,

S. Rotter, and M. Banks. McPhase users manual. *http://www.cpfs.mpg.de/r̃otter/homepage_mcphase/manual/manual.html*, July 2011.

[83] Manh le Duc. MnV_2O_4 mcphase calculations report: Verification using pure spin-wave model. *Helmholtz-Zentrum Berlin fr Materialien und Energie*, August 2010.

[84] M. H. Sage, G. R. Blake, C. Marquina, and T. T. M. Palstra. Competing orbital ordering in RVO_3 compounds: High-resolution x-ray diffraction and thermal expansion. *Phys. Rev. B*, 76(19):195102, Nov 2007.

[85] M. Reehuis, C. Ulrich, P. Pattison, B. Ouladdiaf, M. C. Rheinstädter, M. Ohl, L. P. Regnault, M. Miyasaka, Y. Tokura, and B. Keimer. Neutron diffraction study of YVO_3, $NdVO_3$ and $TbVO_3$. *Phys. Rev. B*, 73(9):094440, Mar 2006.

[86] M. Noguchi, A. Nakazawa, S. Oka, T. Arima, Y. Wakabayashi, H. Nakao, and Y. Murakami. Synchrotron x-ray-diffraction study of orbital ordering in YVO_3. *Phys. Rev. B*, 62(14):R9271–R9274, Oct 2000.

[87] G. R. Blake, T. T. M. Palstra, Y. Ren, A. A. Nugroho, and A. A. Menovsky. Neutron diffraction, x-ray diffraction, and specific heat studies of orbital ordering in YVO_3. *Phys. Rev. B*, 65(17):174112, Apr 2002.

[88] Peter Horsch, Giniyat Khaliullin, and Andrzej M. Oleś. Dimerization versus orbital-moment ordering in a mott insulator YVO_3. *Phys. Rev. Lett.*, 91(25):257203, Dec 2003.

[89] C. Ulrich, G. Khaliullin, J. Sirker, M. Reehuis, M. Ohl, S. Miyasaka, Y. Tokura, and Keimer B. Magnetic neutron scattering study of YVO_3: Evidence for an orbital peierls state. *Phys. Rev. Lett*, 91:257202, 2003.

[90] G. Khaliullin, P. Horsch, and Oleś A.M. Spin order due to orbital fluctuations: Cubic vanadates. *Phys. Rev. Lett.*, 86:3879, 2001.

[91] J. B. Goodenough. Electronic and ionic transport properties and other physical aspects of perovskites. *Reports on Progress in Physics*, 67(11):1915, 2004.

[92] K. I. Kugel and D. I. Khomskii. The Jahn Teller effect and magnetism: transition metal compounds. *Sov. Phys. Usp.*, 25:231, 1982.

[93] Giniyat Khaliullin. Orbital order and fluctuations in mott insulators. *Progress of Theoretical Physics Supplement*, 160:155–202, 2005.

[94] Junjiro Kanamori. Crystal distortion in magnetic compounds. *Journal of Applied Physics*, 31(5):S14 –S23, may 1960.

[95] M Sayer, P Chen, R Fletcher, and A Mansingh. The metal-insulator tran-

sition in lanthanum strontium vanadate. *Journal of Physics C: Solid State Physics*, 8(13):2059, 1975.

[96] T. Shin-ike, T. Sakai, Tetsuo Sakai, G. Adachi, and J. Shiokawa. Spectroscopic studies on the rare-earth vanadites. *Materials Research Bulletin*, 12(7):685 – 688, 1977.

[97] A. V. Mahajan, D. C. Johnston, D. R. Torgeson, and F. Borsa. Magnetic properties of $\mathrm{LaVO_3}$. *Phys. Rev. B*, 46(17):10966–10972, Nov 1992.

[98] Patrick Dougier, Didier Deglane, and Paul Hagenmuller. Evolution of crystallographic, electrical, and magnetic properties of the system $\mathrm{La}_{1-x}\mathrm{Ca}_x\mathrm{VO}_3$. *Journal of Solid State Chemistry*, 19(2):135 – 142, 1976.

[99] G. P. Shveĭkin V. G. Zubkov, G. V. Bazuev. Low-temperature neutron and x-ray diffraction investigations of rare-earth orthovanadites. *Sov. Phys. Solid State*, 18(7):1165, July 1976.

[100] John B. Goodenough. *Magnetism and the Chemical Bond.* R. E. Krieger Pub. Co., 1976.

[101] Y. Ren, T. T. M. Palstra, D. I. Khomskii, E. Pellegrin, Nugroho A. A., A. A. Menovsky, and G. A. Sawatzky. Temperature-induced magnetization reversal in a $\mathrm{YVO_3}$ single crysta. *Nature*, 396:441–444, Dec 1998.

[102] J. P. Hill and D. F. McMorrow. Resonant Exchange Scattering: Polarization

Dependence and Correlation Function. *Acta Crystallographica Section A*, 52(2):236–244, Mar 1996.

[103] J. P. Goff, W. Hayes, S. Hull, M. T. Hutchings, and K. N. Clausen. Defect structure of yttria-stabilized zirconia and its influence on the ionic conductivity at elevated temperatures. *Phys. Rev. B*, 59(22):14202–14219, Jun 1999.

[104] F. Fabrizi, H. C. Walker, L. Paolasini, F. de Bergevin, A. T. Boothroyd, D. Prabhakaran, and D. F. McMorrow. Circularly polarized x rays as a probe of noncollinear magnetic order in multiferroic $TbMnO_3$. *Phys. Rev. Lett.*, 102(23):237205, Jun 2009.

[105] N. Aliouane, K. Schmalzl, D. Senff, A. Maljuk, K. Prokes, M. Braden, and D. N. Argyriou. Magnetic field induced flop of cycloidal spin order in multiferroic $TbMnO_3$: The magnetic structure of the P||a phase. *Phys. Rev. Lett.*, 102:207205, 2009.

[106] N. Aliouane, K. Schmalzl, D. Senff, A. Maljuk, K. Prokes, M. Braden, and D. N. Argyriou. Flop of electric polarization driven by the flop of the Mn spin cycloid in multiferroic $TbMnO_3$. *Phys. Rev. Lett.*, 102(20):207205, May 2009.

[107] E. Arzi. *Introduction to Neutron Powder Diffractometry.* University College Cardiff Press, 1984.

[108] J. Bala and A. M. Oleś. Spin excitations in ferromagnetic manganites with orbital order. *New Journal of Physics*, 6:190, December 2004.

[109] R. Ballou, E. Lelièvre-Berna, and B. Fåk. Spin fluctuations in $(Y_{0.97}Sc_{0.03})Mn_2$: A geometrically frustrated, nearly antiferromagnetic, itinerant electron system. *Phys. Rev. Lett.*, 76(12):2125–2128, Mar 1996.

[110] Martin T. Dove. *Structure and dynamics: An atomic view of materials.* Oxford University Press, Oxford, 2003.

[111] Zhong Fang and Kiyoyuki Terakura. Structural distortion and magnetism in transition metal oxides: crucial roles of orbital degrees of freedom. *Journal of Physics: Condensed Matter*, 14(11):3001, 2002.

[112] T. Fennell, S. T. Bramwell, D. F. McMorrow, and P. Manuel. Pinch points and kasteleyn transitions: How spin ice changes its entropy. *Nature Physics*, 3:566, 2007.

[113] M. J. Harris, S. T. Bramwell, D. F. McMorrow, T. Zeiske, and K. W. Godfrey. Geometrical frustration in the ferromagnetic pyrochlore $Ho_2Ti_2O_7$. *Phys. Rev. Lett.*, 79(13):2554–2557, Sep 1997.

[114] Y. Joly, S. di Matteo, and C. R. Natoli. Ab initio simulations of resonant x-ray scattering on the insulating phase of V_2O_3 compared with recent experiments. *Physical Review B*, 69(22):224401, June 2004.

[115] T. A. Kaplan, K. Dwight, D. Lyons, and N. Menyuk. Classical theory of the ground spin state in spinels. *Journal of Applied Physics*, 32, Dec 1969.

[116] D. I. Khomskii and T. Mizokawa. Orbitally induced peierls state in spinels. *Phys. Rev. Lett.*, 94(15):156402, Apr 2005.

[117] O. J. Lipscombe, G. F. Chen, Chen Fang, T. G. Perring, D. L. Abernathy, A. D. Christianson, Takeshi Egami, Nanlin Wang, Jiangping Hu, and Pengcheng Dai. Spin waves in the (π,0) magnetically ordered iron chalcogenide $Fe_{1.05}Te$. *Phys. Rev. Lett.*, nov 2010.

[118] D. Mannix, D. F. McMorrow, R. A. Ewings, A. T. Boothroyd, D. Prabhakaran, Y. Joly, B. Janousova, C. Mazzoli, L. Paolasini, and S. B. Wilkins. X-ray scattering study of the order parameters in multiferroic $TbMnO_3$. *Phys. Rev. B*, 76(18):184420, Nov 2007.

[119] A. Muñoz, J. A. Alonso, M. T. Casáis, M. J. Martínez-Lope, J. L. Martínez, and M. T. Fernández-Díaz. Crystallographic and magnetic transitions in $cevo_3$: a neutron diffraction study. *Phys. Rev. B*, 68(14):144429, Oct 2003.

[120] A. Muñoz, J. A. Alonso, M. T. Casáis, M. J. Martínez-Lope, J. L. Martínez, and M. T. Fernández-Díaz. Thermal evolution of the crystallographic and magnetic structure in $LuVO_3$: A neutron diffraction study. *Chemistry of Materials*, 16(8):1544–1550, 2004.

[121] B. G. Ueland, J. S. Gardner, A. J. Williams, M. L. Dahlberg, J. G. Kim, Y. Qiu, J. R. D. Copley, P. Schiffer, and R. J. Cava. Coexisting magnetic order and cooperative paramagnetism in the stuffed pyrochlore $Tb_{2+x}Ti_{2-2x}Nb_xO_7$. *Physical Review B*, 81(6):117, 2010.

[122] A. S. Wills. Validation of magnetic structures. *Zeitschrift fr Kristallographie Supplements*, 26:53–58, 2007.

[123] Guangyong Xu, J. F. Di Tusa, T. Ito, K. Oka, H. Takagi, C. Broholm, and G. Aeppli. Y_2BaNiO_5: A nearly ideal realization of the $S = 1$ Heisenberg chain with antiferromagnetic interactions. *Phys. Rev. B*, 54(10):R6827–R6830, Sep 1996.